Evaluating Emissions of Nitrogen Oxides in Megacities

William Stephen Drysdale

PhD

University of York
Chemistry
September 2020

Abstract

It is estimated that 7 million deaths globally are due to poor air quality. Understanding the sources, transport, transformation and eventual fate of pollutants in the atmosphere is important in informing interventions to reduce this number. This thesis focuses on measuring emissions of Nitrogen Oxides in two megacities - London, UK (spring 2017) and Delhi, India (pre- and post-monsoon 2018) - and using them to evaluate emissions inventories. A good understanding of urban emissions is important, as the proportion of the global population living in them is ever increasing and with it total exposure to poor air quality. Nitrogen oxides are of interest due to their role in tropospheric ozone formation and the detrimental health effects of nitrogen dioxide.

Here, eddy covariance has been used to measure NO_x emission in both cities, and developments have been made in mass balance methods towards an alternative measurement of NO_x emission in London.

The measurements made in London, in agreement with previous measurements, found that there is an underestimation of NO_x emission by the UK's National Atmospheric Emissions Inventory by an average of 1.4 × and that this became more pronounced at the weekends due to differences between diurnal traffic flow and the diurnal profile used to scale road traffic emissions.

In Delhi, NO_x emissions were measured at two sites, and a local inventory was shown to overestimate the emissions significantly, however, the spatial variation in emissions was well captured.

Finally, work on the mass balance method highlighted key areas for continued development for the method to be applicable for reactive gases and large targets such as London. These include improving the treatment of chemical transformation between emission and measurement, and more robust treatment of the air mass being sampled to connect it with emissions inventories.

Contents

List of Tables

List of Figures

Acknowledgements

I would first like to acknowledge and thank my supervisors James Lee and Ruth Purvis for the opportunity to undertake this PhD, along with their help and guidance throughout the process. Many thanks also are warranted to a myriad of colleagues at the Wolfson Atmospheric Chemistry Laboratories, those involved in the Air Pollution and Human Health campaigns and those at the National Ecology Observatory Network, who answered many, many questions and allowed me to learn from them numerous skills required to complete this work.

Those who completed their own PhDs concurrently at WACL; Freya, Pete, and Stefan, deserve special thanks. Without them the experience would not have been what it was. In addition to their support throughout, providing many lively discussions (including unique perspectives on the scale of the atmosphere), impromptu doughnut supply and being excellent friends and housemates are but a few of their qualities.

Finally, thanks to my mum, dad, and brother, who were a source of resolute optimism and encouragement, in the absence of which I would not have been able to achieve this.

Declaration

I declare that this thesis is a presentation of original work and I am the sole author. This work has not previously been presented for an award at this, or any other, University. All sources are acknowledged as references.

Section 1.5.1 is based upon my contribution to published work, the details of which are:

J. D. Lee, W. S. Drysdale, D. P. Finch, S. E. Wilde and P. I. Palmer. ”UK surface NO_2 levels dropped by 42 % during the COVID-19 lockdown: impact of surface O_3 ”. *Atmospheric Chemistry and Physics* (2020), 15743–15759

Chapter 1

Introduction

Poor air quality is driven by combination of pollutant emission, chemistry and meteorology. The primary introduction of pollutants to the atmosphere come from a combination of anthropogenic and biogenic sources, followed in some cases by chemical production of secondary pollutants. Meteorology affects the transport of the pollution through the atmosphere and the magnitude of concentrations that result from emission. The anthropogenic emission of pollutants has increased globally due to population growth and economic development driving demand for polluting technologies.

Air pollution is not a recent issue, but the pollutants of importance have changed with both changing technology and implementation of abatement strategies. For example the introduction of the Clean Air Act in the UK started the move towards smokeless fuels reducing the concentrations of sulphur dioxide (SO_2) and large particulates which, when combined with adverse meteorological conditions, caused air pollution events like the Great Smog of London of 1952 [1].

More recently the increased emissions of hydrocarbons from road transport vehicles required the installation of catalytic converters, of which newer three-way versions also somewhat addressed nitrogen oxide (NO_x= NO + NO_2) emissions. However, whilst petrol cars could reach emissions standards using this technology, diesel vehicles could not, due to operating with a more O_2 rich exhaust. Exhaust gas re-circulation (EGR) can be used to reduce some of these emissions, by re-circulating some of the exhaust air back through the engine, lowering both the temperature and amount of O_2, reducing NO_x emission at the expense of fuel efficiency. Across Europe there has been much larger uptake of diesel vehicles than in other regions of the world, with 50 % of new cars in 2011 in the UK being diesels. This growth was due to incentives instated by the European Union as a part of policy focusing on reduction of greenhouse gas emissions encouraging the use of more fuel efficient diesels over petrol cars to help achieve this [2]. This led to much of the fleet breaching NO_x emissions standards. Euro VI emissions standards have focused on reducing these NO_x emissions further still and at first this lead to attempts from some manufacturers to circumvent emissions testing [3–5]. These manufacturers opted to install "defeat devices" in the vehicle software to fool the emissions certification tests [6]. As the emissions testing procedure involved a regimented driving cycle under controlled conditions, the on-board computer was able to detect the test being performed and enabling emission controls during the test, but under real driving conditions, EGR was disabled. These unexpectedly high emissions were discovered through independent monitoring by the International Council on Clean Transportation measuring emissions on the road, and ultimately has lead to changes in emissions testing to prevent defeat devices from being useful [7]. Despite this, vehicles have begun to adopt new emission reductions technology. and Euro VI compliant vehicles have begun to enter the fleet (figure 1.1).

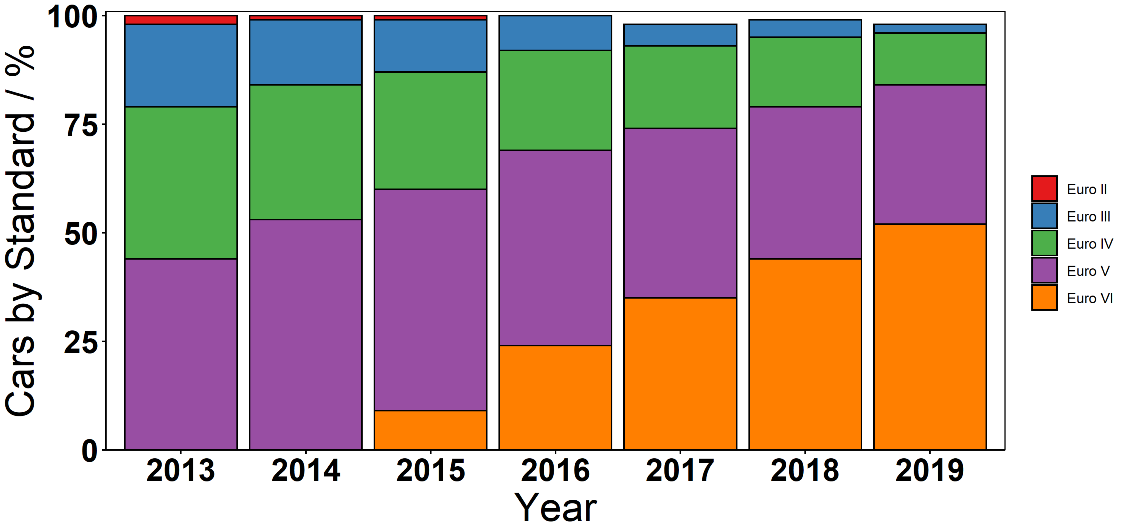

Figure 1.1: Change in non-hybrid cars outside of London in the UK by euro standard 2013 - 2019

Lean NO_x traps (LNT) and selective catalytic reduction (SCR) are two of the main technologies being employed to curb NO_x emission. LNTs are an augmented three-way catalytic converter that is capable of adsorbing NO_x during O_2 rich operation, common in diesel vehicles - during which a traditional catalytic converter would be unable to reduce NO_x to N_2 - and later releasing and regenerating the surface when NO_x reduction to N_2 can be performed. SCR uses ammonia to perform this reduction, requiring a regent such as urea to be added to the vehicle. Both methods reduce the overall NO_x emission from the vehicle, with SCR being particularly effective [8]. The ultra-low emissions zone, implemented in London in 2019, specifies Euro VI as the minimum acceptable emission standard for diesel cars to increase usage of these new technologies and further encourage reductions in NO_x emission.

Over the course of the last 30 years, the average concentrations of NO_x in the UK have decreased, due to these emissions controls (figure 1.2). This trend is more prevalent in urban areas, where traffic sources are more dominant, however the rate of reduction has been slower since ~2005. This has also had the effect of increasing urban O_3 levels closer to those seen at rural sites, due to the reduced competition of NO_x with available oxidants (see section 1.3). Whilst there is ongoing work to limit air pollution, the World Health Organisation estimated that in 2016 7 million deaths were due to poor air quality (both ambient and indoor), demonstrating that air pollution very much an ongoing problem [9]. Projections of future air quality suggest that the combination of O_3 and $PM_{2.5}$ (particles with diameter less than 2.5 μm) could be responsible for twice their current global mortality by 2050 assuming continued levels of pollution [10]. However, those from $PM_{2.5}$ may reduced by a factor 1.1 - 1.7 by the end of the century if emissions reductions based upon the representative concentration pathways adopted by the Intergovernmental Panel on Climate Change are implemented successfully[11, 12].

To further mitigate and avoid future problems caused by poor air quality it is important that the sources, processes, and ultimate fate of pollutants released into the atmosphere are well understood. This thesis focuses on the measurement of NO_x emission in two megacites - Greater London, UK and Delhi, India - and the application of these measurements to emissions inventory evaluation. In this chapter the meteorology important to air pollution and the role NO_x in the lower atmosphere are introduced, along with the direct and in-direct effects of key air pollutants on human health.

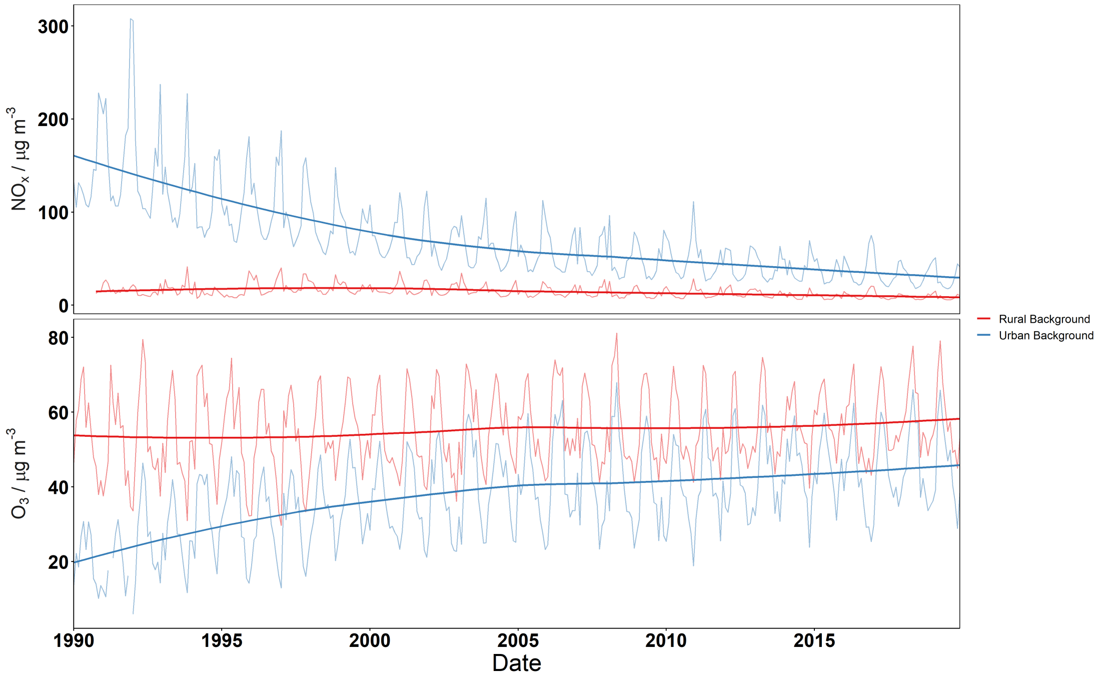

Figure 1.2: NO_x (top) and O_3 (bottom) monthly mean concentrations from measurements made at urban (blue) and rural (red) background sites on the Automatic Urban and Rural Network in the UK from 1990 to 2019. Loess smoothing is overlaid to show overall trend.

1.1 Meteorology

Meteorology governs the structure and motion of the atmosphere into which pollutants are emitted, subsequently affecting their concentrations and any transportation from their source. When focusing on the impact of air pollutants on human health, the primary areas of concern are where the most exposure occurs; in the context of the atmosphere, this is the lowest layer, the troposphere, as this borders the earths surface. The troposphere spans from the surface to ~10 - 15 km high. This layer is separated from the stratosphere (ranging from ~10 - 50 km) by a temperature inversion due to heating from absorbance of solar radiation < 290 nm by O_3. This minimises mixing between the layers, trapping most surface emissions in the troposphere. The troposphere can be further subdivided into the boundary layer and free troposphere. The boundary layer comprises the lower layer of the troposphere and is discussed in detail in section 1.1.1. The dynamics of the boundary layer influence a pollutant's behaviour shorty after emission, and underpin the eddy covariance (EC) methods employed in chapters 3 and 4. The method is discussed in detail in 2. While primarily affected by the micrometeorological processes governing the boundary layer, a pollutants concentration and fate are also governed by larger scale processes and are discussed further in section 1.1.2. In addition to the references within, a detailed overview of the boundary layer can be found in Stull 1988, which much of the following sections are based upon [13].

1.1.1 Twenty Thousand Metres Under the Stratosphere

The boundary layer comprises the lowest layer of the troposphere and is characterised broadly as the portion of the atmosphere who's behaviour is driven by its interaction with the Earth's surface. It responds to forcing from the surface on timescales of the order of about an hour or less and can extend over heights of tens to low thousands of meters depending on time of day, surface and latitude. These interactions with the surface can include a variety of factors (such as the the aforementioned emission of pollutants) but the presence of turbulence is an important resultant property of several of them, namely buoyancy and wind shear.

Generally, turbulent flow is the property of a fluid (which in this case is air) within which the particles flow chaotically, resulting in minimal predictability and high sensitivity to initial conditions. This is opposed to laminar flow, where the fluid moves in layers where properties such as velocity remain mostly constant spatially and when they do change, transition smoothly between states.

Turbulent motion in the boundary layer is mainly driven by convection. Air parcels close to the surface are heated and therefore become more buoyant, these then rise through the boundary layer, cooling radiatively and descending again. This promotes mixing throughout the boundary layer and creates turbulent motion as many air parcels of varying size are rising and descending simultaneously. Additionally, wind shear (rapid changes in wind speed or direction over a short distance) can generate turbulence. Turbulence drives vertical transport within the boundary layer, but as the average vertical wind over sufficient time scale is considered to be 0.00 m s^{-1} (as air is not being lost from the atmosphere), the boundary layer becomes vertically well mixed.

The remainder of the troposphere above the boundary layer is referred to as the free troposphere, which, by definition, lacks this much of this surface induced turbulence (though can still experience shear induced turbulence) and instead motion of air here is driven by advection - transport with the mean wind direction. During the day, as surface heating increases, the boundary layer grows entraining air from the free troposphere to do so, and as the surface cools the boundary layer decays. This can introduce transported pollutants into the boundary layer or release them into the free troposphere to be transported further away. Indeed, horizontal advection is also present in the boundary layer, transporting pollutants locally and allowing the application of Taylor's frozen turbulence hypothesis [14] which is important to EC measurements.

Boundary layer growth is driven by surface heating, so greater heights and diurnal variability are seen over the land, where the surface has a lower heat capacity, heating more rapidly and to greater temperatures than over the ocean. As sea surface temperatures are less variant, boundary layers over the ocean vary comparatively little between day and night, and remain more stable due to a shallower vertical temperature gradient. Over land a stable layer usually forms within the lower portion of the boundary layer overnight when turbulence has decreased, and can further limit vertical mixing of pollutants until turbulence resumes, creating a residual layer between the free troposphere and this nocturnal boundary layer. Figure 1.3 shows schematic boundary layer development over a day. Boundary layer stability refers to whether conditions are causing turbulence to increase, be maintained, or decrease. One measure of this is the stability parameter from Monin-Obukhov similarity theory; z/L, where z is the measurement height and L is the Obukhov length. L is proportional to the displacement above the surface where buoyancy has a greater contribution to turbulence than wind shear, and as such the sign of z/L indicates stability, negative is unstable - turbulence is increasing - and positive is stable - turbulence is decreasing [15].

Urban areas can experience higher nighttime boundary layers than rural areas as the surface retains its heat for longer. This is known as an urban heat island and can result in convection driving turbulence overnight, such that a stable layer never forms. These persistent mixed layers can then be driven up if they are advected out of the city, pushed above cooler stable layers that have formed in surrounding rural areas, transporting pollution in the cities plume further than if the air mass had remained lower [16].

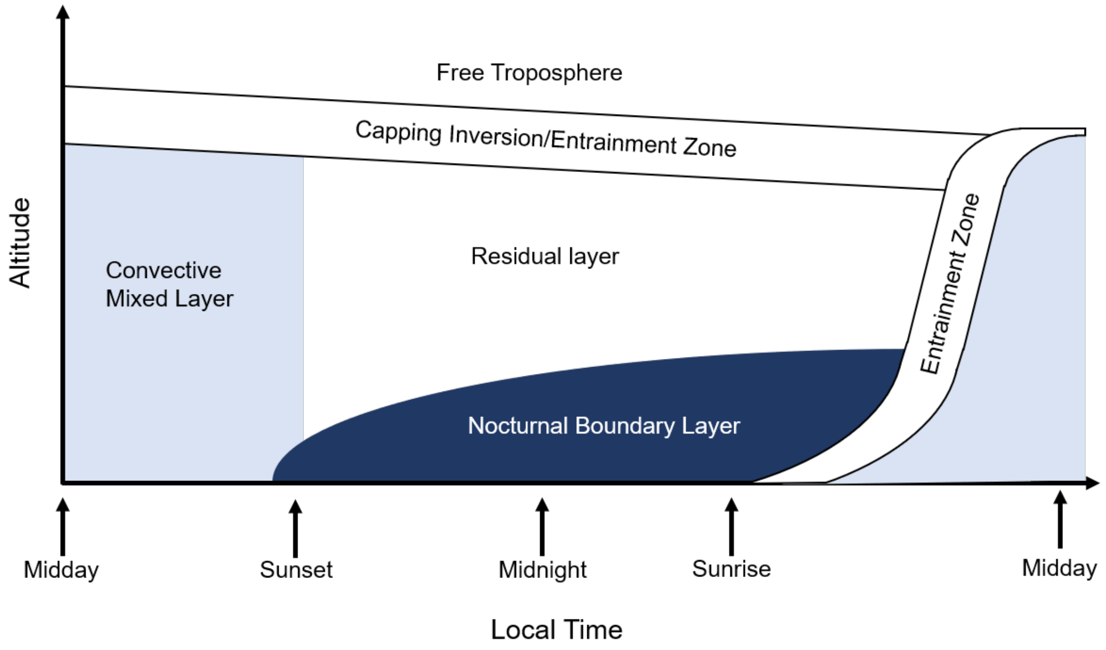

Figure 1.3: Schematic of boundary layer development over 24 hours. Based upon a similar diagram from Stull 1988 [13].

1.1.2 Effects of the Boundary Layer and wider Meteorology on Pollutant Concentrations

The development of the boundary layer throughout the day can have diluting effects on the concentration of pollutants. Ignoring emission or production of a pollutant, the growing boundary layer mixes cleaner air in from the free troposphere, lowering concentrations through the day. This is observed as a sinusoidal pattern in some diurnal profiles, including those measured in this thesis (see NO_2 in figure 3.8 and several pollutants in figure 4.4). In these examples the decrease is strongly anti correlated with boundary layer height. Of course, this is not observed for all pollutants, O_3 in figure 3.8 does not show this pattern, as its production overcomes this dilution effect. Lower boundary layers can drive higher concentrations, especially stable layers with little turbulent mixing, as are often observed overnight [17].

Wind speeds also impact ambient concentrations. As mentioned previously they can increase turbulence, but also drive advection. Higher wind speeds therefore lead to lower concentrations, but increased transport of emissions, which can move the problem of pollution downwind. Large scale movement of air masses is also important, as these influence the background concentrations into which local pollution is emitted. Lamb Weather Types have been used to classify synoptic scale weather patterns over the United Kingdom - generally grouped by wind conditions, e.g. cyclonic (counter-clockwise curl of the wind direction), anticyclonic (clockwise curl of the wind direction) and cardinal wind directions [18, 19]. Several studies have observed that anticyclonic, easterly and south-eastern conditions lead to enhancements in NO_2 , O_3 and $PM_{2.5}$ [20]. This is due to reduced air mass mobility in anticyclonic conditions, which in turn reduces the transport of pollutants away from their source, and due to transport from mainland Europe in the case of easterly flows, whereas westerly flows bring cleaner air from the Atlantic [21, 22].

1.2 Sources of NO_x

Global emissions of NO_x were estimated to be ~38 TgN yr^{-1} in 1996 [23]. The Emission Database for Global Atmospheric Research (EDGAR) estimates that global surface NO_x emissions in 2012 were ~121.8 Tg yr^{-1}, which assuming 100 % of the emission is as NO, is roughly 56.9 TgN yr^{-1} (note that under this assumption, the EDGAR inventory estimates ~45.0 TgN yr^{-1} in 1996) [24]. Tropospheric NO_x is primarily emitted as NO as a by product of high temperature combustion and as such anthropogenic sources dominate, especially road transport. Exceptions to this include natural emissions from lighting and soil (~5.8 and ~5.6 TgN yr^{-1}) and lower temperature biomass burning (~5.9 TgN yr^{-1}) [25, 26].

The dominance of anthropogenic emissions leads to higher levels of NO_x generally being found in areas of higher population. The world average population passed 50 % living in urban areas in 2007, and in 2018 between 42.5 % (in Africa) and 82.2 % (in Northern America) live in urban areas. By 2050 this is projected to narrow to between 58.9 - 89.0 %, with a global average of 68.4 % (figure 1.4) [27, 28]. With the proportion of the world's population living in urban areas increasing, both emission of and human exposure to air pollution in these regions will increase.

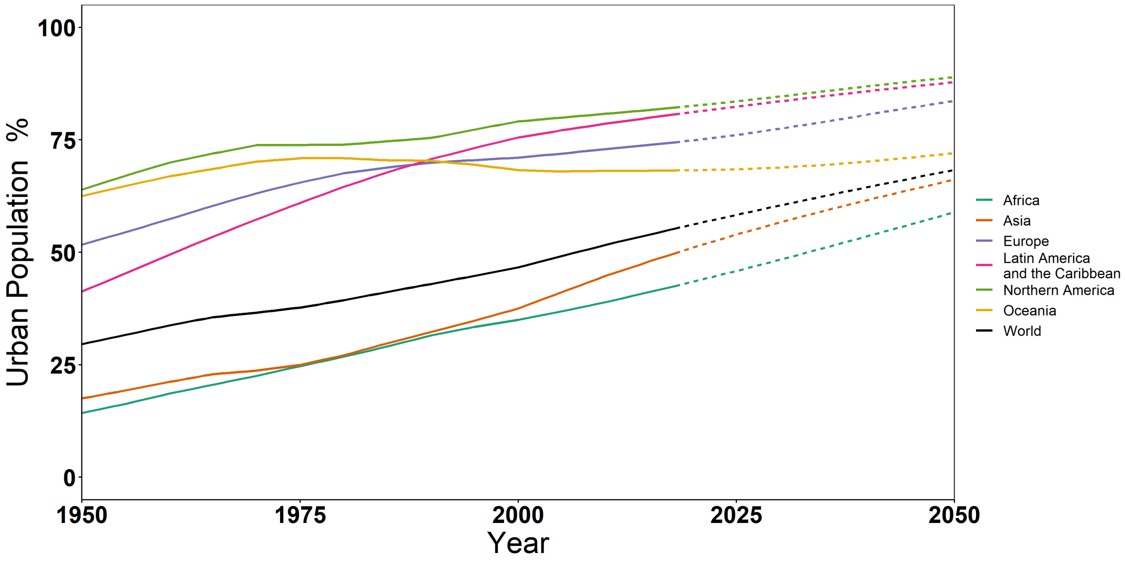

Figure 1.4: Proportion of world population living in urban areas, from 1950 - 2018 (solid). Projection of population in urban areas 2018 - 2050 (dashed) [27].

For example, the National Atmospheric Emissions Inventory (NAEI), a top-down atmospheric emissions inventory for the United Kingdom (see section 3.3.1 for more details), breaks emissions down into several sectors [29]. For NO_x , road transport dominates making up 39 % of onshore emissions, followed by other transport and energy production sectors (figure 1.5). Urban centres contribute disproportionately to these emissions per unit area, with Greater London contributing 5.3 % of the UK's total NO_x emissions whilst being focused in < 0.7 % of the area. The combination of Greater London, Greater Manchester and

Birmingham make up 8.8 % of total emissions in 1.3 % of the area, but do however include roughly 20 % of the UK's population. Focusing on these urban centres also increases the contribution to emissions from road transport and domestic combustion, seen in figure 1.5 when the UK is compared to Greater London.

It should also be noted that other important pollutants that degrade air quality share emissions sources with NO_x. Figure 1.6 shows $PM_{2.5}$ has large contributions from road transport, other transport and domestic combustion sectors both at the country and city scale. Conversely, non-methane volatile organic compounds (NMVOCs) have their major contributions from other sources, namely solvent use and production, agricultural and natural sources which combined contribute 57.3 % at the UK level and 66.2 % in Greater London. Section 1.3 described the importance of both NO_x and NMVOCs being present for in-situ O_3 production, and their emissions should be reduced inline with one another to avoid inadvertently moving into higher O_3 production regimes. Implementing policy to this effect is made harder due to this lack of overlap between emissions sources.

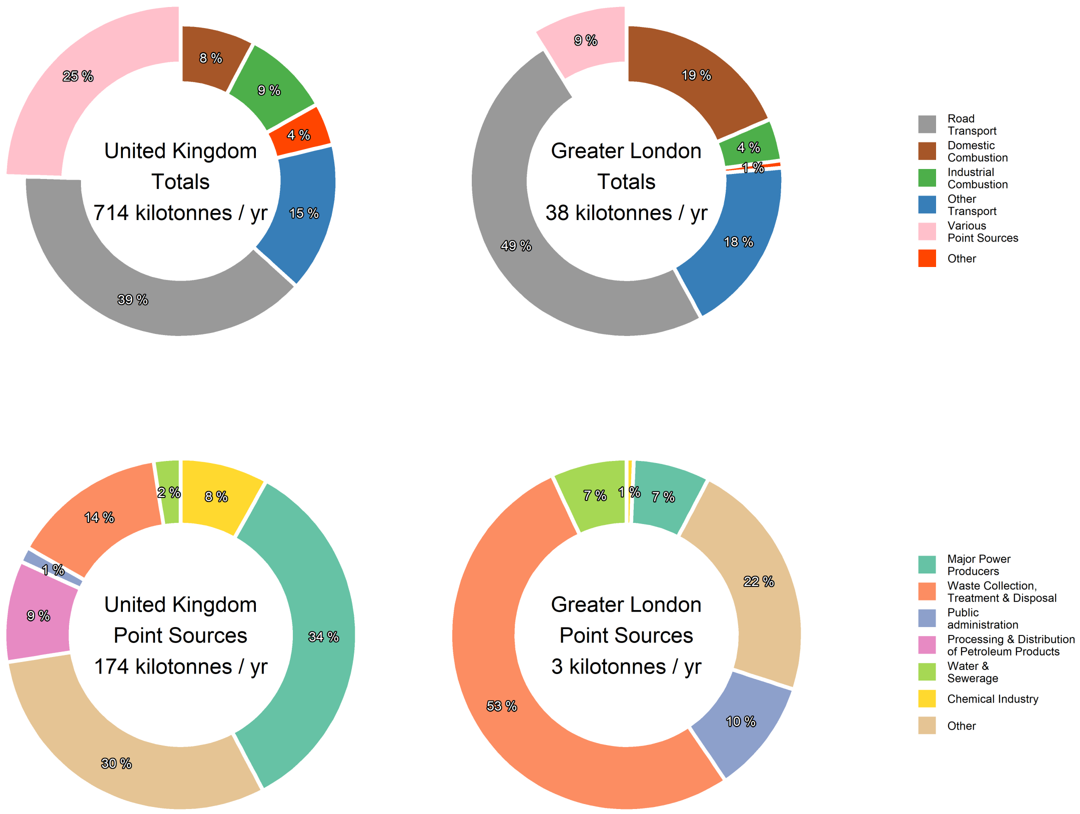

Figure 1.5: Top - Total onshore NO_x emission by sector for the UK (left) and Greater London (right) from the 2017 National Atmospheric Emissions Inventory [29]. Data outside of UK borders were excluded from the totals, to be more representative to the Greater London emissions, which naturally exclude these. Sectors that contribute to "Other" (values from UK totals): agriculture 3.7 %, energy production 0.4 %, natural 0.2 %, waste 0.1 %, solvents < 0.1 %, and industrial processes < 0.1 %. Some of these will also be represented by point sources instead, included in the offset wedge. Bottom - The 'Various Point Sources' sector subdivided into more groups. Kilotonne values do not exactly match percentages above due to the point source spatial layer used as the data source for the top row and a separate point source list used for the bottom.

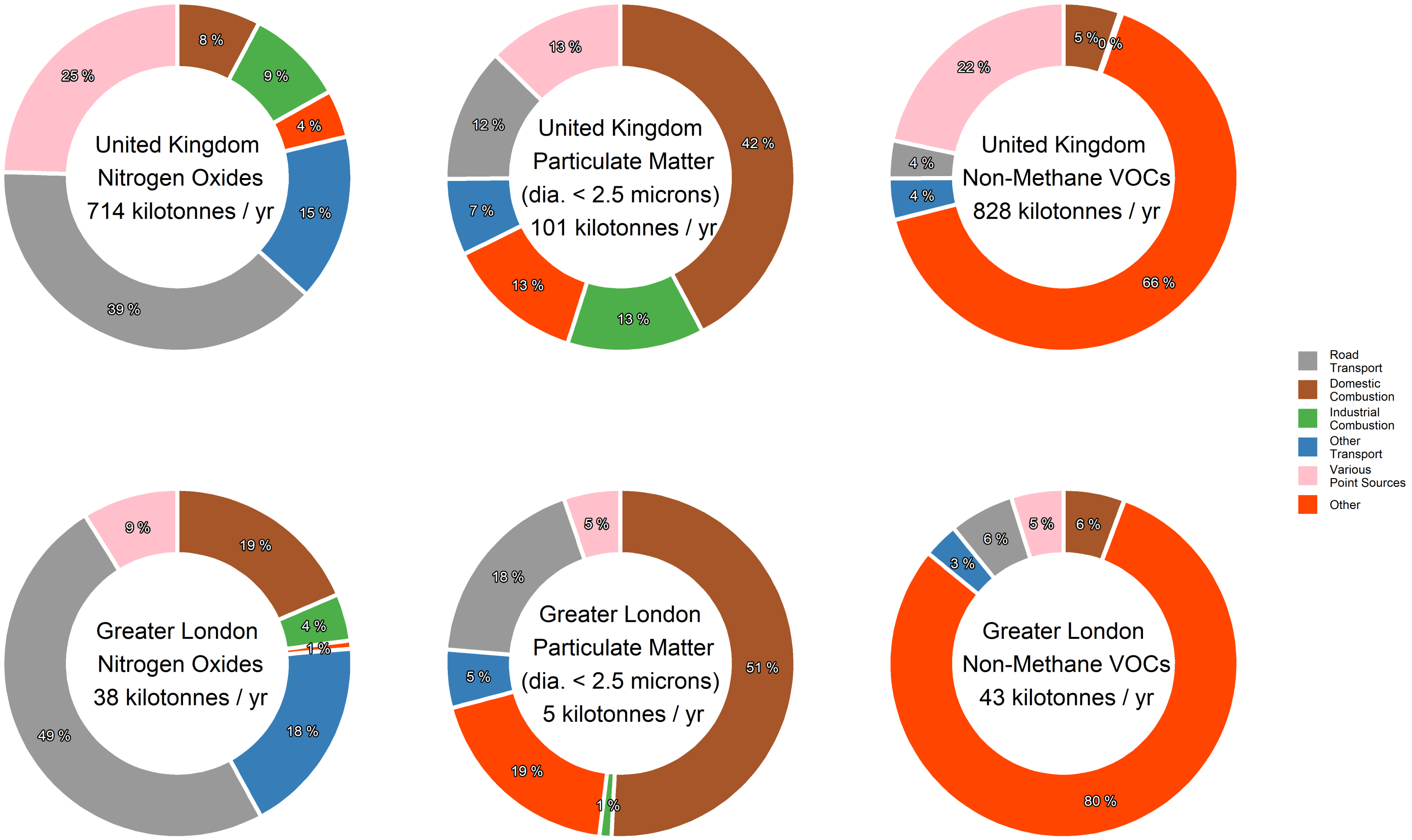

Figure 1.6: Total onshore pollutant emission from the NAEI (left to right: NO$_x$, PM$_{2.5}$ and NMVOC) by sector for the UK (top) and Greater London (bottom) [29]

1.3 The Chemistry of NO_x in the Troposphere

NO_x is an important pollutant in the troposphere for for two reasons; it provides routes for the formation of O_3, which is damaging to human health as is NO_2 in its own right. Figure 1.7 presents a simple overview of the chemical processes found in the troposphere. As mentioned previously, the stratosphere absorbs much of the high frequency radiation reaching the lower layers of the atmosphere and limits the photochemistry to reactions involving radiation at wavelengths greater than 290 nm (actinic radiation).

The right hand side of figure 1.7 represents a clean atmosphere i.e. no significant NO_x concentrations. Here the hydroxyl radical (OH) is formed during the day from the reaction of water with atomic oxygen (O^1D), this triggers oxidation of organic molecules and the formation of hydroperoxy and alkylperoxy radicals (HO_2 and RO_2 - herein grouped as *peroxy radicals*, formed via R 1.1 - R 1.6). These eventually undergo radical chain termination as hydroperoxides (ROOH or H_2O_2) and ultimately removed from the atmosphere through dry and wet deposition [30]. Figure 1.7 shows the route by which general organic species (RH, where the R group represents the characteristic functional group of a specific volatile organic compound) undergoes this oxidation (R 1.1 and R 1.2) . This section of the cycle can also result in the net destruction of O_3 when a similar process resulting in the formation of HO_2 is followed (R 1.3 - R 1.7).

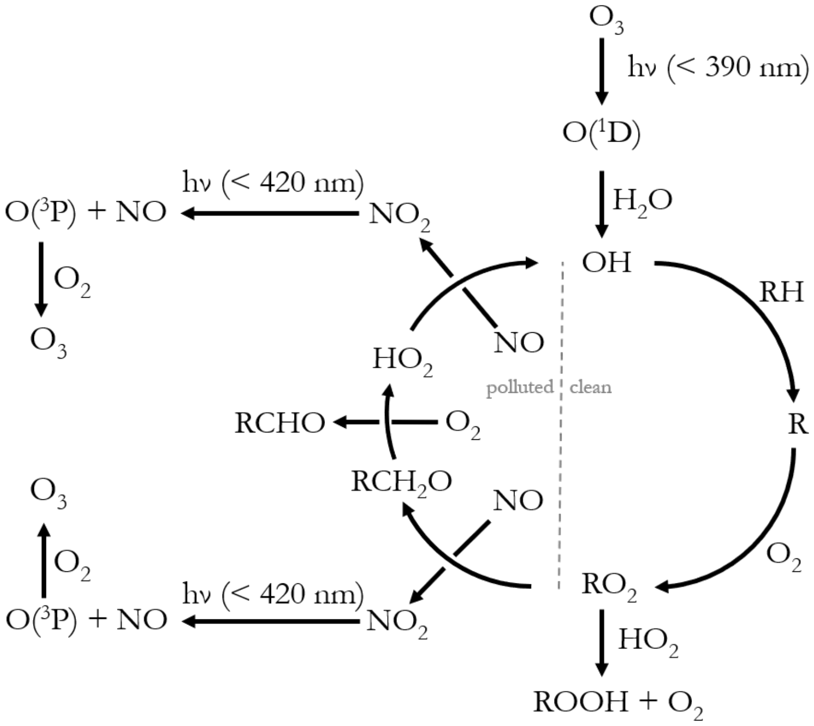

Figure 1.7: Simple overview of atmospheric chemistry in the troposphere. The R group represents the characteristic functional group of a specific volatile organic compound. NO to NO_2 conversion is described in equations R 1.8 and R 1.9

$$\mathrm{OH + RH \longrightarrow R + H_2O} \tag{R 1.1}$$

$$\mathrm{R + O_3 \xrightarrow{M} RO_2} \tag{R 1.2}$$

$$\mathrm{HCHO \xrightarrow{h\nu\, <\, 334\, nm} HCO + H} \tag{R 1.3}$$

$$\mathrm{H + O_2 \xrightarrow{M} HO_2} \tag{R 1.4}$$

$$\mathrm{HCO + O_2 - HO_2 + CO} \tag{R 1.5}$$

$$\mathrm{OH + CO \longrightarrow CO_2 + H} \tag{R 1.6}$$

$$\mathrm{O_3 + HO_2 \longrightarrow 2\,O_2 + OH} \tag{R 1.7}$$

However, the remainder of the cycle in figure 1.7 provides an alternative pathway for the peroxy radicals, via the oxidation of NO to NO_2. The cycling of NO and NO_2 and subsequent O_3 production is summarised in equations R 1.8 - R 1.10.

$$\mathrm{NO + X \longrightarrow NO_2} \tag{R 1.8}$$

$$\mathrm{NO_2 \xrightarrow{h\nu\, <\, 420\, nm} NO + O(^3P)} \tag{R 1.9}$$

$$\mathrm{O(^3P) + O_2 \xrightarrow{M} O_3} \tag{R 1.10}$$

In R 1.8 X is any of O_3, RO_2 or HO_2, all of which can oxidise NO to NO_2. When X is O_3, these reactions form an cycle with no net production or loss of O_3, but when peroxy radicals are available in the place of X, this null cycle is perturbed leading to net production of O_3. Furthermore, HO_2 can be regenerated from the products of R 1.8 when X is RO_2 upon abstraction of H from RCH_2O (alkoxy radical, expanded from RO) by O_2, which can again go onto oxidise NO and subsequently create more O_3 (R 1.11).

$$\mathrm{RCH_2O + O_2 \longrightarrow HO_2 + RCHO} \tag{R 1.11}$$

Clearly, O_3 formation requires NO_x but the peroxy radicals are needed for net production which in turn require the presence of non-methane volatile organic compounds (NMVOCs). The O_3 production potential for varying concentrations of NMVOCs and NO_x can be represented on an O_3 production isopleth, an example of which is shown in figure 1.8. These isopleths are formed by modelling the O_3 produced (shown on the z axis) by different combinations of NO_x /VOC starting concentrations (given on the y and x axis). Polluted urban areas, such as central London, are often categorised as being under VOC limited regimes [31], due to the relative abundance of NO_x in these areas. Under some VOC limited conditions, reduction in NO_x can actually drive an increase in O_3 production as formation of HNO_3 from NO_2 competes for the availability of OH and removes both from the system in a radical termination step (R 1.12). Alternatively, an overabundance of NO_x can suppress the O_3 production potential owing to R 1.12 competing for OH [32]. The decrease in OH limits the available peroxy radicals, in turn limiting oxidants alternative to O_3 in R 1.8. There are then less cycles of NO oxidation that result in net O_3 formation. This formation of HNO_3 also constitutes the primary loss route for NO_2 , which leads to a lifetime on the order of hours [33].

$$NO_2 + OH \xrightarrow{M} HNO_3 \tag{R 1.12}$$

The rapid interconversion between NO and NO_2 via O_3 results in an equilibrium between the three species (photostationary state) and, in the absence of peroxy radicals, the combination of R 1.8 - R 1.10 results in a null cycle (as in R 1.8, when X is O_3 and O_2 is an additional product). The O_3 concentration can then be written as equation 1.1, where $j_{R\,1.9}$ is photolysis rate for the dissociation of NO_2 and $k_{R\,1.8}$ is the rate of reaction of NO with O_3 to form NO_2 [32].

$$[O3] = \frac{j_{R1.9}[NO_2]}{k_{R1.8}[NO]} \tag{1.1}$$

As this model of the system does not contain the perturbations due to the presence of peroxy radicals discussed previously, the equation can be rewritten as equation 1.2 [34]. Here ϕ is the Leighton ratio, and is unity when there are no other oxidants than O_3 available and greater than unity when there are [35].A negative value suggests that the photo stationary state has not yet been reached, such as near a NO emission source.

$$\phi = \frac{j_{R1.9}[NO_2]}{k_{R1.8}[NO][O_3]} \tag{1.2}$$

ϕ is often close to unity in high NO_x environments, due to NO_2 limiting the availability of peroxy radicals [36]. In lower NO_x environments (or as the relative NO_2 concentration is depleted in an air mass), ϕ will increase and thus O_3 production. This will continue until a point of maximum O_3 production can be reached and it enters into a NO_x limited regime, with R 1.9 becoming the rate limiting step. These parameters for O_3 production have consequences when emissions controls are to be considered. Reduction of NO_x emissions without the reduction of NMVOC emissions may result in a NO_x limited regime being reached sooner, likely increasing O_3 production nearer the original emissions sources. In the converse case, reductions in NMVOC emissions without the reduction of NO_x emissions may drive O_3 production to peak further from the emissions sources, causing O_3 problems further afield [37].

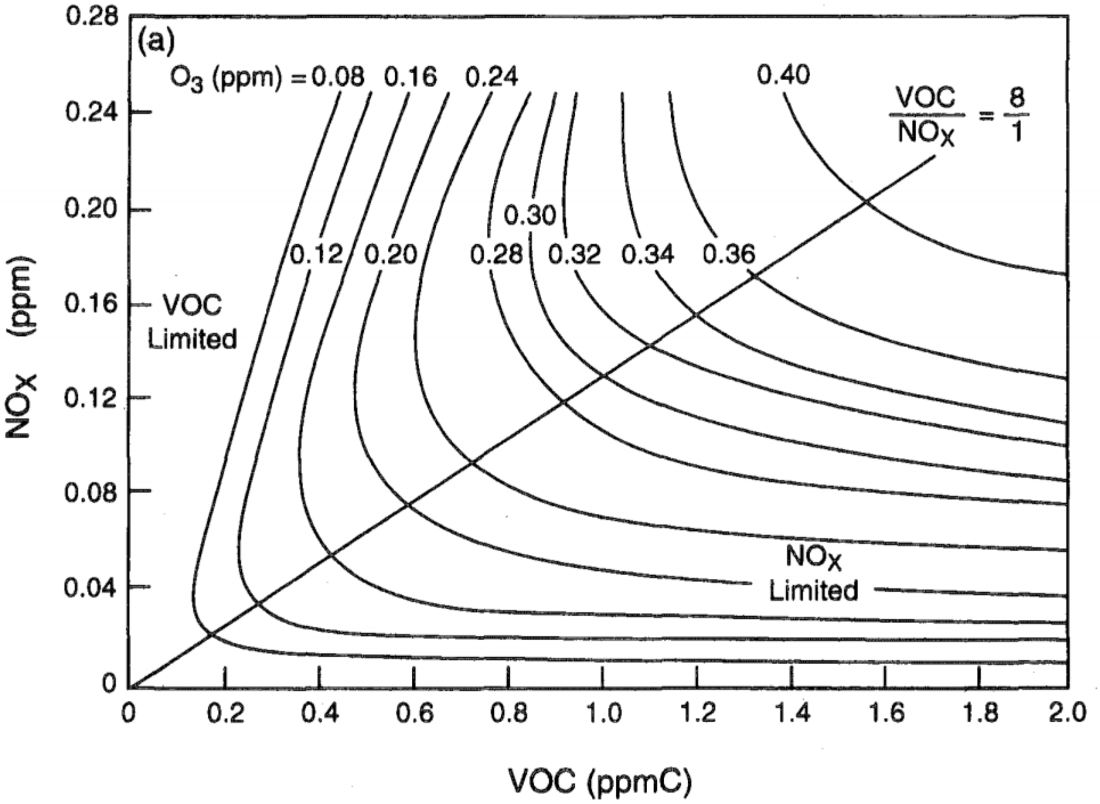

Figure 1.8: Example O_3 production isopleth, based upon their initial concentrations in an air mixture and generated via a combination of modelling and atmospheric chamber data. Reproduced from Finlayson-Pitts and Pitts 1993 [38]

Equation R 1.12 has already shown the primary loss route for NO_2 to HNO_3. HNO_3 is removed from the atmosphere via wet deposition or though neutralisation on reaction with ammonia, potentially leading to aerosol formation. As this loss mechanism for NO_2 is facilitated by OH, it mainly occurs during the daytime. NO_2 can react with RO_2 to form peroxyacyl nitrate (PAN) species (R 1.13). PAN acts as a reservoir for NO_x and can increase the range it can be transported, as it evades loss to HNO_3. PAN reverts to RO_2 and NO_2 via thermal decomposition, so can be a particularly large reservoir when transported to or formed in cooler regions [39]. Depending on temperature and pressure the lifetime of PAN can range from minutes to days, which can aid transportation, with increased lifetime at the lower pressures and temperatures when lofted into the free troposphere.

$$RO_2 + NO_2 \underset{\Delta}{\rightleftharpoons} PAN \tag{R 1.13}$$

During the night, NO_2 can form the nitrate radical (NO_3) on reaction with O_3 (R 1.14). The nitrate radical is rapidly photolysed in the day (lifetime < 5 s [32]), limiting its formation to the nighttime. It can act in place of the OH radical similarly to the initiation of the cycle presented in figure 1.7, forming alkyl radicals and nitric acid (R 1.15), again ultimately forming a loss route for NO_2. Additionally, NO_3 can react with NO_2 to form N_2O_5 reversibly, which can act as a reservoir for NO_2 overnight, and a morning source (R 1.16). The N_2O_5 reservoir in the presence of Cl, can be extended to include $ClNO_2$ (R 1.17).

$$NO_2 + O_3 \longrightarrow NO_3 + NO_2 \tag{R 1.14}$$

$$NO_3 + RH \longrightarrow R + HNO_3 \tag{R 1.15}$$

$$NO_3 + NO_2 \xrightleftharpoons{M} N_2O_5 \tag{R 1.16}$$

$$N_2O_5 + Cl \longrightarrow ClNO_2 + NO_3 \tag{R 1.17}$$

A final important transformation NO_x can undergo in the atmosphere is NO's interaction with OH to form HONO (R 1.18). As HONO is rapidly photolysed by UV light (R 1.19), build up usually occurs at night, and its decay can be an early morning source of OH. It can also be a source of NO_2 via oxidation by OH (R 1.20) [40].

$$NO + OH \xrightarrow{M} HONO \tag{R 1.18}$$

$$HONO \xrightarrow{h\nu} OH + NO \tag{R 1.19}$$

$$HONO + OH \longrightarrow H_2O + NO_2 \tag{R 1.20}$$

The reactions described in this section are summarised in figure 1.9.

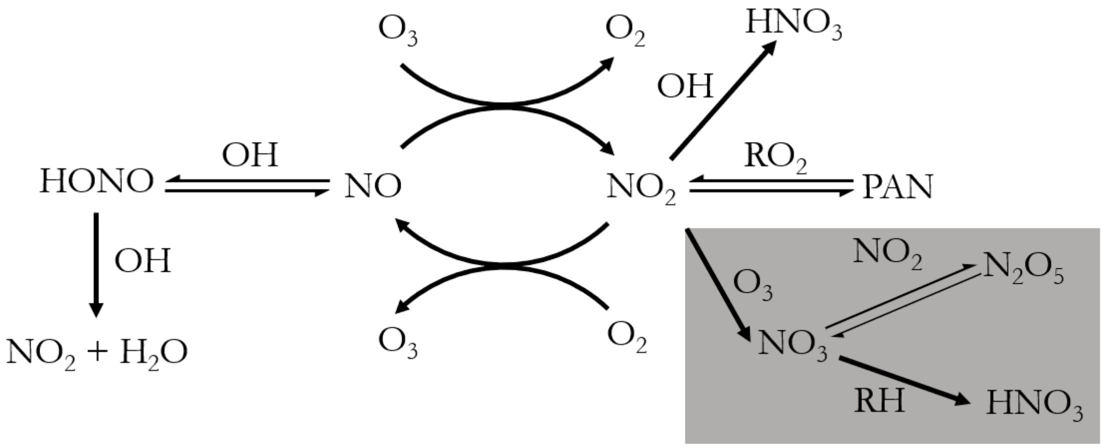

Figure 1.9: Overview of NO_2 related chemistry in the troposphere. Shaded region shows night-time chemistry.

Figure 1.10 shows the mean diurnal and annual concentration profiles for NO_x and O_3 for 2019 measured across the UK's Automatic Urban and Rural Network (AURN) separated into urban traffic, urban background and rural background sites to provide some spatial variability - see section 1.5 for more details on the network and site types.

From figure 1.10, average hourly NO_x concentrations measured across the UK were between 7.7 and 111.0 ppbv. The highest were seen at urban traffic sites, during January at peaks in the morning an evening. The lowest were measured at rural background sites during August in the early morning. The diurnal profile at all the types of sites shows a double peak in the morning and evening which generally aligns with increased transport activity as people move to and from work and the largest values being measured at the roadside links this to road transport activity. The highest values are observed in the winter due to a combination of lower boundary layer (from cooler surface temperatures, section 1.1.1) and increased emissions from heating in buildings, a greater volume of and less efficient vehicle use.

For O_3 , UK wide hourly average concentrations ranged between 24.2 and 68.7 ppbv, however the trend in sites was reversed. Highest concentrations were seen at rural background sites, and the lowest at urban traffic sites. This is due to the suppression of O_3 production due to competition with radicals from NO_2 discussed earlier. Annually, ozone reaches an average monthly maxima in the spring and decreases to a minima during the winter, likely caused by variations in photochemical activity and influenced by anthropogenic activity, though no firm conclusion has been reached [41].

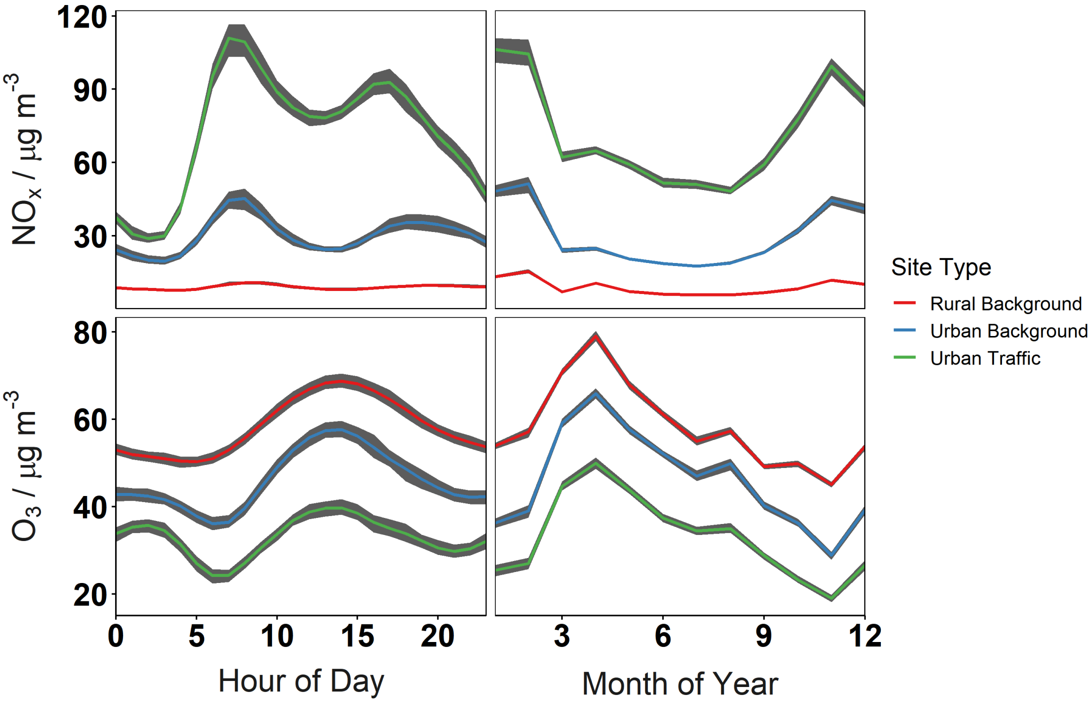

Figure 1.10: Diurnal (left) and annual (right) mean concentrations for NO$_x$ (top) O$_3$ (bottom) at rural background (red), urban background (blue) and urban traffic (green) sites in the Automatic Urban and Rural Network, UK for 2019.

1.4 Health Effects

1.4.1 Nitrogen Oxides

NO_x is of concern due to its aforementioned role in O_3 production and acute exposure to NO_2 can affect pulmonary function, inflame airways, increased risk of stroke, and lower birth weights [42, 43]. Exposure to high NO_2 concentration is required before acute effects are felt, and air quality objectives (table 1.1) reflect this, however, it is not uncommon in the urban environment for these objectives to be breached (see section 1.5). Those who have preexisting conditions, such as asthma or chronic obstructive pulmonary disease are more readily susceptible to the adverse effects of NO_2 [44]. As elevated NO_2 concentrations are closely linked with both increased $PM_{2.5}$ concentration, due to their shared sources, and O_3 formation, many more impacts of air pollution are linked with these directly and can be considered secondary effects of NO_2 emission.

1.4.2 Ozone

Ozone is of concern as an air pollutant to due to range of acute and chronic effects on human health. The impact has been linked to both concentrations commonly measured in and around urban areas, and breathing tidal volume, thus increasing susceptibility to the negative effects of O_3 during exercise [45]. Acute exposure to concentrations of ~160 μg m^{-3} have shown impacts on pulmonary function within 24 hours, increased hospital emissions of those with underlying respiratory conditions have been linked to concentrations less than 60 μg m^{-3} and people with implanted defibrillators are twice as likely to suffer an arrhythmia in the hour immediately following exposure to 44 μg m^{-3} [46–48]. This final effect is likely linked specifically to these underlying conditions, as in the study and review of ozone exposure "Multicenter Ozone Study in oldEr Subjects" the cardiovascular effects of O_3 in individuals without implanted defibrillators were not significant. The study did support that the effects on the pulmonary system at concentrations ~140 - 240 μg m^{-3} [49]. Long term effects of exposure to O_3 include links to the onset of asthma; in cases were regular (> 3 times per week) physical activity was conducted in with exposure to high O_3 (maximum 1-hour mean concentration of 151 μg m^{-3}) compared with similar activity in low O_3 environments (maximum 1-hour mean concentration of 95.2 μg m^{-3}) had a 3 fold risk of developing asthma [50]. Although it is not a direct health effect of O_3 , it should also me noted that elevated O_3 concentrations (> 35 ppbv) can impact crop yield, costing ~$20 billion globally across major agricultural crops [51, 52].

1.4.3 Particulate Matter

While particulate matter come in a range of sizes, the fine mode (diameter $< 2.5\ \mu$m) has the greater effects on health due to being *respirable*; being drawn deep into the lungs and depositing on the alveoli. Ultra-fine particles (diameter $< 0.1\ \mu$g) can diffuse into the blood and from there into other organs [53]. These are considered to have acute health effects, though longer term impacts are as yet unknown [54]. The larger particles (coarse mode, diameter $> 2.5\ \mu$m) are more readily trapped earlier in the respiratory system and are therefore less toxic [55]. $PM_{2.5}$ is linked exacerbation of respiratory and cardiovascular issues, and chronic increase in all cause mortality [56].

1.5 Air Quality Monitoring

Due to the adverse effects on human health there is cause for concern when their concentrations reach dangerous levels. Many countries adopt legal air quality objectives to codify poor air quality events. The UK has adopted a combination of EU air quality directives and its own national air quality objectives to form its set of limits (legally obligated to attain) and targets (to be attained where possible), some of which are summarised in table 1.1, [57, 58].

Table 1.1: Key UK air quality objectives, [57, 58]. The objectives for NO_2 and $PM_{2.5}$ are air quality limits which carry a legal obligation to maintain, whereas the objective for O_3 is considered a target, to maintained where necessary steps are not cost prohibitive.

Pollutant	Objective / μg m^{-3}	Number of Exceedances / yr^{-1}	Averaging Period
NO_x	200	8	hourly
$PM_{2.5}$	25	-	annual
O_3 *	100	10	8 hourly

To determine whether these air quality objectives are being met, ambient air quality must be monitored. The UK has implemented the Automatic Urban and Rural Network (AURN) managed by the Department for Environment, Food and Rural Affairs (Defra) [59]. The AURN consists of ~150 active sites (figure 1.11) each using standardised equipment and operating procedures generating comparable measurements across the country. Sites are classified based on their location e.g. traffic sites are situated close to the roadside whereas background sites are designed to be more representative of residential areas. They are also separated by urban or rural locations. Similar networks are implemented in countries across the world [60–62]. Additionally, some local authorities augment these networks with their own to increase the spatial resolution of measurements and improve the understanding of local pollution. The London Air Quality Network (LAQN, for site map see figure 3.1) is a good example of this, where sites additional to AURN are operated in the Greater London area and feed into air pollution forecasting for the area [63].

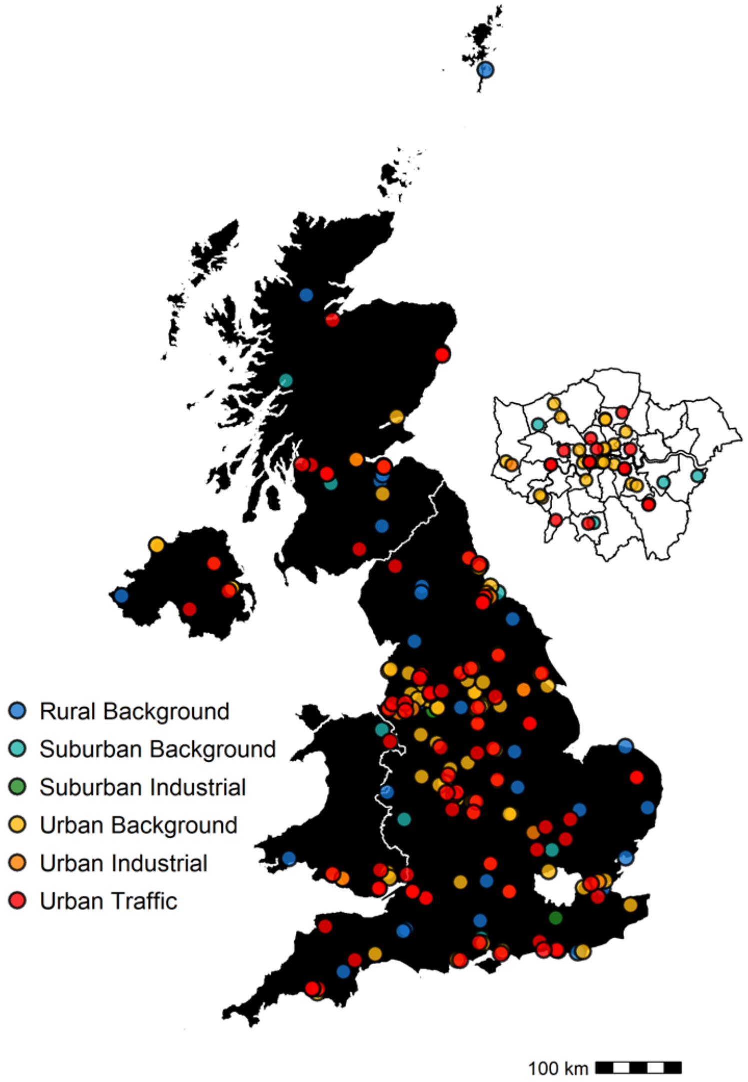

Figure 1.11: Map showing the location and type of AURN sites across the UK, reproduced from Lee et al. 2020 [64]

1.5.1 London Air Quality Network Case Study

Monitoring networks producing real time data allow for rapid analysis of unexpected events, which may not have been otherwise measured, such as the first *lockdown* implemented in many countries in the world, including the UK, in response to the SARS-CoV-2 pandemic. As a part of a wider analysis of the effects of the lockdown Lee et al. 2020 used the LAQN to contrast the number of exceedances of air quality objectives (table 1.1 for NO_2 and O_3 over the lockdown period compared to the previous 5 years [64].

Exceedances were calculated on a per site basis, and then summed across all sites of a given type. For NO_2 a simple one-hour mean was calculated and each hour greater than 200 μg m^{-3} was counted as an exceedance. For O_3 a rolling mean value was calculated, using a window of eight hours and a step size of one hour. If a given calendar day saw this rolling mean exceed

100 μg m^{-3} , an exceedance was counted. Using this method multiple exceedances (contiguous or separated in time) were only counted as one to avoid ambiguity in their definition, and therefore can be thought of as "days when an O_3 exceedance occurred".

Figure 1.12 shows the results for January – May 2020 and comparisons to those months in 2015—2019. A general downward trend of exceedances was found at roadside and kerbside sites in London, due to the continued reduction in NO_x emissions from the vehicle fleet. At kerbside, the number of exceedances dropped quickly from 2395 in 2015 to only 28 in 2019. At roadside sites, exceedances dropped consistently from 472 in 2015 to 45 in 2019, with almost all of the remaining 45 at two sites. From this it was hard to state whether the lockdown impacted NO_2 due to the already diminishing number of exceedances, but O_3 at urban background sites saw a clear increase in exceedances. Additionally, kerbside sites (those traffic/roadside sites that are extremely close the road traffic) saw some exceedances, which had not since at least 2015. This links strongly with the earlier discussion that reducing NO_x , without a corresponding reduction in NMVOCs can cause an increase in O_3 production before the transition to a NO_x limited system occurs.

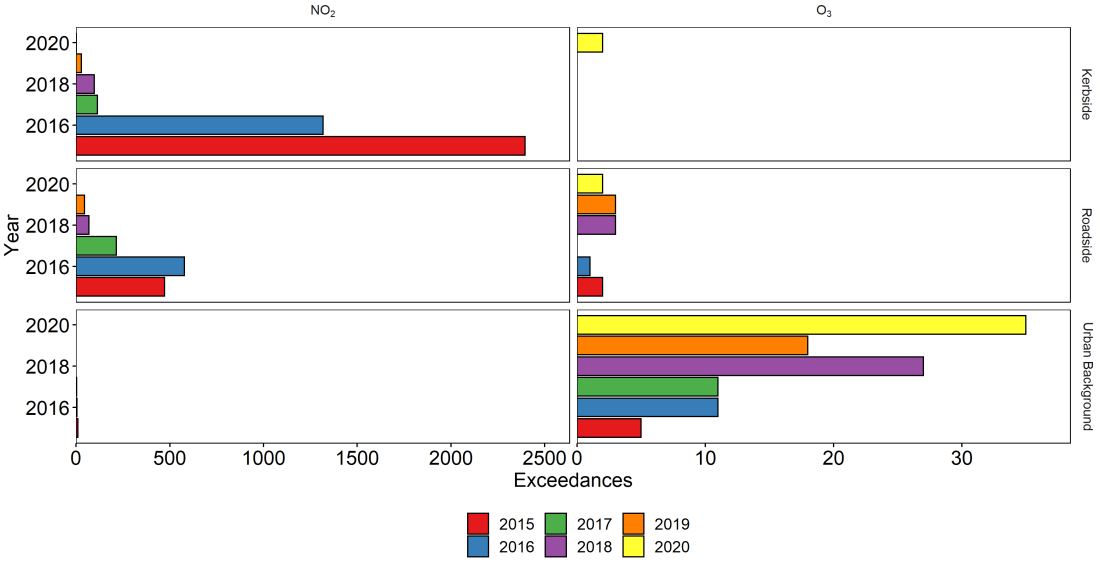

Figure 1.12: Exceedances of the UK air quality objectives for NO_2 and O_3 across the London Air Quality Network, reproduced from Lee et al. 2020 [64]

1.6 Thesis Outline

The following work in this thesis focuses on measuring NO_x emissions in two megacities. Chapter 2 describes the dual channel chemiluminescence NO and NO_2 analyser used to make many of the measurements in this work. It also discusses the background to the eddy covariance (EC) technique in detail along with introducing the software packages used for its implementation.

In chapter 3, a high time-resolution NO_x analyser was deployed to a tall tower site in central London, UK, during March - June 2017. These data were used to calculate NO_x fluxes via EC, and coupled with a footprint model to generate comparisons with the NAEI. This comparison found an average underestimation of the inventory by a factor of 1.4.

Chapter 4 reports data collected from two similar NO_x analysers deployed to two sites in Delhi, India, in October 2019. Again fluxes were calculated via EC and footprint models were run. An inventory developed by Indian Institute of Tropical Meteorology, Pune, the India Meteorological Department and the National Centre for Medium Range Weather Forecasting was used for comparison with the measured fluxes. Even an optimised version of the inventory was found to overestimate NO_x emission at both sites by 2 - 3 ×, but did capture the relative difference between them.

For chapter 5 NO_x concentrations in the London, UK, plume were measured from aboard the Facility for Airborne Atmospheric Measurements' BAE-146 aircraft on three flights; one in 2016 and two in 2017. These data are used in applying a mass balance approach to calculate the city's NO_x emission. The work aims to develop an applicable footprint from backwards particle dispersion data calculated using the Hybrid Single Particle Lagrangian Integrated Trajectory Model. This footprint was used to generate a comparable inventory estimate to compare the measurements too. The chapter discusses the effectiveness and future improvements of this method,

Finally chapter 6 summarises all the work presented here and considers how the research could be continued in the future.

Chapter 2

Eddy Covariance

The eddy covariance (EC) method is used to calculate the net flux of a scalar quantity involved in surface-atmosphere exchange. This can be a meteorological parameter such as latent/sensible heat, momentum for use in energy budget closure or a trace gas. Greenhouse gases (GHGs) such as CO_2 and CH_4 have been studied extensively in this manner and often focus their measurements over agricultural fields or natural surfaces such as forests or wetlands. Large numbers of these sites form long-term networks assessing GHG budgets. There has been increased use of EC to measure emissions over urban areas covering both GHGs and pollutants important to air quality [65–69].

Combining high time resolution measurements (on the order of 5-20 Hz) of vertical wind speed and a scalar EC provides the means to calculate the vertical flux of that scalar. The method is rooted in considering the atmosphere as a turbulent system, operating over a range of time and length scales. The eddies from which the methods name is derived are a property of this turbulence are considered responsible for vertical transport. In this context, emission can be considered as an increase in concentration as an eddy moves air from below the sample point up past it, resulting in positive covariance between vertical wind and concentration. These eddies turn over on scales ranging from sub second to hours, however those in the middle are often responsible for the bulk of the transport. By measuring at a fast-enough time scale a large range of these eddies can be captured. The covariance calculated for a given aggregation period, often on the order of 30 minutes - 2 hours, results in a net emission or deposition per period.

2.1 Measuring NO_x at High Time Resolution

NO and NO_2 concentrations were measured using an Air Quality Design (AQD) dual channel chemiluminescence analyser. A version of the instrument operating at high time resolution (5 Hz) was used for eddy covariance in chapters 3 and 4 and a second version was run on the Facility for Airborne Atmospheric Measurement's (FAAM) BAe-146 aircraft to collect the data used in chapter 5. The instruments are similar but not identical - the following provides a general description of the instruments based mainly upon the one used for 5 Hz tower based measurements.

2.1.1 Principle of Operation

Instrument Overview

The instrument consists of two channels, one measuring NO and another measuring NO_x. The difference between these channels provides NO_2. The sample is pressure controlled to 300 Torr upon entering the inlet box, and is then split into the two channels, both immediately passing through a mass flow controller set to 1.2 lpm. Channel two passes through a blue-light converter (BLC - see NO_2 Conversion below) while channel one contains tubing that is of equal volume to the route via the BLC, to keep the samples synchronised. After conversion the samples leave the inlet box and pass to the detector. The detector box contains the pre-reaction chambers, photomultiplier tubes (PMTs) and the detectors. O_3 is created in the ozoniser box both flowing O_2 through coronal discharge tubes and introduced to the sample in either before or after the pre-reaction chambers. In normal operation the O_3 is introduced after these chambers such that chemiluminescence occurs in the PMTs. Introducing the O_3 before these chambers means the chemiluminescence occurs before reaching the PMTs, and allows a zero reading to be taken in the absence of a zero air source. In practise both of these methods are used together to provide a higher quality zero. Calibration gas and a second source of O_3 for gas phase titration can be introduced before the BLC in the inlet box. Schematics are shown in figures 2.1-2.4,

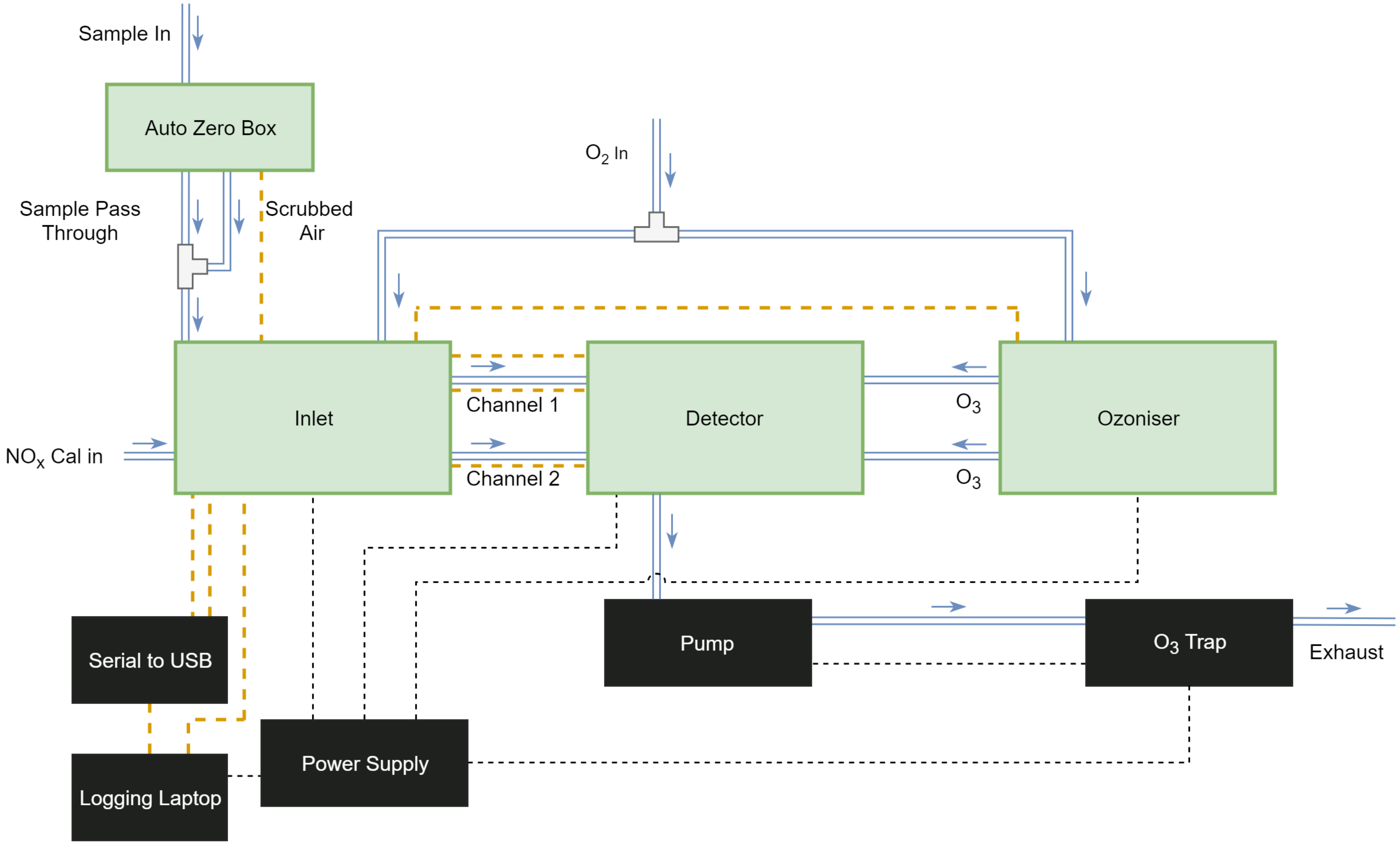

Figure 2.1: Plumbing Diagram for the Air Quality Design NO$_x$ analyser. The four instrument boxes are shown in green. Tubing for gas flow is shown by blue double strokes, with flow direction marked by arrows. Orange dashed lines show communication and control connections. Black lines show power connections. Internal diagrams of the inlet, detector and ozoniser are shown in figures 2.2-2.4

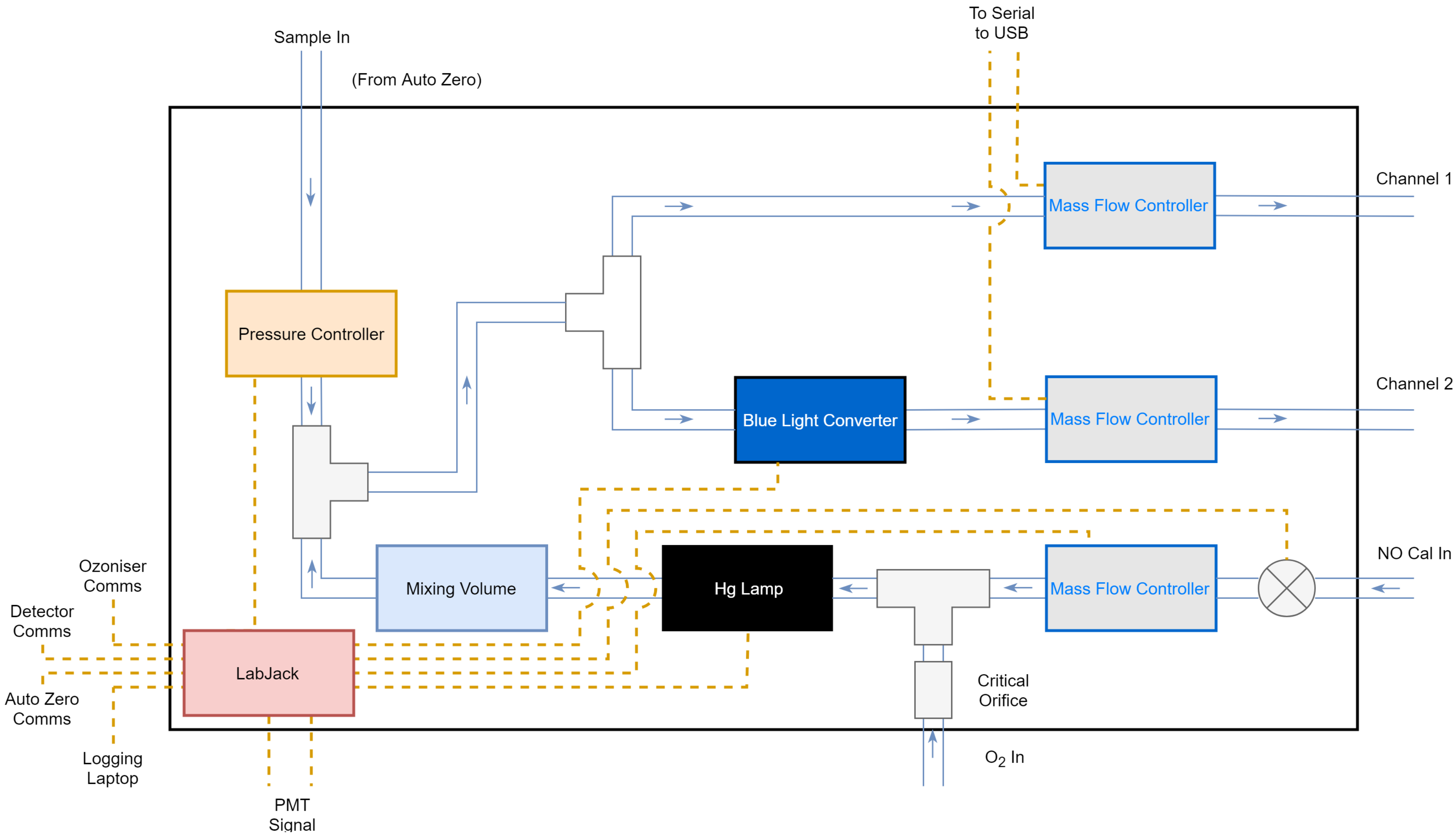

Figure 2.2: Plumbing Diagram for the Air Quality Design NO_x analyser inlet.

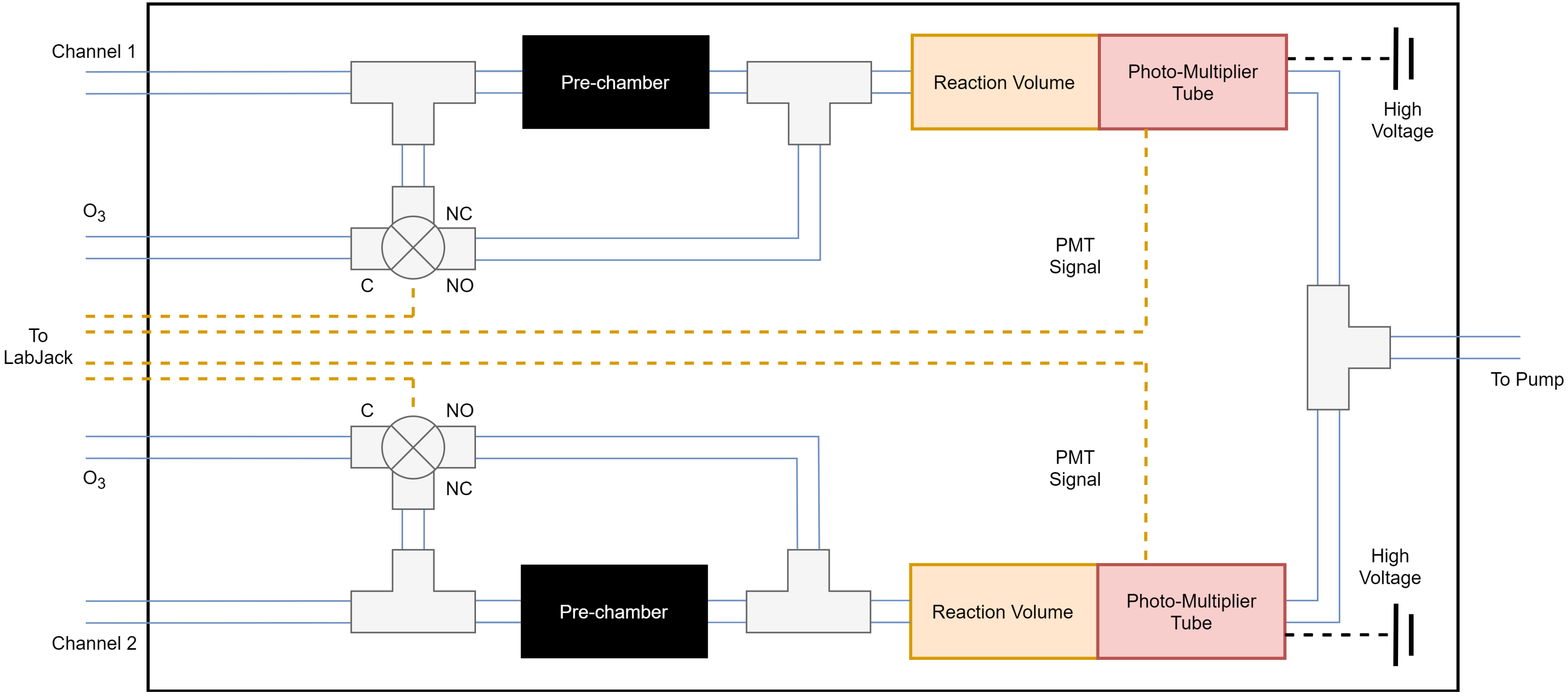

Figure 2.3: Plumbing Diagram for the Air Quality Design NO_x analyser detector.

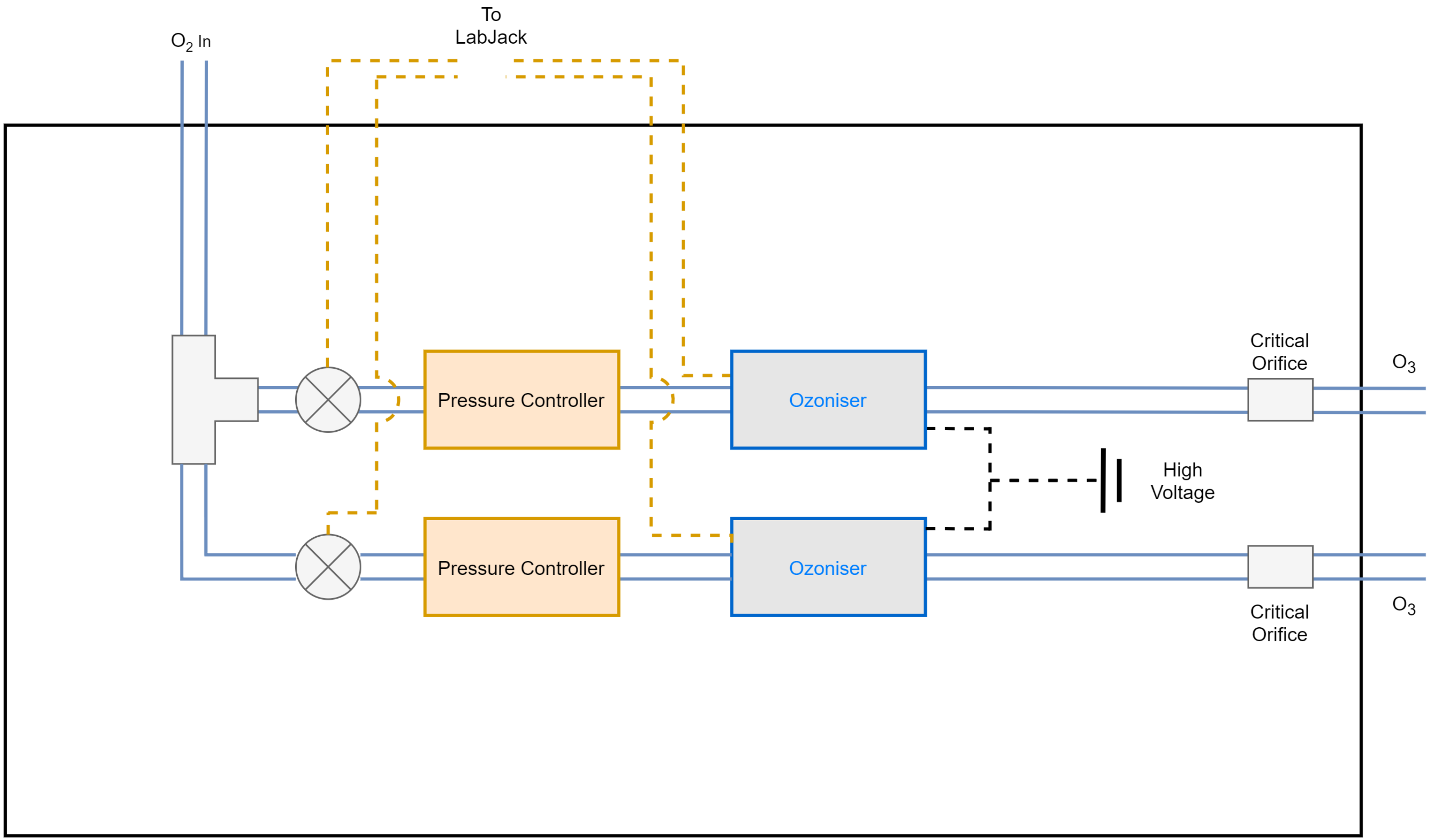

Figure 2.4: Plumbing Diagram for the Air Quality Design NO_x analyser ozoniser.

Detecting NO via Chemiluminescence

NO is detected in each channel via chemiluminescence, whereby the reaction of NO with O_3 creates an excited state of NO_2 which subsequently relaxes via emission of a photon (chemical equations R 2.21 and R 2.22). As the number of photons released is proportional to original concentration of NO, photon counting can be employed to determine the NO concentration.

$$\mathrm{NO} + \mathrm{O_3} \longrightarrow \mathrm{NO_2}^* + \mathrm{O_2} \tag{R 2.21}$$

$$\mathrm{NO_2}^* \longrightarrow \mathrm{NO_2} + \mathrm{h}\nu \tag{R 2.22}$$

This technique is employed in both channels of the instrument, where the first channel measures NO, and the second measures NO plus a percentage of NO_2, depending on the conversion efficiency (CE). The uncorrected measurement from this channel is referred to as NO_c as to separate it from NO_2.

NO_2 Conversion

When measuring NO_2, it is currently more common to convert NO_2 to NO, and calculate the difference between this and a NO measurement. Direct measurements of NO_2 are available via methods such as cavity attenuated phase shift (CAPS) or laser induced fluorescence (LIF), but are less well established [70, 71]. Two indirect methods for NO_2 to NO conversion employ molybdenum or blue-light converters. These conversion units are commonly referred to as moly and BLC respectively. Moly converters reduce NO_2 to NO by flowing the gas over a heated (> 325 °C) Mo catalyst. This methods enjoys a high CE, often > 95 %, but suffers from interferences from other oxides of nitrogen (HNO_3, PAN, HONO, $RONO_2$ etc) [72]. BLCs use an array of diodes centred about a specific wavelength < 410 nm to photolytically reduce NO_2 to NO (R 1.9). The AQD instrument uses a diode centred on 395 nm to avoid interferences from other species which will also photolytically reduce to produce NO at these short wavelengths [73]. The additional benefit to using a BLC is the smaller photolysis cell volume compared with the volume of the cavity in a CAPS. The smaller volume allows the instrument to operate at a higher time resolution as the cell is flushed more frequently.

$$\mathrm{NO_2} \xrightarrow{\mathrm{h}\nu\,<\,420\,\mathrm{nm}} \mathrm{NO} + \mathrm{O}(^3\mathrm{P}) \tag{R 1.9}$$

2.1.2 Calibration Procedure

To calibrate the instrument, the zero and sensitivity for each channel must be determined, along with the CE of the BLC. When the instrument is deployed in the field, it is a equipped with an auto-zero box connected between the sample line and inlet box. This box contains a three-way valve and NO_x trap. In the trap the sample first passes through Sofnofil to oxidise NO to NO_2, which is then scrubbed using activated charcoal. Using the three-way valve to connect the instrument to scrubbed ambient air, a regular in-field zero can be taken. Under normal operation this zero lasts for 2 minutes and is triggered once an hour. This zero air is also used as the sample when sensitivities and conversion efficiency are being determined.

Sensitivities and CE require a NO source to calibrate. This process takes ~20 minutes to complete so at tower sites the cycle is run automatically every n hours, where n is chosen to spread the calibration through the diurnal cycle, e.g. 61 hours was used at the BT Tower in 2017. On the aircraft a calibration is run on the ground before and after flight and is triggered by the operator during the flight when possible. A ~5 ppmv cylinder is diluted into the instruments flow via a mass flow controller. Knowing the flow through the instrument and cylinder concentration the NO sensitivity in each channel can be span calibrated. The sensitivity is expressed as the number of counts per 1 pptv of NO. CE is determined using gas phase titration (GPT). O_2 is flowed over through a UV titration cell, in which the lamp is pulsed several times a second using a square wave generator to create a supply of O_3 which is mixed with the NO span gas. The lamp pulse rate is set to titrate ~50 % of the span NO. This to balance having both low signal to noise in the residual NO and a dilution such that this value is significantly different from the pre-dilution concentration. It should be noted that the exact dilution amount does not matter as long as it is within range and stable, as determination of CE is independent of absolute NO_2 concentration. Figure 2.5 shows an example calibration sequence and equation 2.1 shows how the CE is calculated from average concentrations of an invariant input concentration of span gas, C. Whether the GPT system and BLC are on/off is denoted by the 1/0 respectively. The denominator of equation 2.1 represents the amount of NO_2 being produced by the GPT system. This is the difference between the titrated/un-titrated NO signal with the blue light converter disabled. The numerator represents how much of the NO_2 created by the GPT system is measured. Note here that the BLC is enabled in both the titrated and un-titrated cases such that any residual NO_2 in the calibration source cancels out, as it will be present in both signals.

$$CE = 1 - \frac{C_{(GPT\_0,BLC\_1)} - C_{(GPT\_1,BLC\_1)}}{C_{(GPT\_0,BLC\_0)} - C_{(GPT\_1,BLC\_0)}} \tag{2.1}$$

NO and NO_2 concentrations are calculated from the channel sensitivities and CE, shown by equations 2.2 and 2.3. These are then summed to provide total NO_x.

$$NO_{conc} = \frac{Counts_{\ ch2} - Zero_{\ ch2}}{Sensitivity_{\ ch2}} \tag{2.2}$$

$$NO_{2\ conc} = \frac{\frac{Counts_{\ ch1} - Zero_{\ ch1}}{Sensitivity_{\ ch1}} - NO_{conc}}{CE} \tag{2.3}$$

One aspect of NO_x measurement that is not accounted for in this calibration procedure are instrument artefacts, which can be due to interfering reactive nitrogen species that can form NO within the instrument [73, 74]. This is primarily an issue when measuring low concentrations of NO_x (in the pptv range) where the artefact makes up a significant proportion of the measurement [75]. In the urban environment, this can be neglected.

2.1.3 Instrument Uncertainty

The instrument uncertainty is given by the precision which is based upon the limit of detection (LOD), and accuracy, which is calculated from the combination of several percentage uncertainties from component calibration. Each channel of the instrument has a precision and accuracy associated with it, resulting in the uncertainty in NO_2 concentrations being a combination of the uncertainties in NO and NO_x.

The accuracy for the NO and NO_x channels, totalling 3 %, is the combination in quadrature of:

- sample flow mass flow controller, 2 %
- calibration gas mass flow controller, 2 %
- calibration gas certification usually supplied as < 1 %, = 1 % is used in these calculations.

The NO_2 measurement is then the combination of these and the uncertainty in the determination of the calibration efficiency - which repeated calibrations in the laboratory gave as 0.63 % at 1 sigma, along with the mass flow controller in the gas blender use to perform the gas phase titration (2 %). This results in an uncertainty in NO_2 of 4.7 %.

The limit of detection calculated as the 3 sigma variance in instrument signal when sampling zero air. A conservative estimate can be gained from simply calculating the standard deviation of a zero signal as has been performed in chapters 3 and 4 (~170 pptv at 5 Hz) or via Allen variance which additionally accounts for systematic drift in the instrument over longer time periods, but also provides a more accurate estimate. This latter method is used when calibrating the NO_x instrument used on the aircraft in chapter 5, as higher precision is desirable for some clean atmosphere measurements (~40 pptv at 1 Hz). In this work measuring

NO_x in urban settings, the limit of detection is sufficiently low that it can be neglected, especially when compared with the random error of the eddy covariance calculations.

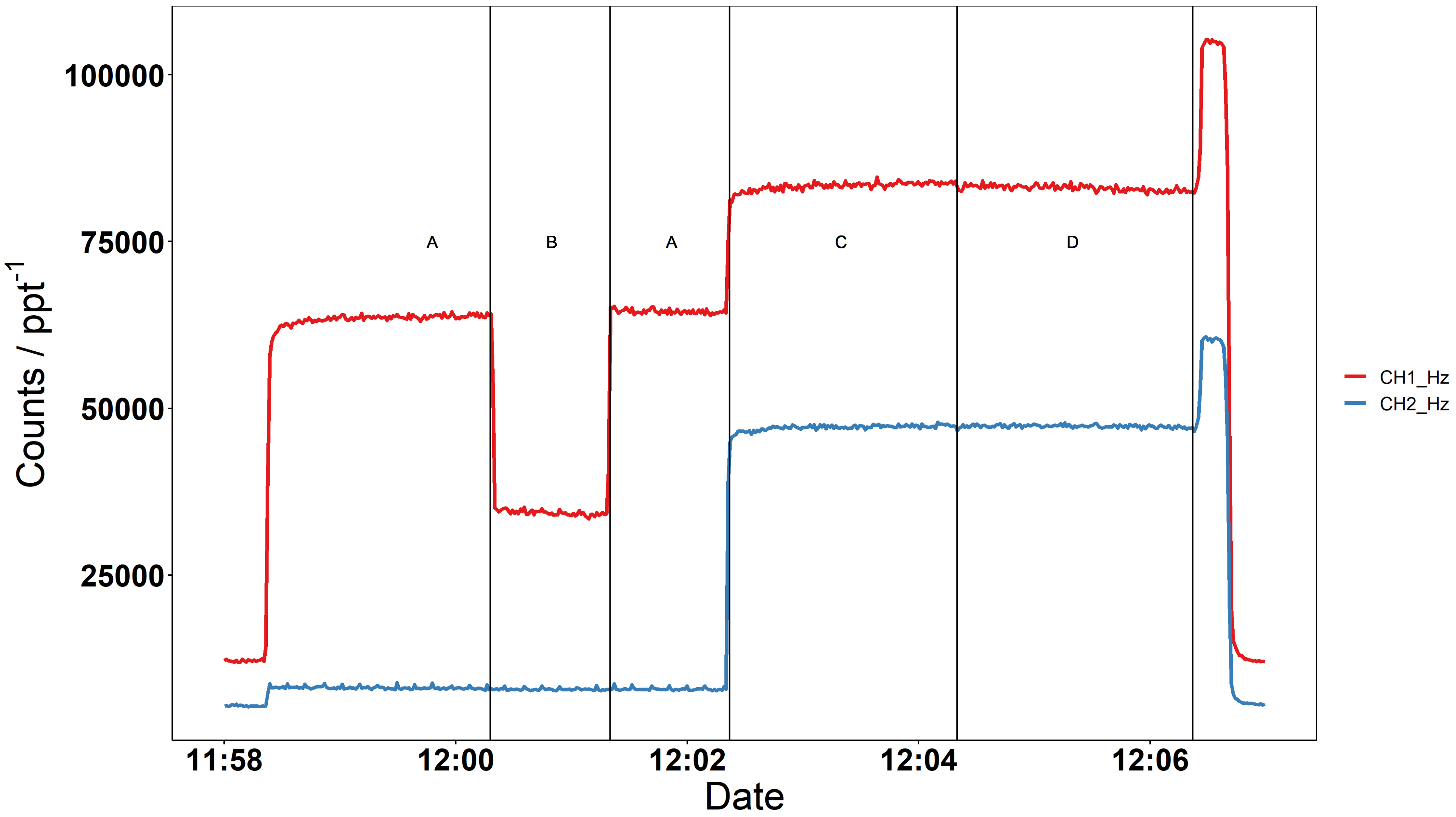

Figure 2.5: Example NO_x calibration cycle. Segment C contains the response used to calibrate the sensitivities of each channel for use in equation 2.2. The conversion efficiency terms in equation 2.1 correspond as follows A: GPT_1,BLC_1, B:GPT_1,BLC_0, C:GPT_0,BLC_1, D: GPT_0,BLC_0

2.2 The Eddy Covariance Method

Calculating the emission of air pollutants using EC is not a trivial task. Not only does it require fast, accurate gas analysers, but also fast micrometeorological data from a 3-D sonic anemometer. Data from the sensors must be high quality data and have good temporal coverage before beginning the calculation. Additionally, these sensors must be located such that they are above the canopy or urban roughness layer, ~2 - 3 × the building height, as below this momentum flux cannot be assumed to be constant. The fluxes generated must be assessed such that they have been calculated during periods where the criteria for valid application of EC are met and, in the case where surface fluxes are being presented, the calculated fluxes are connected to the surface. In the case of urban EC where the surface is extremely heterogeneous not only must the fluxes be connected to the surface, but also what part of the surface is the flux related to. Furthermore, decisions must be made about how to process the data during the calculation and depend on many factors such as site, sensor, scalar,etc. Sections 2.2.2 - 2.2.3 cover how each of these steps is tackled. In addition to the references herein, this section has taken much inspiration from Burba 2013, Lee et al. 2005 and Aubinet et al. 2012 [76–78].

2.2.1 Eddy Covariance Theory

EC makes use of the turbulent structure of the atmospheric boundary layer (ABL), which makes up the lower portion of the troposphere (section 1.1.1). The ABL is the portion of the atmosphere where the influence of the surface dominates its behaviour. It is usually separated from the free troposphere by a temperature inversion across which mixing is limited. In the ABL this turbulence is responsible for the majority of vertical transport, whether it is driven by buoyancy or wind shear. Because of this, the relationship between vertical wind speed (w) and a scalar quantity measured aloft (c) is related to the flux of the scalar. Flux can be simply defined as the movement of a scalar though a unit area in unit time and in the case of gaseous scalars, positive flux is an emission from the surface and negative flux a deposition or loss to the surface. The covariance between the instantaneous components of vertical wind speed (w') and scalar (c') allows the magnitude of this flux to be calculated. This is derived via Reynolds decomposition of the equation for turbulent flux (equations 2.4 - 2.9 present this calculation as Burba 2013 [76]). Reynolds decomposition is the separation of a signal into its mean (overbar) and fluctuating (prime) components and is governed by three rules:

1. The mean product of two variables as two components, the product of the individual means, and the mean of the product of their fluctuations, equivalent to the covariance
2. The mean of an individual fluctuating component is zero

3. The mean of the sum of two components is equivalent to the sum of the means of the components

Equation for vertical flux

$$F = \overline{\rho_d w c} \tag{2.4}$$

Apply Reynolds decomposition

$$F = \overline{(\overline{\rho_d} + \rho'_d)(\overline{w} + w')(\overline{c} + c')} \tag{2.5}$$

Expand terms

$$F = \overline{(\bar{\rho}_d \bar{w} \bar{s} + \bar{\rho}_d \bar{w} s' + \bar{\rho}_d w' \bar{s} + \bar{\rho}_d w' s' + \rho'_d \bar{w} \bar{s} + \rho'_d \bar{w} s' + \rho'_d w' \bar{s} + \rho'_d w' s')} \tag{2.6}$$

A lone deviation from the mean is zero when averaged, all terms containing just one are removed

$$F \approx \overline{(\bar{\rho}_d \bar{w} \bar{s} + \bar{\rho}_d w' s' + \rho'_d \bar{w} s' + \rho'_d w' \bar{s} + \rho'_d w' s')} \tag{2.7}$$

Two assumptions are made:
— First is that deviation in the density of air is negligible

$$F \approx \overline{(\bar{\rho}_d \bar{w} \bar{s} + \bar{\rho}_d w' s')} \tag{2.8}$$

— Second that the mean vertical wind is zero (i.e. no air is being lost or gained vertically in the system)

$$F \approx \overline{\rho_d w' c'} \tag{2.9}$$

With this the practical equation for eddy flux equation is left 2.9.

w′ and c′ in equation 2.9 by definition correspond to the fluctuating component of their respective signals, which provides the measurement of the turbulence. The turbulence is considered as being made up of various sized *eddies*, from which the technique derives its name. These eddies turn over on scales ranging from sub-second to hours and are used to select the bounds for the measurement. Fast instrumentation (5 - 20 Hz) is required to capture the high frequency eddies, and aggregation periods must be selected to enclose the bulk of large eddies responsible for vertical transport. See *Defining Aggregation Periods* in section 2.2.2 for more details. EC often utilises a single point measurement to gather information on these eddies, especially in the urban setting where site selection is limited by many external factors, and as such makes use of Taylor's hypothesis of frozen turbulence, which states that turbulent air is advected past a fixed point with essentially no change to the eddy structure, providing that the mean flow dominates over the intensity of the turbulence [14]. By this, it is assumed that the properties measured through a single point measurement apply to the whole eddy as they are not changed by the horizontal advection. The covariance of the instantaneous vertical wind and the scalar of choice is then analogous with the eddy turn over. An updraught associated with an increase in concentration is an eddy transporting an air parcel of higher concentration from below past the measurement point, and can be considered an emission. The alternative of an updraught being associated with a decrease in concentration corresponds to a deposition. The average of these over a period deemed to be capturing all significant eddy sizes provides the measurement of the net flux of the scalar.

2.2.2 Flux Calculation

This section discussed the various steps corrections and transformations applied to the data for a general flux calculation on which the analyses presented in this thesis are based upon. There are two broad categories of steps, those applied to the high-time resolution data and those applied to the averaged parameters - including the covariances. Those noted here are applied whilst running the eddy4R workflows (section 2.3). There are other quality criteria for input data, but these are applied in the pre-processing and data workup stages, relating more to sensor correction and attempt to address many of the problems noted by Vickers and Mahrt 1997 [79]. Figure 2.6 provides a schematic of these steps.

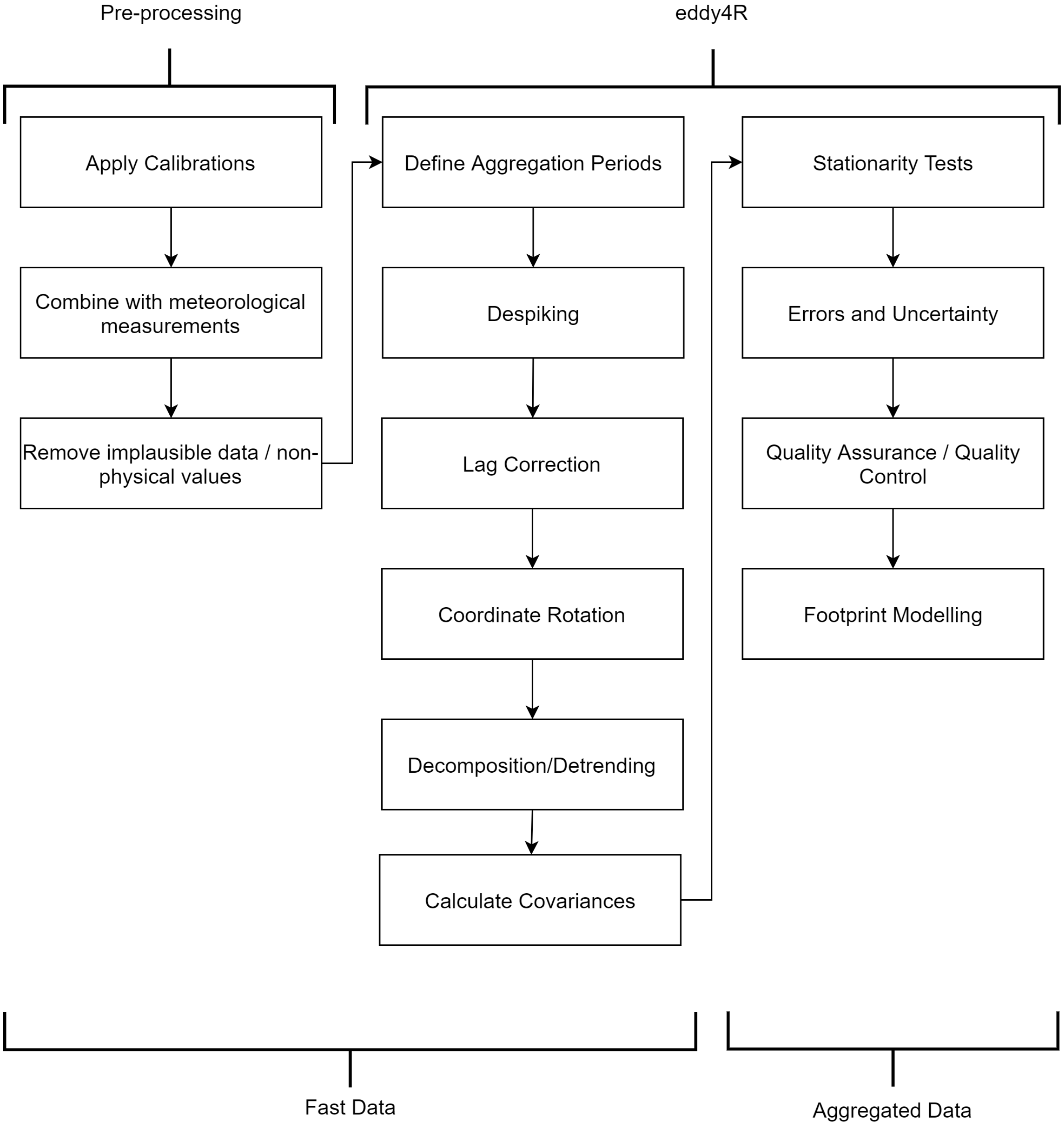

Figure 2.6: General overview of steps taken to process eddy covariance data throughout this thesis.

Defining Aggregation Periods

It is necessary to calculate the average flux over a short period, rather than for the whole data set (or even daily) as the turbulence responsible for vertical transport of the emission is being considered. When aggregation periods are extended to lengths greater than 2-6 hours as larger, non turbulent, scale processes can begin to be captured [80]. This must be done whilst not having too short an averaging period that large eddies that do contribute to the flux are missed. Commonly these periods range from 30 mins – 4 hours. Optimum ranges can be defined through the analysis of Ogive spectra (integration under the cospectra), or repeating the flux calculation using sensible averaging periods, and attempting to locate a maxima in the cumulative flux, before it is increased by larger scale processes. To simplify data analysis the latter is used for work in this thesis.

Despiking

Despiking is designed to remove artificial spikes in data, often caused by electronics within the instruments. The exact criteria for despiking algorithms is instrument dependant, but usually defines a spike as a short set of data points (3-5) that fall outside of 3-8 standard deviations from surrounding points. The points are removed and can then be filled using linear interpolation or alternatives. Smaller spikes are often also flagged through the use of range tests, where a range of values that would be considered sensible for a given sensor are provided, and aggregation periods that contain data outside of this range are penalised during quality control [81, 82].

Lag Correction

Data used for EC must undergo a correction for the time lag between different sensors. EC experiments are designed such that the inlet and sonic anemometer are co-located and therefore are sampling the same air mass. However, it often not practical to locate closed-path gas analysers alongside the anemometer. Instead the air is pumped though a sample line to the instrument at high flow rates to maintain turbulent flow in the line, preventing signal attenuation when flows are laminar. As such there is a delay between the air mass entering the inlet and being sampled at the instrument. For each flux averaging period, a time lag is determined by calculating the maximum cross-correlation between the w wind vector and scalar quantity time series, and then shifting the scalar in time based on this. This process is usually applied iteratively, as cross-correlation can give false positives when there is not strong covariance. Firstly the cross-correlation is run with no restrictions, then the lag time data is examined and a window enforced on the function - if the lag determined by cross-correlation falls outside of this window, a median or modal lag time is used instead.

Coordinate Rotation

Coordinate rotation is performed due to sonic anemometers rarely being aligned into the mean wind, and often with the u and v wind vectors contaminating the w vector. There are a number of methods to correct for this, but most are a variation of either double rotation or planar fit. As the name suggests double rotation consists of two single rotations and are calculated per flux aggregation period. The first is a rotation into the mean wind by calculating a rotation such that the mean u is zero, which aligns v with the y axis. This is followed by a second rotation such that the mean w is zero. Double rotation is often used as the corrections are simple to calculate and it can be used when limited measurements are available. However, assumption that mean w is zero over the aggregation period is not necessarily correct, especially when an aggregation period is short. The method is also subject to over rotation when anomalies in flows during one aggregation period cause the rotations applied to be disproportionate [83]. Planar fit uses wind measurements collected over longer periods to define the corrections that should be applied to wind vectors [84]. The underling idea is that these parameters collected over longer periods are based upon the mean flows at site and w is then corrected to perpendicular to this plane. Over more complex terrain a plane can be defined based on wind sector to capture how this affects the flow. As noted already this technique requires periods of days to months to determine the parameters, especially if one wishes to determine multiple planes for a site and as such limits the methods efficacy in the case of shorter campaign based EC measurements [85].

Decomposition/Detrending

Eddy covariance requires the fluctuating components of the vertical wind speed w' and scalar c' to be defined. In the simplest case these are the deviations from the mean over a given time period; Reynolds decomposition. In the case of complex surfaces, strong diurnal patterns in the scalar or sensor drifts, which would otherwise introduce non-stationarity, other methods can be employed. Linear detrending is a simple way to reduce the influence of these external factors and is achieved by fitting a linear trend across the flux aggregation period and subtracting this from the data. More complex trends can be removed by fitting polynomials or using running means. However, care must be taken as detrending operates as a high pass filter which could remove frequencies that are responsible for flux, reducing the overall flux calculated. The detrending method must be weighed at each site and for each scalar.

Stationarity

Stationarity is a criterion that should be fulfilled for the time aggregation of fluxes to be valid. In general, a stochastic signal is considered stationary if its statistics are time independent. A practical way to conceptualise this is to consider a signals mean and variance. If the signal is truly stationary the mean and variance of any subsection of the signal should equal that of any other subsection, and that of the whole signal. Crucially, when a signal is stationary, an ensemble average (i.e. if the experiment were to be repeated from identical starting conditions, but had differing results due to the random nature of turbulence) would be equivalent to a temporal average. It is this point that validates the aggregation of fluxes over time. This definition of stationarity is based off of idealised systems but when it comes to measuring in the atmosphere conditions do change and hence imbues a level of non-stationarity in the system. Therefore, it must be decided whether or not a flux is *stationary enough*. To determine this a test is performed similar to the practical analogy above. The flux is first calculated for the whole aggregation period, and then for contiguous samples of the period i.e. 1 x 30 minute flux and 6 x 5 minute fluxes. The fluxes from these subsamples are compared with that for the whole period and if any fall outside of a threshold (usually in the range of 30 - 60 %) the period is flagged for non-stationarity [86].

Random and Systematic Errors

Random and systematic errors in fluxes are linked to the eddy scales being measured. Systematic error is due to eddy scales which contribute to the measured flux being larger than the flux aggregation period or smaller than the instrument sampling resolution. Random error is due to a record not being significantly long enough to capture the full behaviour of the turbulence and consider the turbulence as an ergodic process - a process that any sample of sufficient length is representative of the whole process. Using a 1 hour long aggregation period as an example, in terms of systematic error, eddies greater than 1 hour in scale will not be fully captured and if significant, lead to underestimation of the flux [87, 88].Equally, if sampling was occurring at lower altitudes (e.g. 5 m) using a 5 Hz instrument, systematic error would arise from high-frequency losses, as at these heights < 5 Hz eddy scales make a significant contribution to the flux. For the random error, if a major transporting eddy was found to be on the 15 minute scale, only 3 - 4 samples of this eddy scale can be included, reducing the overall confidence in this record. Errors are calculated after the methods outlined by Mann and Lenschow et al. 1994 [89]. Practically these are limited by the need to avoid non-stationarity - decomposition must occur on timescales ~1 hour to avoid things such as boundary layer growth - and study focus. Those presented in this thesis were focused on sub daily variations in emission, so are time averaged to 1 hour to preserve the diurnal cycle. Errors are reduced by forming the average diurnal as a psuedo-ensemble average, which does invoke the assumption that emission across the averaged days are comparable. The combined random and systematic error is a useful data filter and individual points where this value was greater than 150 % were removed in the analyses in later chapters. When diurnally averaged these errors provided uncertainty ranges for the measured flux on the order of order of ± 25 - 50 %.

2.2.3 Footprint Modelling

Now the flux has been calculated, it can be related to the surface. This is achieved using a footprint model. When flux is measured in areas that have homogeneous surface coverage the terrain can be assumed to influencing the response the same per unit area. As such the primary function in these regimes is to estimate total area responsible for the signal. However, with flux being measured more frequently in increasingly heterogeneous terrains – including highly heterogeneous urban areas – the need for footprint modelling to aid both site selection and the interpretation of data has increased [65–68, 90–92].

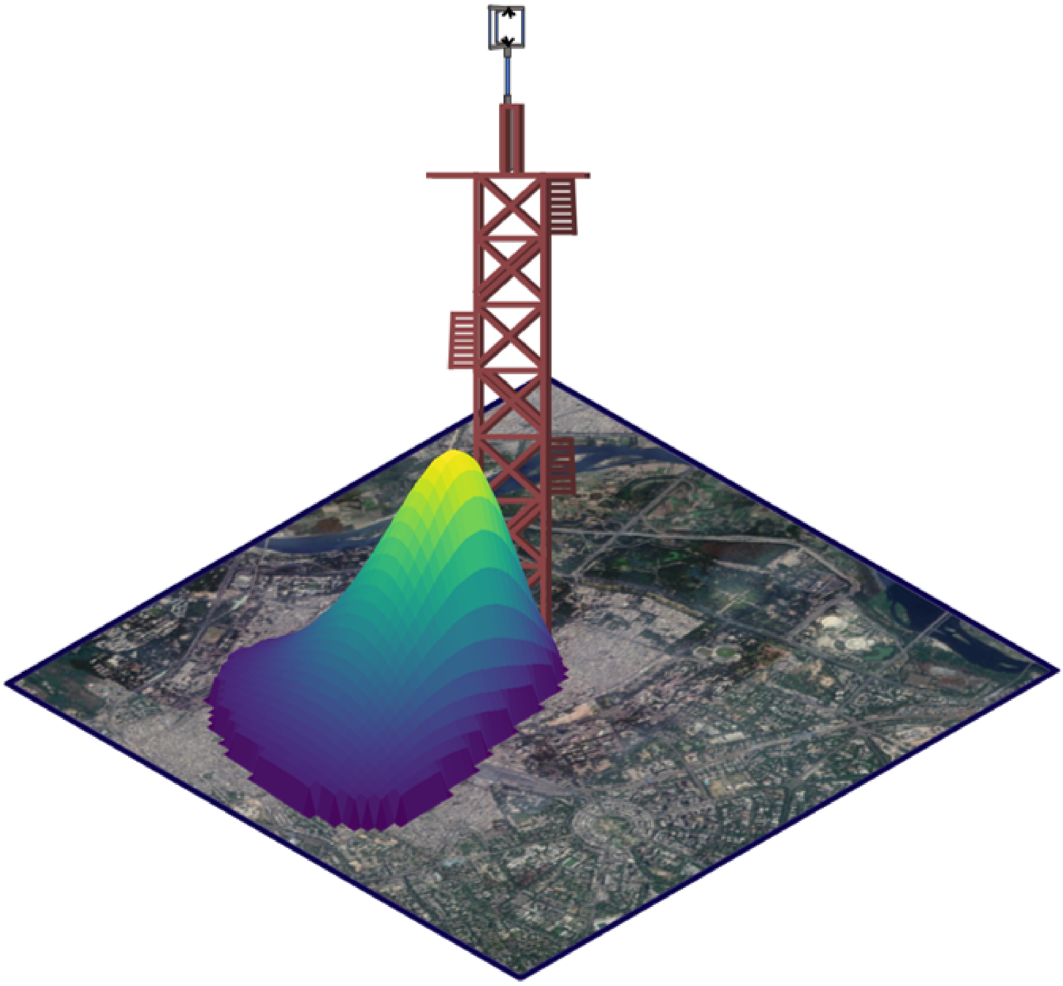

Figure 2.7: Schematic footprint example; calculated footprint provides an area from which the measured flux originated.

For this more complex scenario the footprint model needs to provide more detailed information - crucially it must place the receptor in space relative to the surface being sampled. Vesala et al, 2008 gives a comparison between three more recently used methods; Lagrangian stochastic particle dispersion models (LPDM), large eddy simulations (LES), and ensemble-averaged closure models [93]. The history of the development of some of these methods, along with a discussion of the mathematics behind the idea of a footprint is covered by Schmid 2002 [94]. LPDM forms the basis to support the EC measurements in this thesis. The LPDM can be used with either forward or backward particle trajectories. Forward can be viewed as modelling a tracer release and observing what particles reach the downwind sensor - where the more that reach the sensor the more that location contributes to the footprint. Backward calculates the particle trajectories in negative time steps from the sensor, and those that touch down contribute to the footprint. A drawback to LPDM is that running the simulations are computationally expensive and as such are often impractical for measurement campaigns. A parameterisation of a LPDM-B for a range of meteorological conditions and receptor heights by Kljun et al. 2004 alleviates the need to run these more expensive models in a large amount of cases [95]. The method aims to provide a general cross-wind integrated footprint function (F^*) as a function of its along-wind distance (X^*), based upon footprints generated by the dispersion modelling. The footprint model parameterisation is based upon the following parameters. The footprint's extent is bounded by the time taken for a particle to reach the receptor height (z_m), and the furthest distance in which turbulence within the boundary layer moves relevant air masses past the receptor location. The standard deviation of the vertical wind component (σ_w) provides a relationship with rate of vertical transport by buoyancy and friction velocity (u^*) a relationship with transport due to turbulence. Boundary layer height (h) provides a bound for the largest eddy sizes that can feasibly contribute to measured flux. The surface roughness length (z_o) scales the model for various emissions surfaces. The along-wind distance from the receptor (which is theoretically bounded by the previous conditions) is noted as x. By scaling a generalised non-dimensional footprint in terms of these parameters a comparatively computational cheap model is created and can be run along side the flux calculations, or iterated over quickly during post-processing analyses.

The footprint parameterisation has been further extended into two dimensions using a Gaussian distribution driven by the standard deviation in the cross-wind component (σ_v) as in Kljun et al. 2015 and Metzger et al. 2012 [96, 97].

Once calculated, these footprints provide spatial information of the contribution to the measured flux. These can be projected onto inventories or other land use maps in an attempt to provide context to the measurement, or in the case of the inventories, evaluate the quality of their estimates.

2.3 eddy4R

eddy4R is an open source collection of R packages - primarily developed at the National Ecology Observatory Network (NEON) in Boulder Colorado - which provides a modular set of tools for producing eddy covariance workflows [98]. Fluxes calculated in chapters 3 and 4 have used these software packages. Additionally, code developed for the processing of chemical fluxes during this work has been contributed to the eddy4R repositories. These contributions allowed for n different chemical species to be processed in parallel, e.g NO, NO_2 and CO simultaneously [68], and have since been used in the processing of fluxes of many VOC species in Delhi and in a eddy covariance methods intercomparison exercise [99, 100]. This is not something that is currently available in the widely used EddyPro software (as of version 7.0.6 [101]) where the user is limited to one custom scalar beyond CO_2, H_2O and CH_4. A key advantage of eddy4R is this focus on wide community collaboration and has received contributions from many sources meaning cross discipline expertise is available to users.

In addition to contributes made to the central code base, the modular nature allowed additional customisation of the workflow. These included error handling procedures to minimise the data pre-processing steps. The workflow was built to be able to fail gracefully at most stages without interrupting the overall processing and instead move onto the next flux aggregation period to be processed, logging the failure and its associated error for review. To support this various simple tests were standardised and applied to the input data (e.g that all required columns were present, and that the data contained within them was present in sufficient quantity). Following this the workflow was also designed to cope with intermittent sensor data that should not inhibit the running of the workflow i.e. heat flux was calculated even when the NO_x analyser was experiencing a fault.

Dynamic flux aggregation period length was added, meaning that input data could be provided at any record length and if the flux aggregation spanned across multiple files or alternatively many flux aggregation periods were contained within a file, this was handled at run time.

Double rotation of the coordinate system was implemented. This was not available in the base algorithm due to the major use case for the development team at NEON being long term monitoring and as such only planar fit methods were available.

Finally, an in-house package was developed to streamline the post-processing steps, including the running of the footprint model. All other steps marked as "eddy4R" in figure 2.6 are contained within the eddy4R workflow. This package handled the reading of the eddy4R output into a consistent format, such that transformations (i.e. combining NO and NO_2 and their associated errors into NO_x flux or extraction of inventory data using the results of the footprint model) were consistent. This was advantageous in the case where multiple sites are being used (as in chapter 4) or multiple iterations of the eddy covariance calculations need to be processed identically (as in section 3.1.3).

2.3.1 Quality Assurance and Quality Control

A notable feature available in eddy4R is the quality assurance and quality control (QA/QC) framework. This system builds a library of quality flags and metrics based upon tests both high-frequency (e.g 5 Hz) data, similar to those described by Vickers and Mahrt 1996 [79], or time integrated data (e.g 1 hour), such as stationarity flagging [86]. The framework builds upwards from individual flags for each data point and combines the broader criteria ultimately resulting in a single flag for a good or bad record. The flags can be tailored for a custom receptor like the NO_x instrument used in this work, so are sensor agnostic. A detailed description of the algorithms implementation can be found in the technical document by Metzger and Smith 2013, but an overview of the methods provided below [102]. The high frequency metrics are concerned with the plausibility of the signal:

- range - does a value fall outside of a sensible range or is nonphysical such as a negative concentration?
- step - was the change from the previous data point to the current realistic, or has there been a step change in the data?
- persistence - is the rate of increase or decay of the signal feasible, or is there a fault that has lead to this?

These are calculated either per data point or for persistence in a moving window across the high frequency data and the flag for that metric for that record is set as either pass or fail if a percentage threshold is reached (e.g 10 % out of range / missing data). Flags for each metric are combined into an overall quality flag through a weighted average, resulting in one signal high-frequency data quality flag for the record.

The time averaged criteria are concerned with the applicability of eddy covariance to the record:

- Stationarity - tests as described by Vickers and Mahrt 1997 (effect of detrending on the covariance) and Foken and Wichura 1996 (covariance of subintervals vs covariance of the whole record) are performed, and the result of the test where the data performs the worst informs the stationary flag [79, 86].
- Development of turbulence - measured turbulence is quantified as the integral turbulence characteristics (ITCs) (Tillman 1972 [103]) and modeled ITCs are calculated after Foken 2004 and Thomas and Foken 2002 [104, 105]. The magnitude of the percentage difference between measured and modelled ITC informs the quality flag

> (the test fails if the difference is greater than 100 %). It should be noted that the ITC criteria implemented in the QA/QC framework are based upon more idealised conditions than are commonly found in the urban environment. For the analyses presented here, the result of the QA/QC framework inclusive and exclusive of the ITC component did not differ significantly, especially when additional data cleaning metrics (such as the 150 % error threshold, section 2.2.2) are also applied, so the framework was run unmodified.

This process results in each time averaged period having three quality flags (from the combination of high frequency tests, stationarity and turbulence). A single flag for the time averaged period is the combination of these three flags such that if they all pass, the time averaged period passes and if they all fail the time averaged period fails.

2.4 Summary

The instruments described in section 2.1 can measure NO_x at suitably high time resolution for tower based eddy covariance experiments following the methodology described in section 2.2. Two were used to make NO_x emissions measurements in London and Delhi. One was deployed to a tall tower site in central London in 2017 (chapter 3) and was redeployed along with a second similar instrument to two sites in Delhi in 2018 (chapter 4). The aim of these experiments being to produce emissions estimates and assess inventories around the tower. A third similar instrument was deployed on an aircraft flown in the Thames Estuary to measure emissions from Greater London. In this case emissions estimates were calculated via a mass balance approach (chapter 5).

Chapter 3

NO_x Emission Measurement in Central London

Through a combination of the Automatic Rural and Urban Network (AURN) and the London Air Quality Network (LAQN) NO_x concentrations are measured across the Greater London area. Average annual concentrations for 99 sites in the Greater London area are shown in figure 3.1, 56 of which breach the European annual mean air quality limit of 40 μg m^{-3} in 2017 [57]. Sites classified as kerbside or roadside make up 51 of these (table 3.1).

NO and NO_2 are anthropogenic air pollutants, mainly emitted from combustion processes as NO and oxidised in the atmosphere forming NO_2. NO_2 is itself of concern for its impacts on human health, having been shown to exacerbate pre-existing respiratory and cardiovascular problems [44]. NO_x is also responsible for formation of ground level O_3 in the presence of peroxy radicals (from the oxidation of volatile organic compounds) and is involved in the formation of nitrate aerosols (see section 1.3). O_3 has been shown to cause pulmonary conditions, and has been linked to the development of asthma [45, 50].

Transport, domestic and industrial combustion are key sources of NO_x in the urban environment. Road transport is the largest single contributing sector with diesel engines receiving much of the attention and blame for the high concentrations seen in the London. Road transport has been the target of policy intervention in the city such as the Congestion Charging Zone (CCZ) introduced in 2003 which imposed a daily charge for vehicles driving into the centre of London, Monday to Friday, 7 am to 6 pm. This policy was not intended to improve air quality but rather, as its name suggests, congestion and also CO_2 emissions. Very little change was seen in NO_x concentrations and at places such as Marylebone Road, which forms the border of the CCZ, increases in ambient NO_2 were recorded [106, 107]. Grange et al. 2019 applied a machine learning technique designed to normalise the effects of meteorology on concentration data and showed that the CCZ increased effective concentrations of NO_2 at Marylebone Road and they did not approach pre-CCZ levels until 2011 with the improvement of buses from Euro III to Euro V on routes from around the site. Further decline is noted with the introduction of Euro VI and hybrid buses up to 2016, where the study ends. In April 2019 London introduced the Ultra-Low Emissions Zone (ULEZ) specifically targeting vehicle emissions. The charge applies at all times to vehicles that do not meet specific Euro classes for their vehicle type (motorbikes Euro 3, petrol cars Euro 4, diesel cars and larger vehicles Euro 6).

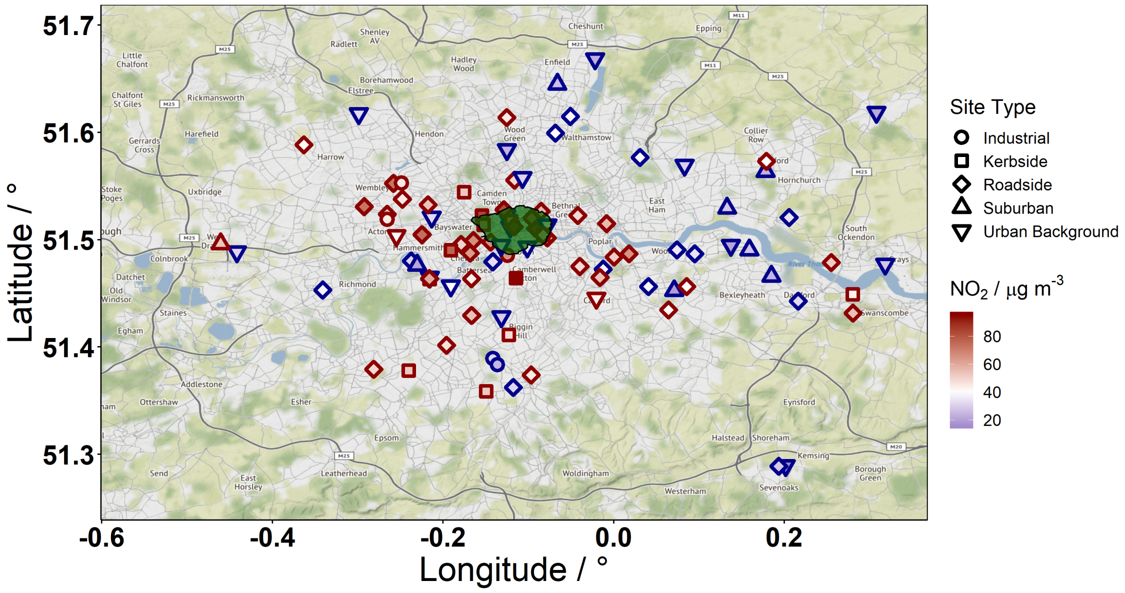

Figure 3.1: 100 air quality monitoring sites located in and around Greater London. Sites are coloured by their annual mean NO_2 concentration for 2017 (ug m^{-3}). Point shape denotes the type of measurement site. Point borders change from blue to red above the 40 ug m^{-3} air quality limit. 56 sites had annual mean concentrations above this limit in 2017. The area which encompasses the congestion charging zone and ultra low emissions zone is shown in green.

Whilst there are large amounts of ambient concentration measurements available, limited emissions measurements have been made in London. Emissions are estimated by the National Atmospheric Emissions Inventory (NAEI), and have been estimated to be declining, with total emission from the Greater London area decreasing from 124 to 45 ktonnes yr^{-1} between 1998 and 2017. However, NO_x concentrations have remained relatively stable over this period, with roadside concentrations even showing a slight increased in recent years (figure 3.2).

Eddy covariance (EC) measurements of NO and NO_2 fluxes were previously measured at the British Telecom (BT) Tower during the Clean Air for London (ClearfLo) project's intensive

Table 3.1: Sites in the Greater London area shown on figure 3.1 by type. Those that breached the annual mean are those that had an annual average of NO_2 greater than or equal to 40 μg m^{-3}.

Site Type	Breached Annual Mean	Total Sites	Percent
Industrial	3	5	60.00
Kerbside	12	12	100.00
Roadside	38	53	71.70
Suburban	1	8	12.50
Urban Background	2	21	9.52

operating periods in 2012-13 and from an aircraft during the Ozone Precursor Fluxes in an Urban Environment (OPFUE) campaign in 2014 [90, 91].

During ClearfLo Lee et al. 2015 collected EC data at the BT Tower for 36 days in June - August 2012 and 28 days in March - April 2013. These measurements suggested that there was consistent underestimation of the NO_x emission when compared to the NAEI by 1.36 - 2.2 times and was largest for fluxes measured to the east of the tower, across all footprint distances, towards central London. Diurnal profiles of NO_x correlated closely with diurnal profiles of traffic flow surrounding the tower.

Airborne EC NO_x fluxes were collected during 3 flights in July 2013. Vaughan et al. used these data to provide insight into the spatial change in emissions across Greater London and found the underestimation of NO_x emission by the NAEI, in central London, to be similar to that found by Lee et al. Moving out from central London, the agreement between measurement and inventory improved significantly. Both of these studies compared their results to the London Atmospheric Emissions Inventory (LAEI), an inventory that focus on the Greater London area, and an enhancement of the LAEI using using on road emissions data, collected via remote sensing. Both of these comparisons further improved agreement and suggested that the traffic sector is responsible for much of the disagreement. The spatial change in fleet makeup as you approach central London, away from private vehicles towards taxis and buses correlates with the increasing disagreement [108].

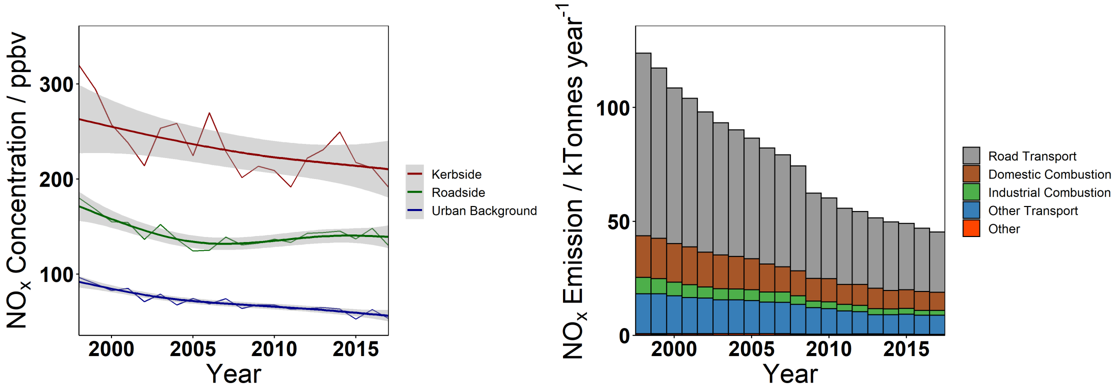

Figure 3.2: Left - Change in average concentration at roadside, kerbside and background sites in Greater London between 1998 and 2017. All sites with available data were first annually averaged, followed by the grand mean of all sites of a given type per year. A gam model was fit to the data to produce the smooth line, shading shows the standard error in this fit. B - National Atmospheric Emissions Inventory emissions for Greater London. These data were generated by scaling each sector of the spatially resolved inventory for 2017 by their respective sector total for the reported inventory time series, and subsequently summing all grid cells contained within the Greater London area. This was due to their only being a spatial inventory valid for the current inventory year (2017 in this case). Improvements in inventory construction are not back-propagated through the spatial inventories, but the time series inventory for UK totals is maintained.

3.1 Measurements at the BT Tower

3.1.1 BT Tower Site Description

Measurements were made at the BT Tower between March - June 2017 for NO, NO_2 and O_3 concentrations and NO_x fluxes. Instrument details are given in tables 3.2. The site is a 177 m tall tower located in Central London in borough of Camden, south of Euston Road and North East of Hyde park (lat/lon: 51.521/-0.139 °, figure 3.3). The surroundings are typical of the Central London area with a mixture of larger arterial roads high traffic density and smaller side streets interconnecting them. Traffic is slow moving and *stop-start* driving conditions are common during busier periods. Surrounding buildings within 3 km average ~50 m high, with the next tallest building measuring ~130 m, placing the sampling height above the canopy [109].

A 3-D sonic anemometer (Gill R3-50) was mounted on a mast atop the tower, co-located with the gas analyser sample line, providing a measurement height of 191 m. The anemometer was offset 11.9 ° clockwise from north. Air was pumped down the ~45 m sample line (PFA OD 3/8”) at $25\ \ell\ \text{min}^{-1}$, to the instrument which was located in a 19” rack on the 35th floor. The setup of this instrument is detailed in chapter 2, section 2.1. During March - June 2017 the predominant wind direction was between west and south westerly, with wind speeds up to ~20 m s^{-1}.

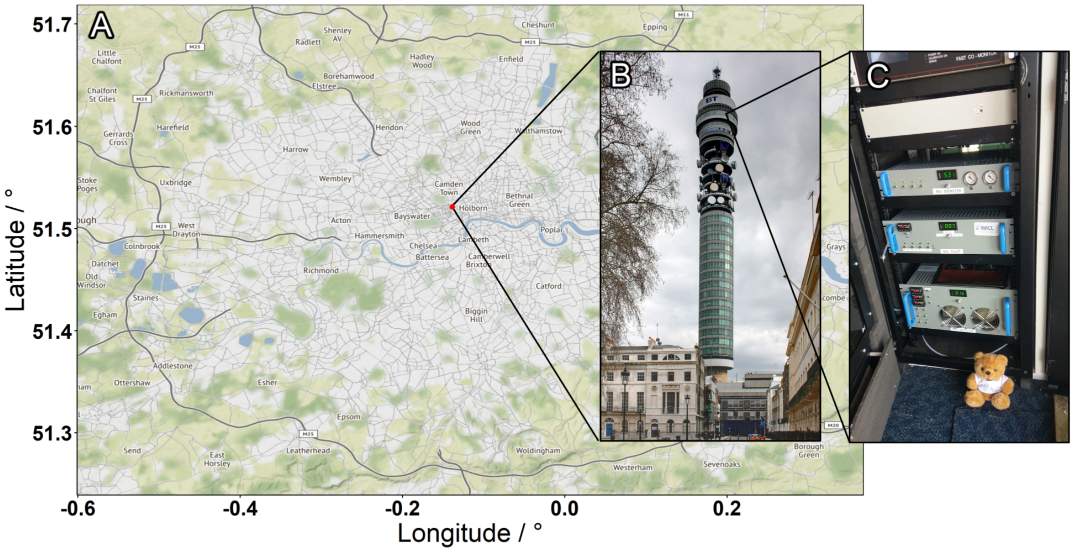

Figure 3.3: A - The BT Tower’s location in central London (red). B - The BT Tower. C - The NO_x instrument while located at the BT Tower

Table 3.2: Instruments installed at the BT Tower used for concentration and flux measurement during March - June 2017. Limit of detection quoted at the listed time resolution. * - Calculated as the the median of the standard deviation in the hourly zeros of the instrument during campaign, using the average channel sensitivities (2.4 and 3.8 counts pptv^{-1}). ** - Temperature calculated from speed of sound.

Quantity	Instrument	Time Resolution / Hz	Limit of Detection	Precision
NO / ppbv	Air Quality Design	5	153 pptv*	3 %
NO_2 / ppbv	Air Quality Design	5	199 pptv*	4.7 %
u, v, w / m s^{-1}	Gill R3-50	20, resampled to 5	0.01 m s^{-1}	-
Temperature** / K	Gill R3-50	20, resampled to 5	0.01 m s^{-1}	-

3.1.2 Instrument Calibration

NO and NO_x channel sensitivities and NO_2 conversion efficiency were calibrated automatically, following the procedure described in section 2.1.2, every 63 hours such that data loss from calibrations was spread over the diurnal cycle. A 5.2 ppmv NO cylinder (BOC 247536), traceable to the National Physical Laboratory (NPL) scale was flowed at ~ 10 sccm into the sample flow. Coefficients were linearly interpolated to 1 minute resolution before being applied to the data. Both channels were zeroed for two minutes hourly using the pre-chamber zero and an external Sofnofil and activated charcoal trap. Calibrations were used when inspection showed clear square responses and no large step change in calibration coefficients was caused. When a step change occured the following calibration was checked and in all cases the coefficients returned to within normal ranges when another calibration was performed so the anomalous calibration was discarded. NO and NO_x channel sensitivities were 2.4 ± 0.3 and 3.8 ± 0.6 / counts pptv^{-1} respectively and conversion efficiency was 70 ± 3 % over the measurement period. This variability is within normal ranges for the changes in external factors over the measurement period (e.g sample line flow, temperature).

3.1.3 Eddy Covariance Calculations

Data Pre-Processing

Before the EC calculations were performed, the raw data underwent pre-processing. Firstly, channel sensitivities and zeros were applied as equation 2.2. The conversion efficiency was applied after time lag correction in the eddy4R workflow so that lag can be corrected independently for NO and NO_x. Data during the zeroing of the instrument was removed along with any negative data points caused by instrument artefacts. Due to the alignment of the sonic anemometer wind vectors were offset from north by 11.9 ° counter-clockwise. This was corrected and wind vectors were adjusted such that the v wind vector was defined as positive towards the north and the u wind vector positive towards the east. Finally all units were converted to eddy4R's internal unit definitions; K for temperature, m s^{-1} for wind speeds and mol mol^{-1} for chemical species.

Eddy Covariance Settings

To explore the different permutations of EC options, sensitivity tests were conducted on data from 1st - 7th May 2017. Detrending, lag time correction, aggregation period length, and wind vector rotation settings were varied and have been summarised in table 3.3 along with the percentage change in data points that were flagged as high quality relative to the m.60.fix.d reference run (section 2.3.1). For fixed time lags, temperature was set to 0 s, NO to -6.4 s and NO_x to -6.6 s, and for windowed time lags NO and NO_x were allowed to drift between -10 and 0 s.

Figures 3.4 and 3.5 present the sensitivity tests as time series and diurnal profiles. Figure 3.6 depicts these data sets as scatter plots relative to the reference run. Combining these, the settings of 60 minute aggregation periods, windowed lag determination, double rotation and linear detrending were used for the calculations on the full data set.

From figure 3.4, 30 minute aggregation periods can be seen to introduce significant variability to the data, unseen in any other settings. Shorter averaging periods will also cause low frequency losses due to full eddy scales not being captured, especially with receptors located high up. For the BT Tower. An aggregation period of 120 minutes did not show an increase in the diurnally averaged flux (figure 3.5) and having the more frequent hourly measurements allows a greater time resolution footprint analysis.

Using windowed lag correction allows for small drifts in lag time due to physical processes, such as flow rate in the sample line or instrument pressure fluctuations to be corrected. Whereas a fixed lag time would result in a reduction in covariance during these times where drift is correct. This can be observed in the diurnal profiles where m.60.wind.d is either the same as or greater than the reference data (figure 3.5). Unrestricted lag (which in reality is a windowed lag determination with a much wider window of $\pm$ 40 s) differs from the fixed or windowed runs noticeably in the sensible heat flux diurnal where a negative data point at 8 am is not found (figure 3.5). Although negative sensible heat flux at this time is unexpected; from a physical perspective temperature and vertical wind speed have no lag as they are both measured by the sonic anemometer. In a detailed analysis of the sensible heat flux, the data points driving this spike should be examined in more detail, but in this case they highlight that using the unrestricted lag may mean similar data points are missed and as such will not be used.

Single rotation is not used as it leads to a lower flux than double rotation, illustrated in the diurnal profiles (figure 3.5, m.60.fix.s) and the more shallow gradient of the linear regression of m.60.fix.s versus reference panel on figure 3.6. Additionally, applying planar fit coefficients determined over the whole measurement period lead to lower fluxes than single rotation. Planar fit coefficients based on wind direction were also determined using the whole measurement period but in a 30 ° moving window, i.e a wind direction of 90 ° uses data from 75 - 105 °. These coefficients were produced at a 1 ° resolution. This method produced greater flux than single rotation, but still less than double rotation. A third method would have been to determine these coefficients using a moving time window. This is often used when the terrain around a sampling location is expected to change (i.e. growing vegetation). As the terrain does not change in this way in urban centres, this method was not applied. Ultimately, the choice of planar fit method introduced a level of ambiguity in the EC method and as such informed the decision to use double rotation and acknowledge the potential for some uncertainty due to over rotation [83].

Finally, linear detrending was used, as although some flux is lost compared to mean removal, NO and NO_2 can experience rapid changes in concentration on time scales similar to the flux aggregation period, especially during the morning and evenings. Using mean removal here would cause more violations in stationarity criteria during these periods, limiting the periods in which flux could be calculated.

Table 3.3: Eddy covariance calculation settings and their summary in run labels. Also shown is the difference in percentage of data points that passed the QA/QC test, relative to the reference run (m.60.fix.d).

Run ID	Detrending	Aggregation Period / minutes	Lag Time	Rotation Method	Passes QA/QC / % H	 NO_x
m.60.fix.d	mean	60	fixed	double	-	-
l.60.fix.d	linear	60	fixed	double	-0.3	0.3
m.30.fix.d	mean	30	fixed	double	2.8	0.4
m.120.fix.d	mean	120	fixed	double	1.5	-1.5
m.60.un.d	mean	60	unrestricted	double	-0.3	0.0
m.60.win.d	mean	60	window	double	0.0	0.0
m.60.fix.s	mean	60	fixed	single	0.6	-2.7
m.60.fix.PFwind	mean	60	fixed	planar fit - wind sector	1.5	-2.4
m.60.fix.PFf	mean	60	fixed	planar fit - full range	-0.3	-3.9

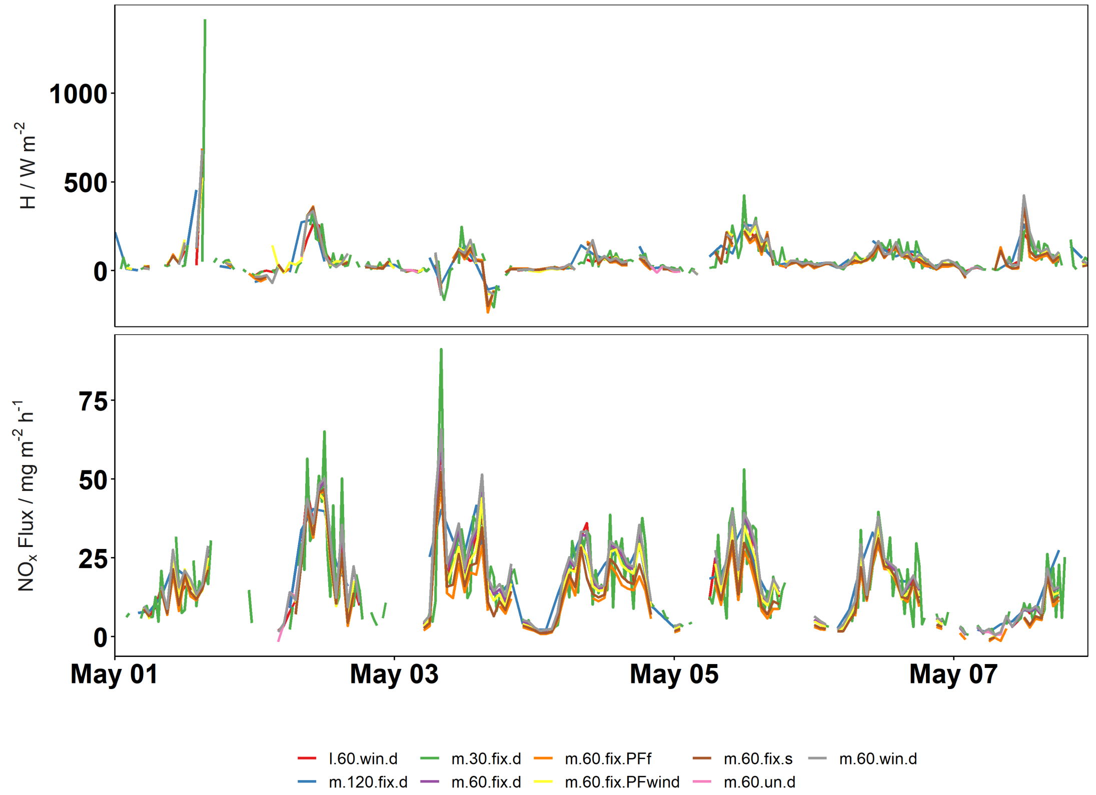

Figure 3.4: Time series of sensible heat flux (top) and NO_x flux (bottom) for 2017-05-01 - 2017-05-07, coloured by eddy covariance settings. Setting abbreviations are described in table 3.3

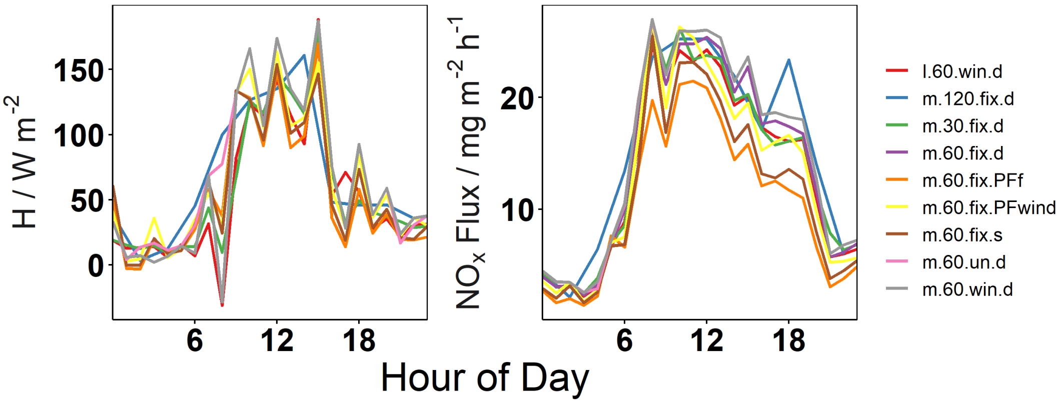

Figure 3.5: Diurnal profile of sensible heat flux (left) and NO_x flux (right) for 2017-05-01 - 2017-05-07, coloured by eddy covariance settings. Setting abbreviations are described in table 3.3

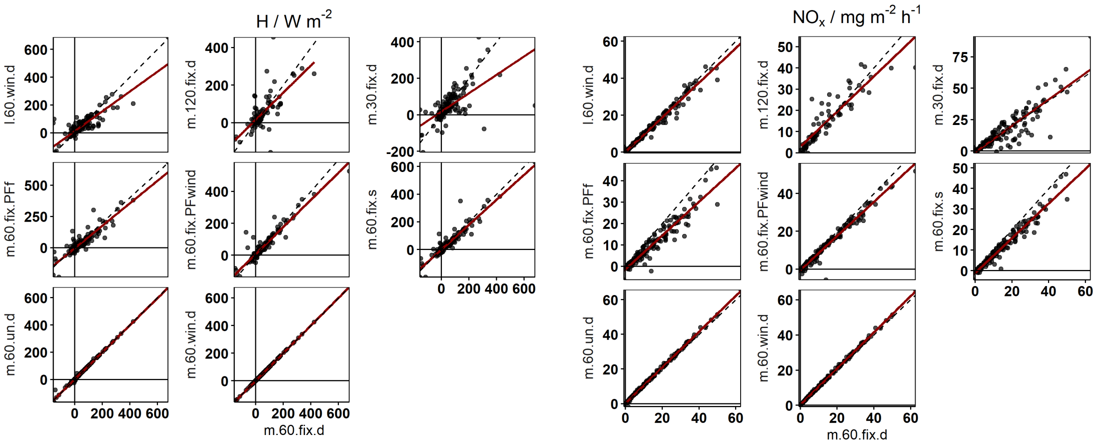

Figure 3.6: Eddy covariance calculations with varying setting of sensible heat flux (left) and NO_x (right), plotted against a reference run. Dashed line shows x=y. Setting abbreviations are described in table 3.3

3.1.4 Results

NO and NO_2 fluxes were obtained for 2008 hours between 2017-03-09 and 2017-06-15, where large data gaps are primarily due to instrument failure. Of these, 1668 were deemed to be of high quality based upon QA/QC criteria (section 2.3.1) resulting in 70 % data coverage for the period (figure 3.7). The following presents NO_x flux rather than NO and NO_2 separately, as the rapid interconversion between the two species causes the ratio at the sampling height to be different to that at the surface, but total NO_x is mostly conserved as chemical loss was estimated to be low. The primary loss route for NO_x is the conversion of NO_2 to HNO_3. Using equation 3.1, the fraction of remaining NO_2 after a given time can be calculated. For this calculation the median Deardorf velocity was used as an estimate for the rate of vertical transport up to the receptor height, providing a median transport time of 150 s [110]. The median temperature of 282 K was also used. From this it is estimated that 98.5 % of NO_2 reaches the receptor height, so loss to HNO_3 is negligible.

$$\frac{[NO_2]}{[NO_2]_0} = e^{-k_{[OH]} \cdot (\frac{T}{300})^{-4.5} \cdot [M] \cdot [OH] \cdot t} \tag{3.1}$$

where:

— $k_{[OH]}$ is the rate constant of NO_2 + OH + M, 3.2 $\times 10^{-30}$ cm^3 $molec^{-1}$ s^{-1} [111]

— T is the temperature, K

— [M] is the total number of molecules, 2.4 $\times 10^{19}$ molec cm^{-3}

— [OH] is the OH concentration, 1 $\times 10^{6}$ molec cm^{-3} (value representative of order of magnitude in absence of measurement [112])

- t is time, s

The diurnal profiles of NO_x concentration and flux are summarised in figure 3.8 alongside temperature and modeled boundary layer height from ERA5 (0.25 x 0.25 ° global meteorology product; ECMWF ReAnalysis 5, [113]). NO concentrations had an average peak of 14 ppbv at 0800 and decline steadily until 1800, where they remain below 3 ppbv overnight. NO_2 concentrations had two peaks of ~20 ppbv at 0800 and 2000. This second peak is not observed in NO as there is more photochemical activity than in the morning, rapidly oxidising the NO to NO_2 , along with further emission of NO having less effect on concentrations due to increased boundary layer height. The increased boundary layer height has the effect of diluting the emissions as the volume of atmospheric boundary layer (the lowest portion of the troposphere), is greater leading to lower concentrations for the same emission. For the flux, the average diurnal profile showed a steep rise in emission from (4.5 ± 0.3) to (20 ± 1.6) mg m^{-2} h^{-1} between 0400 and 0800, and remaining so until 1900 at which point it more gently declined to (4.5 ± 0.3) mg m^{-2} h^{-1} overnight by 0100. Without the additional information provided by the eddy covariance emissions estimates, the reason for enhanced NO_x concentration may be incorrectly attributed to increased emission during rush hour. For the morning peak, increased concentration did correspond to increasing emission, however, the decrease in concentration during the day occurred while emission remained relatively constant. This decrease was anti-correlated with increasing boundary layer height, meaning dilution effects were responsible. The evening concentration peak occurs while emission was decreasing, but at the same time boundary layer height was decreasing more rapidly, reversing the earlier dilution, leading to increased concentrations.

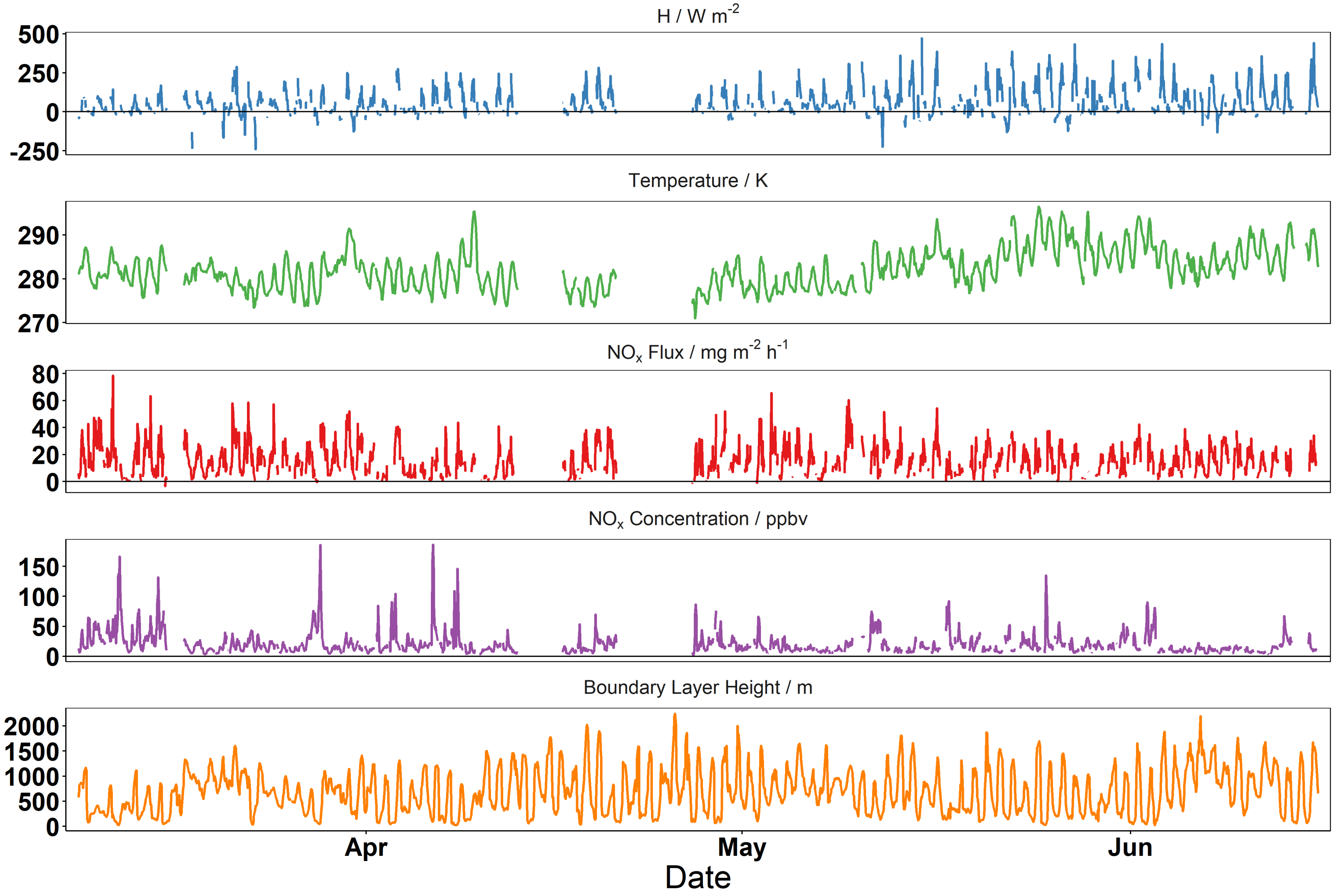

Figure 3.7: Time series of (top-bottom) sensible heat flux (W m^{-2}), temperature (K), NO_x flux (mg m^{-2} h^{-1}), NO_x concentration (ppbv) and modeled boundary layer height (m) at the BT Tower during 2017-03-09 - 2017-06-15

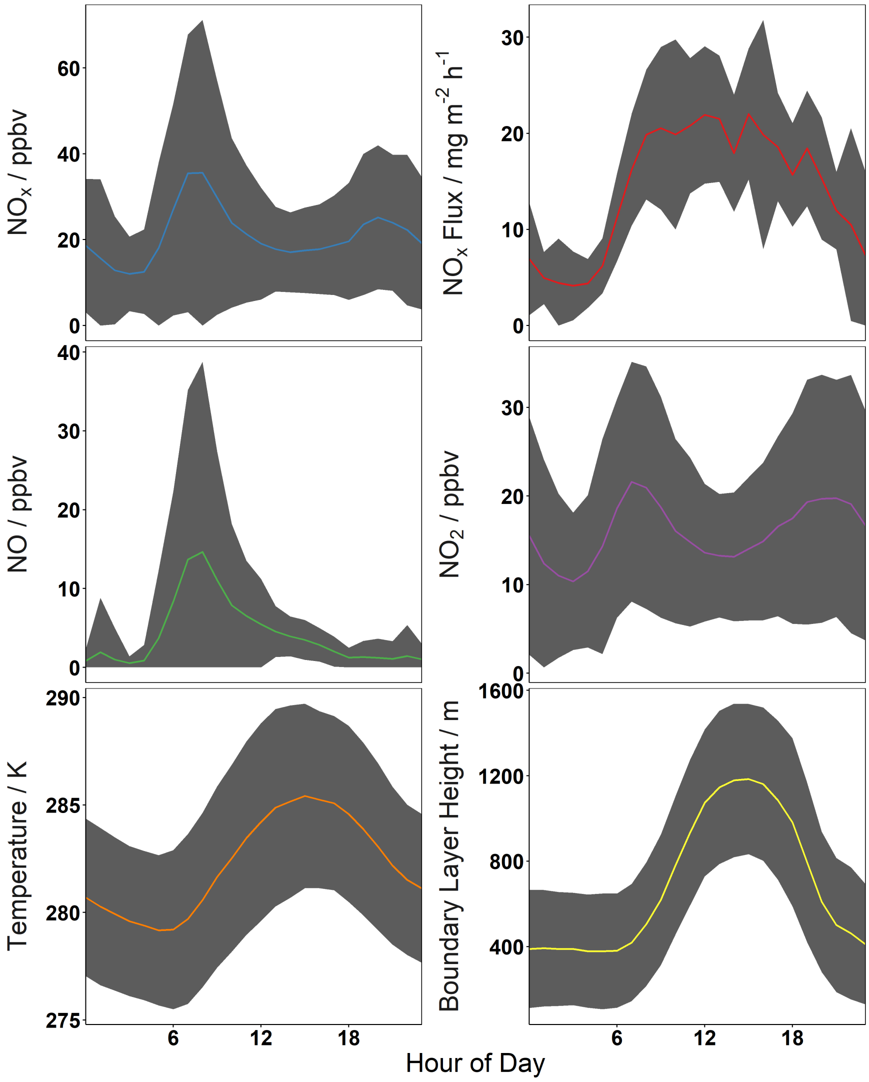

Figure 3.8: Top left - Bottom left; Diurnal profiles of NO_x concentration, NO_x Flux, NO and NO_2 concentrations (ppbv), and temperature (K) measured at the BT Tower between 2017-03-09 and 2017-06-15 inclusive. Bottom right; modeled boundary layer height (m) from ERA5 [113]. Shaded regions correspond to standard deviation in diurnal averaging for all panes other than NO_x Flux, where the shaded regions shows total average error.

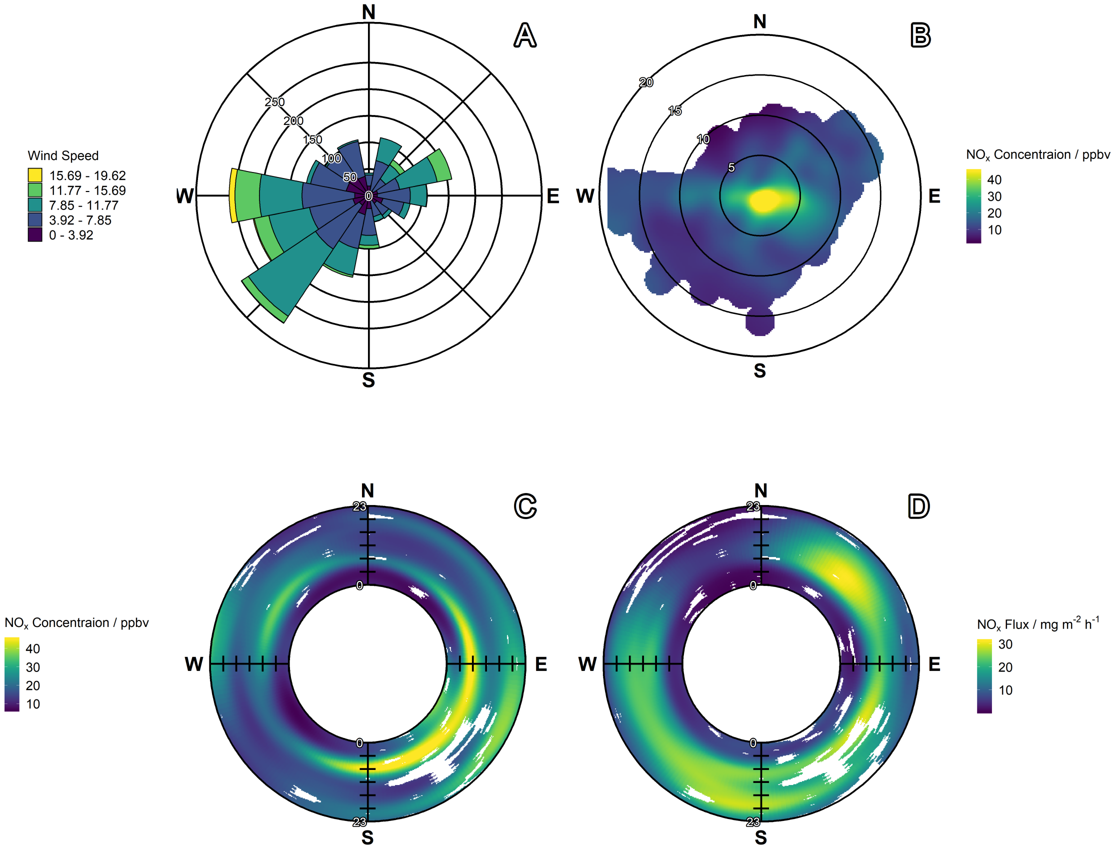

Figure 3.9: A - Wind rose for the BT Tower during March - June 2017. Radial distance shows counts of wind speed measured in a given direction. Paddles are coloured by wind speed bins. B - NO_x concentration as a function of wind speed on the radius, separated by wind direction. C - Polar annulus of NO_x concentration. 0 - 23 hours span the inner to outer circumferences, separated by wind direction. Colour on both B and C groups all concentrations of NO_x greater than 40 ppbv and higher together to preserve structure in the presence of single large values. D - Polar annulus of NO_x flux.

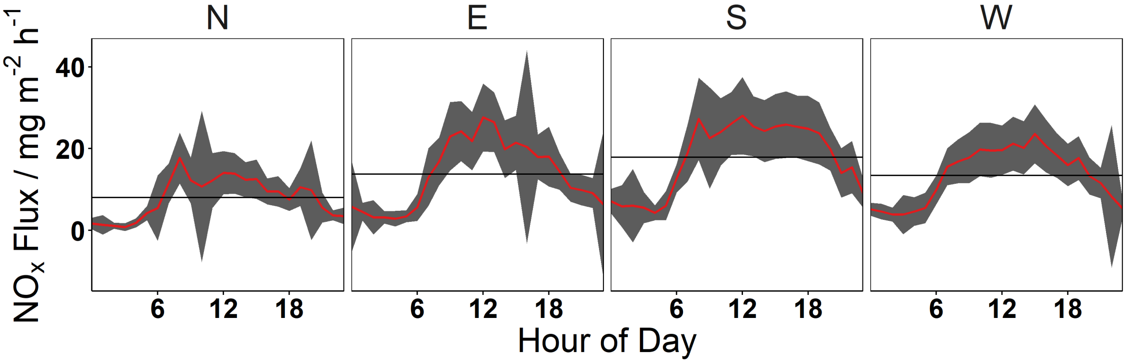

Figure 3.10: Diurnal profile of measured NO_x emission, binned by wind direction. Shaded region shows the total average error in the flux.

Measured emission of NO_x also differed from concentration when compared by wind direction. Directions which experienced lower average wind speeds saw the greatest enhancement in NO_x concentration. In figure 3.9-B the highest concentrations are seen when wind speed was lower than 5 m s^{-1} in all directions. In low wind speed conditions, concentration is more dependant on local emission, as transport to location is reduced. Or alternatively, local emissions stay near to their source, increasing local concentrations.

This leads to the enhancements observed in figure 3.9-C to the north west, east and south east. Here the average diurnal profile of NO_x is shown by wind direction. The diurnal profile is expressed from 0 - 23 hours, between the inner and outer circumferences of the annulus. These sectors correspond to the directions in lowest average wind speed and as such these directions saw the largest NO_x concentrations in their diurnal profile. Lowest concentrations occur when the wind is between 5 - 10 m s^{-1} from the north west. Close by in this direction is The Regent's Park, a large area of green space, which may contribute to the lower concentrations. This idea is supported by the flux annulus (figure 3.9-D) where enhancements occurred when the wind direction was from the north east through to the south west. Intuitively NO_x flux sampled from this region would be lower than other areas surrounding the tower, which contain more roads for traffic emission, and buildings which will contain combustion sources (heating).

The largest NO_x flux was shown the be from the north east, which was a direction where lower concentrations were observed due to the higher average wind speed, effectively masking this source. This direction is towards Marylebone Road and Euston station; areas of increased traffic density so enhanced emission is to be expected. However, using wind speed as a proxy for source is not reliable, as there is no true treatment of surface connectivity meaning that the along wind distance to the source is unknown. Emissions measurements combined with flux footprints give improved information about source location, as demonstrated in section 3.3.3.

Figure 3.10 shows the diurnal cycle based on wind sector. The highest day time NO_x flux was seen to the south, peaking at (30 ± 9) mg m^{-2} h^{-1}. A similar peak was seen to the east, however, the emission was less sustained after 1200 which causes the daily mean to be lower. The daily mean to the west was the same as to the east but in this case emissions had a peak of (24 ± 7.2) mg m^{-2} h^{-1} at 1500, with a more flat profile through the day. The lowest day time NO_x flux was seen to the north, with a morning peak at 0800 of (18 ± 6.2) mg m^{-2} h^{-1}. These differences in the shape of the diurnal profile suggest that the predominant emission sources (or the activity profiles that accompany them) likely differ with direction from the BT tower.

3.1.5 Uncertainties

Whilst the uncertainty in the flux calculation was quantified after Lenschow 1994, there are additional steps in the data processing which have uncertainties that are harder to estimate [114]. The following sections attempt to provide bounds for these uncertainties, so that they can be considered during when interpreting the results.

Removal of night-time data points

When flagging data for quality control, criteria such as stationarity are more readily violated when the magnitude of the calculated flux is lower. Stationarity criteria are considered violated if a subsection of the flux aggregation period calculated separately from the whole would deviate by a significant percentage (~30 %). It is more likely for a subsection to be a greater percentage different from the full aggregation period, the smaller the total flux for that period is.

In figure 3.11-A this is shown to be the case, with the percentage of records flagged by the quality control routine rising sharply once the magnitude of the flux fall below 10 mg m^{-2} h^{-1}. Furthermore, as NO_x emission followed a strong diurnal profile, the lower nighttime values are flagged more regularly, as seen in figure 3.11-B. Removing these flagged data, there is risk that the resulting values are biased high, especially so overnight.

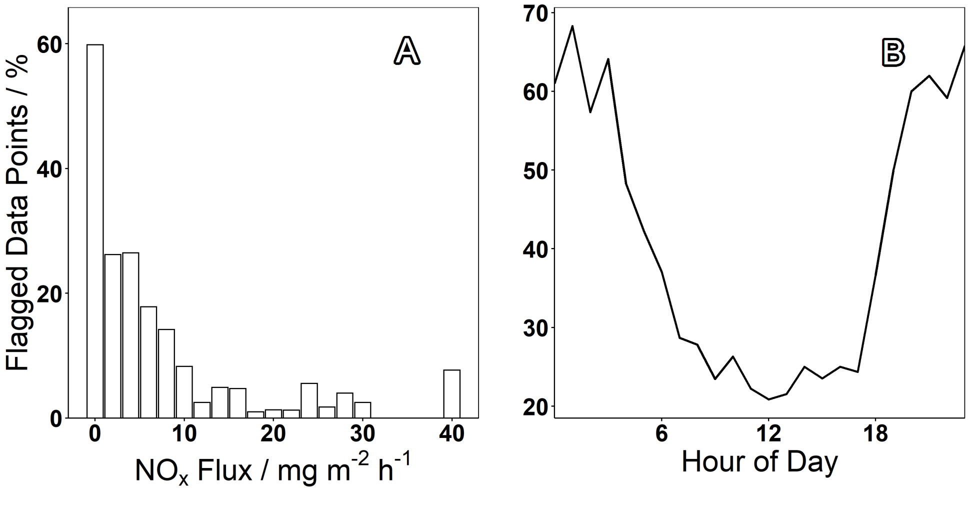

Figure 3.11: A - Percentage of flux records flagged by quality control routines in 2 mg m^{-2} h^{-1} bins. B - Percentage of flux records flagged by quality control routines by hour of day.

To quantify the effect of removing the values, the diurnal profile for NO_x flux was calculated twice in figure 3.12. The black trace removes all data that has been flagged by the quality control routines and the red has only removed points where the magnitude of the flux was greater than 5 mg m^{-2} h^{-1}. A slight high bias was observed when removing all flagged data points, and this bias was greatest at night up to ~20 %. For further analysis, all flagged data points have been removed, but nighttime data should be considered to have an uncertainty of up to 20 % greater than the averages presented.

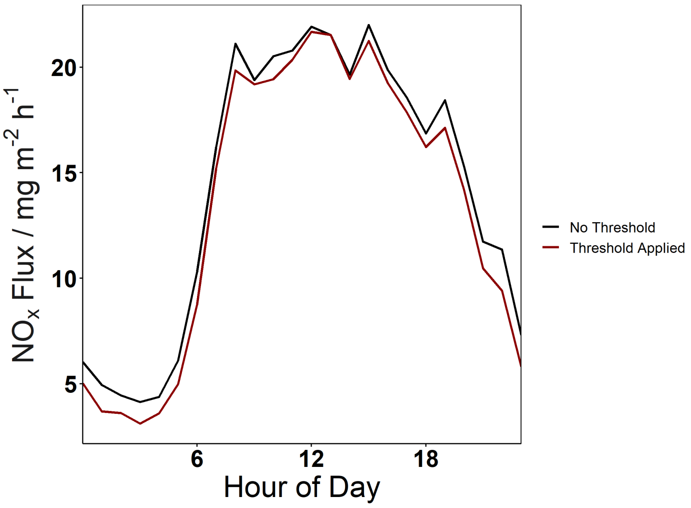

Figure 3.12: NO_x flux diurnal where black has had all records flagged by quality control routines removed and red has only had them removed if the flux magnitude was also greater than 5 mg m^{-2} h^{-1}

Reynolds Number Calculation

For an EC experiment using a closed path analyser, the sample line connecting the inlet to the instrument should have turbulent flow within it. Laminar flow in the sample line causes the gas which interacts with the tubing wall to flow slower than that in the centre, meaning that air parcels contain asynchronous samples, primarily causing high frequency losses [77, 115]. Reynolds number is a quantity which is used to define turbulent flow of a fluid. While the transition is not well defined, generally values of Reynolds number < 1000 would produce laminar flow, and those > 1000 would produce turbulent flow.

During the measurements at the BT Tower, flow rates in the sample line varied between 2.8 and 26.7 slpm due to the line's particle filter becoming blocked. The filter was only irregularly replaced as access to the inlet location was limited. Reynolds number was calculated as equation 3.2 and ranged between 120 and 2300. This leads to periods of time where the sample line was not under a fully turbulent regime, or was laminar.

$$Re = \frac{\rho v d}{\mu} \tag{3.2}$$

where:

- Re is the Reynolds number
- ρ is the density of air, calculated at the sample line pressure and temperature, kg m^{-3}

- v is the transit speed of the air down the sample line, m s^{-1}
- d is the internal diameter of the sample line, 0.00638 m
- μ is the absolute viscosity of air, calculated here as the Sutherland viscosity [116]; equation 3.3

$$\mu = \frac{bT^{\frac{3}{2}}}{T+S} \tag{3.3}$$

where:

- T is air temperature, K
- b is a constant, 1.458 $\times 10^{-6}$ kg m^{-1} s^{-1} $K^{-\frac{1}{2}}$
- S is a constant, 110.4 K

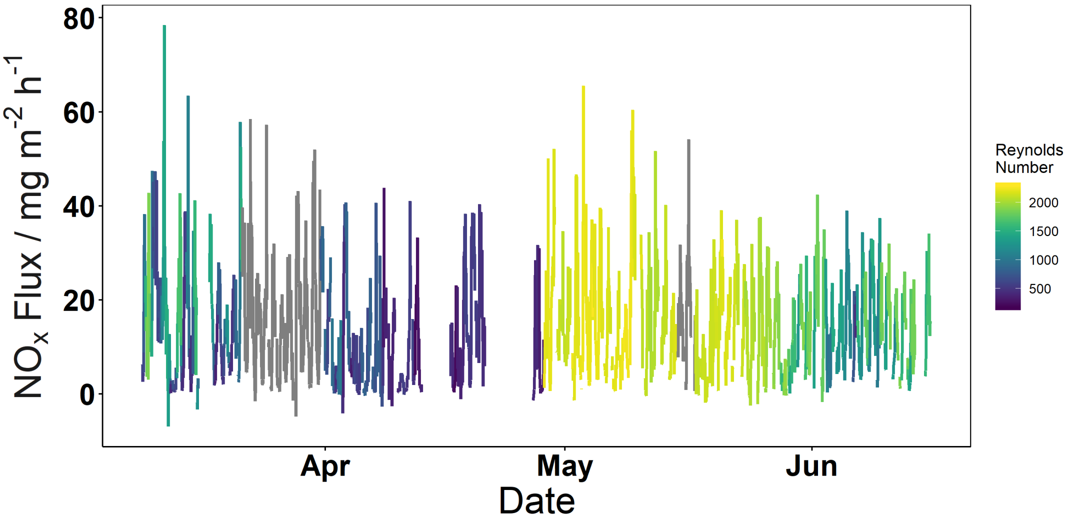

Figure 3.13: Unfiltered NO_x flux coloured by Reynolds number.

Due to its height the high frequency contribution to fluxes measured at the BT Tower is expected to be small, with Helfter et al 2012 noting that > 70 % of flux can be captured using an instrument running at 1 Hz. In figures 3.13 and 3.14 the relationship of Reynolds number with raw NO and NO_2 fluxes is presented. The fitting of the loess smoothed line on the binned data reveals that there may be a dependence of flux on Reynolds numbers below 1500. Further to this, NO_x flux was normalised between 0 and 1 and a second order polynomial was fit to the relationship below 1500 allowing the equation for an empirical correction factor to be derived 3.4.

$$CorrectionFactor = \left((-5.07 \times 10^{-7}) \cdot Re^2 + (1.61 \times 10^{-3}) \cdot Re - 2.83 \times 10^{-1}\right)^{-1} \tag{3.4}$$

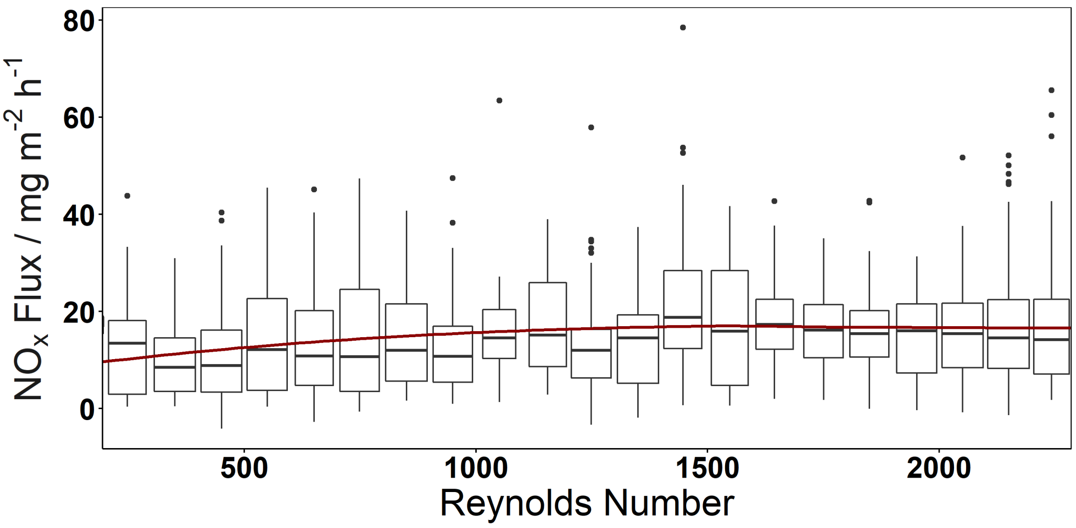

Figure 3.14: NO_x flux against binned Reynolds number (bin width 100). Boxes show median value as the horizontal bar and 25th and 75th percentile at the limits of the box. Whiskers extend to 1.5 × the inter quartile range, data that fall outside of this range are plotted as points. A loess smoothed fit shows increasing dependency of NO_x flux on Reynolds numbers below 1500

This method generated correction factors ranging from 1 - 96, however 95 % were less than or equal to 6. This subset of correction factors includes 70 % of the corrections available, but as this method will produce increasingly large numbers at lower Reynolds numbers, 6 was used as the threshold for this comparison. This threshold had the additional benefit of causing minimal change to the profile of the diurnal cycle; when correction factors above 6 were included *spikes* were introduced through uneven correction across the day. In figure 3.15 the corrected data is up to 50 % higher across the average diurnal. These values are not outside of the plausible range for NO_x flux in central London, with Vaughan et al. measuring up to 40 mg m^{-2} h^{-1} averaged over several flight legs. However, as this correction factor has been derived empirically and does not treat the underlying high frequency loss due to diminished turbulence in the sample line, it was not applied in further analysis and rather it should be borne in mind when considering the upper bound of the uncertainty in these measurements.

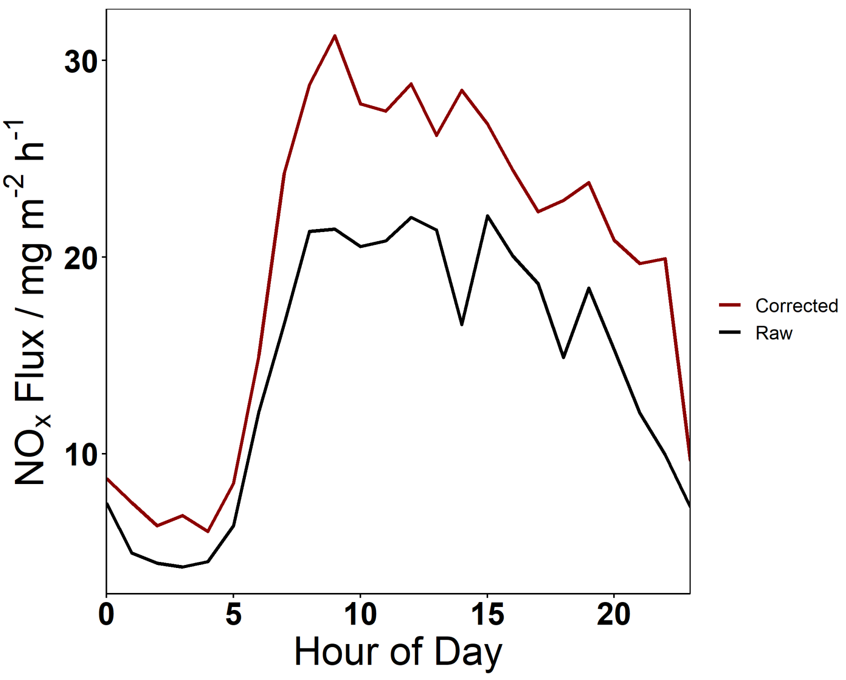

Figure 3.15: Diurnal profiles of NO_x flux showing the effect of the empirical correction factor derived for decreasing Reynolds number (equation 3.4)

3.2 Footprint Modelling

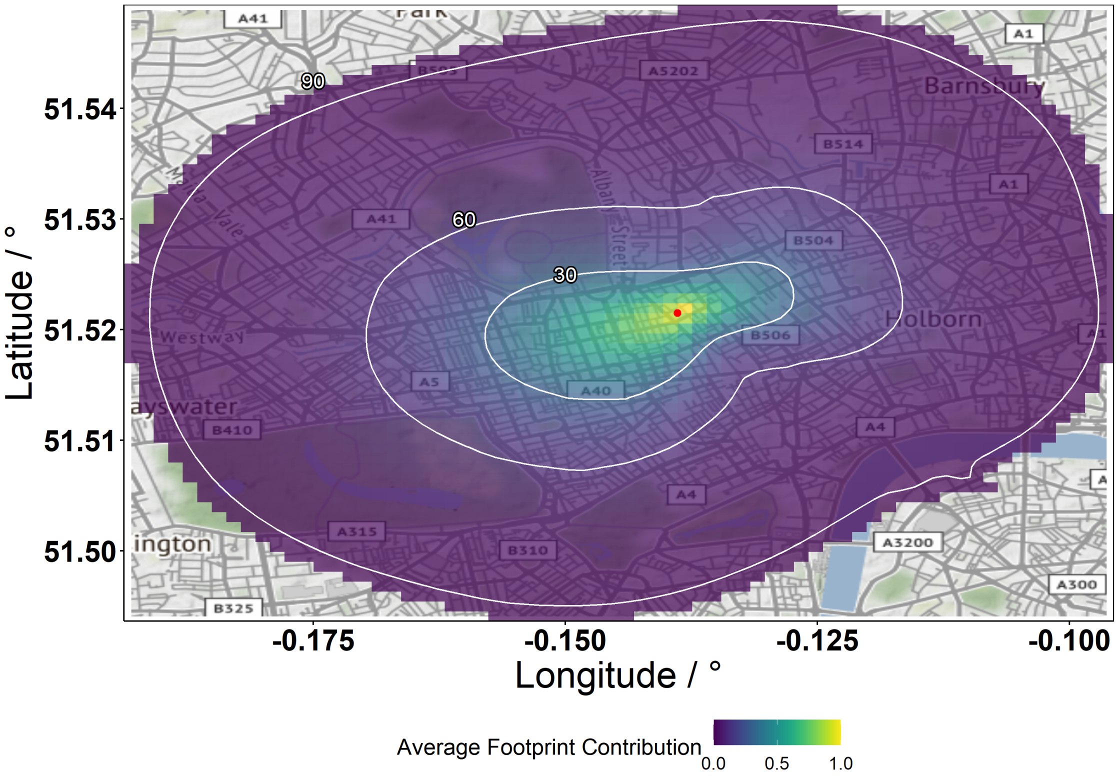

Figure 3.16: Flux footprint averaged over the sampling period. Colour represents normalised contribution to the measured flux. Contours mark the regions of 30, 60 and 90 % contribution to flux. Red point shows the location of the BT Tower

To link EC fluxes measured from a single point to the surface, a footprint model is required. For the measurements made at the BT Tower, a 2 dimensional footprint model was used which is based upon the parameterisation of backwards Lagrangian dispersion models by Kljun et al 2004 with an additional cross wind component by Metzger et al 2012. Full details of the footprint model are discussed in section 2.2.3. A footprint was produced at 100 x 100 m resolution per hour of flux data, using modeled boundary layer height and a roughness length of 1.1 m (the average roughness length within 5 km of the BT Tower, [117]). In figure 3.16 these footprints are averaged over the whole campaign. Sampled region reflects the conditions seen in the wind rose (figure 3.9-A), with the majority of flux sampled from the south west and north east.

The along-wind component of a given footprint resembles an asymmetric Gaussian distribution; in that it climbs more steeply to its peak than it decays afterwards with increasing along-wind distance. As such the distance to the along-wind maxima provides a simple reference point for the majority contribution to the sampled flux. This provides a straight forward, if not truly complete, method of constructing an emissions surface. Figure 3.17 was constructed through the same methods as figure 3.9-B where wind speed is replaced with along-wind maxima distance. This moves the data into a spatial domain which can be mapped. It is acknowledged that the simplifications used in this method mean that footprints that have a broader cross-wind component will have greater error in their location (in the cross-wind direction) as there is greater area covered by the flux footprint adjacent to the along-wind maxima. However, averaging over several months of measurements reduces this.

Figure 3.17 shows enhancements in the measured flux when the source area maxima is ca. 750 m to the north east of the tower. This area includes Euston, a national rail station where several services operate with diesel–electric multiple units. Additionally, there is a large bus stop outside the station, which connects to Euston road (A501). The London bus fleet in 2017 consisted of 70 % fully diesel vehicles with a further 28 % being hybrids. The remaining 2 % are fully electric and fuel cell buses [118]. Compounded with the traffic interruptions from the junctions around the station, the enhancement observed in this location is expected.

Additional areas of enhancement are observed around Oxford Street and the Marylebone area, which experience heavy traffic use and congestion. Lowest emissions are seen to the north where there is decreased road density. As noted previously this mapping method will have increased uncertainty with increased cross-wind contribution to the footprint. This is the case at lower wind speeds, wind direction is less well defined in these conditions. Wind speeds are most frequently the lowest from the north, therefore The Regent's Park may also contribute to the decreased NO_x emission here.

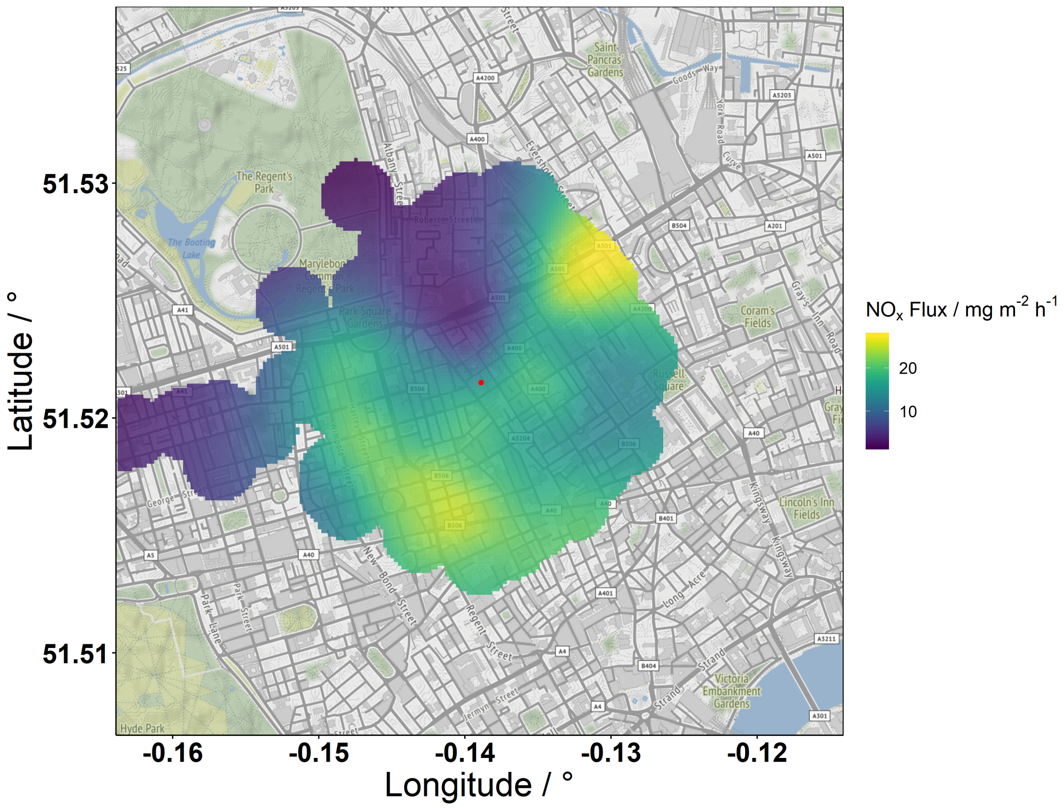

Figure 3.17: NO$_x$ flux surface as a function of along-wind distance to the maximum flux contribution on the radius and wind direction.

3.3 Inventory Analysis

3.3.1 The National Atmospheric Emissions Inventory

The NAEI is an annual emissions estimate for a variety of species in the UK from 1970 to present. Commissioned by the Department for Environment, Food and Rural Affairs (Defra), it is currently produced by Ricardo Energy & Environment; and used to report to European Union and United Nations green house gas and air pollutant monitoring programmes [29, 119]. Primarily the inventory provides total emissions estimates, required by these monitoring programmes. Calculations assimilate activity data and emissions factors from a wide range of sources and combines them to form an emission. Emissions are categorised into the 11 source sectors defined by the Selected Nomenclature for sources of Air Pollutants (SNAP) along with point sources, summarised in table 3.4 [120].

Once emissions estimates as a whole are compiled, the emissions are gridded using spatial information relevant to the SNAP sector. For example road transport uses road network location, local fleet composition from automatic licence plate recognition (ALPR) statistics and the annual average daily flow of traffic [121]. Combined with emissions factor and activity data this provides a 1 km^2 resolution map of emission in the UK.

Table 3.4: Selected Nomenclature for sources of Air Pollutants sector definitions as used in the National Atmospheric Emissions Inventory [29]. The four sectors with the largest contribution to NO_x emission within the footprint of the BT Tower are highlighted in bold

SNAP Sector	NAEI Label	Definition
01	energyprod	Combustion in Energy and Transformation
02	**domcom**	Combustion in Commercial, Institutional, Residential and Agriculture
03	**indcom**	Combustion in Industry
04	indproc	Production Processes
05	offshore	Extraction and Distribution of Fossil Fuels
06	solvents	Solvent Use
07	**roadtrans**	Road Transport
08	**othertrans**	Other Transport and Mobile Machinery
09	waste	Waste
10	agric	Agriculture, Forestry and Landuse Change
11	nature	Nature

Figure 3.18 shows the sum of the four SNAP sectors that make up the majority of NO_x emission in the greater London area in the 2017 version of the NAEI (sectors 07, 02, 03, and 08 in decreasing order of contribution). This grid provides annual NO_x emissions in tonnes yr^{-1}, so additional scaling is required to directly compare with measured NO_x flux. The scaling factors used are discussed in the following section (3.3.2).

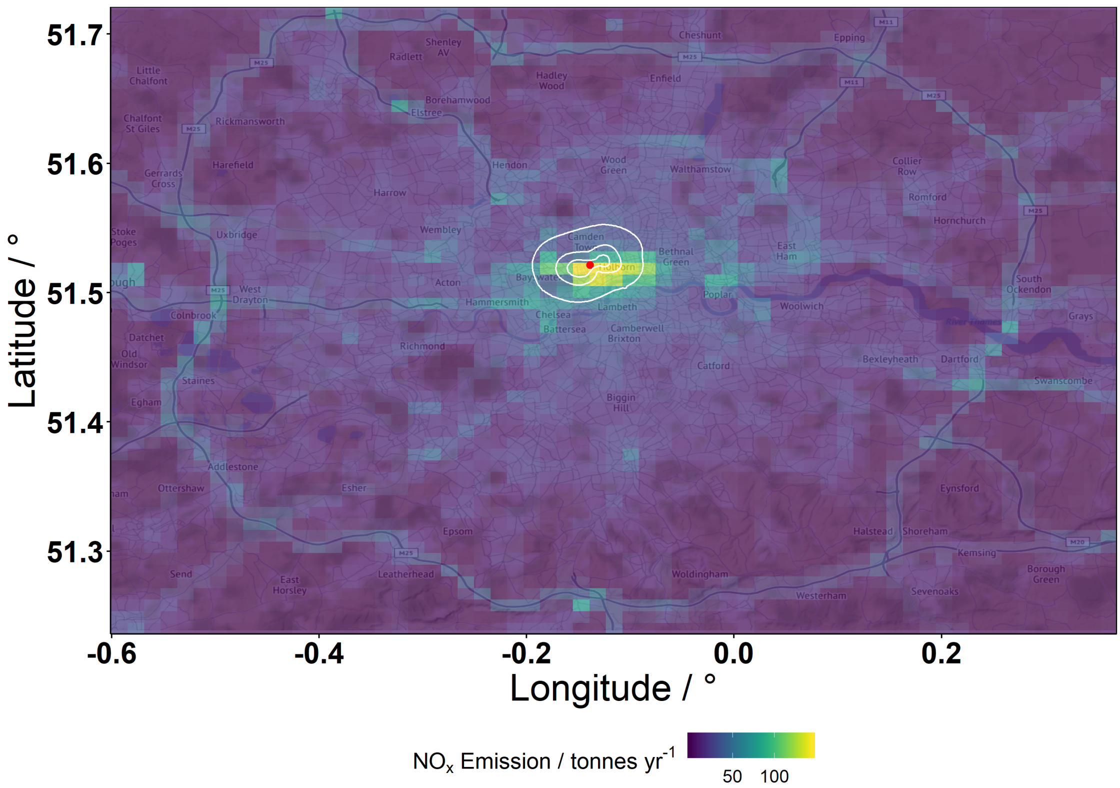

Figure 3.18: The sum of the NAEI layers corresponding to SNAP sectors 07, 02, 03, and 08 (table 3.4) to show the spatial distribution of the majority of NO$_x$ emission in central London. The 30, 60 and 90 % contributions to the average flux footprint for EC measurements made between March - July 2017 are shown in white (see figure 3.16 for averaged footprint data). The red point shows the location of the BT Tower

3.3.2 Scaling Factors

Scaling factors have been selected using the Temporal Emissions Profiles for SNAP Sectors report 2014. This report provide recommended scaling profiles for anthropogenic pollutants by hour of day, day of week and month of year. Figures 3.19 and 3.20 present the scaling profiles for road transport, domestic combustion, industrial combustion and other transport but those sectors that make up the *other* segment in figures presented in section 3.3.3 have been scaled by their respective factors before combining. The recommend factors are a combination of data from the van der Gon et al. 2011, Ricardo-AEA Technical Report and Defra's report on the Assessment of Benzo[a]pyrene Atmospheric concentrations in the UK [122–124]. Notably other transport is only scaled for month of year as hourly and daily activity data is highly spatially variable, for example non-road vehicles from construction.

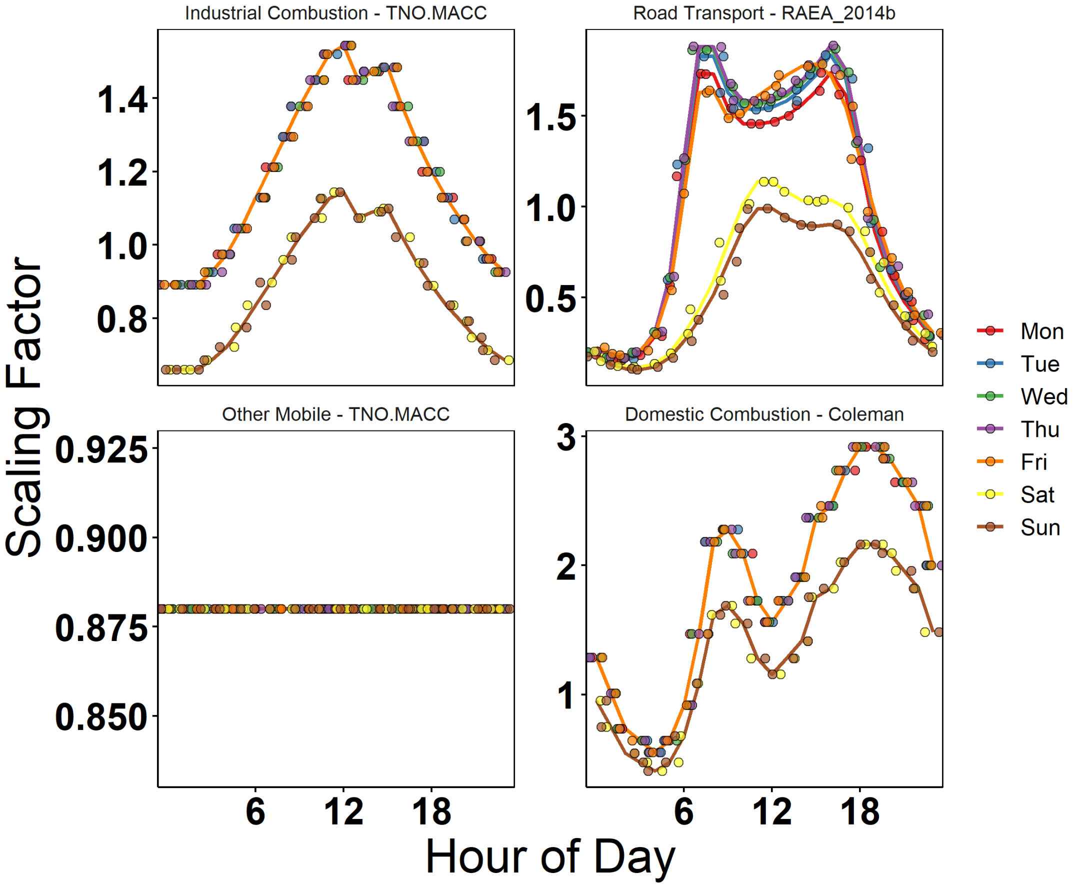

Figure 3.19: Hour of day scaling factors for the four SNAP sectors (07, 02, 03, and 08, see table 3.4) contributing to the majority of NO_x emission around the BT Tower, coloured by day of week. Points have been jittered in the x direction to show profiles that are identical

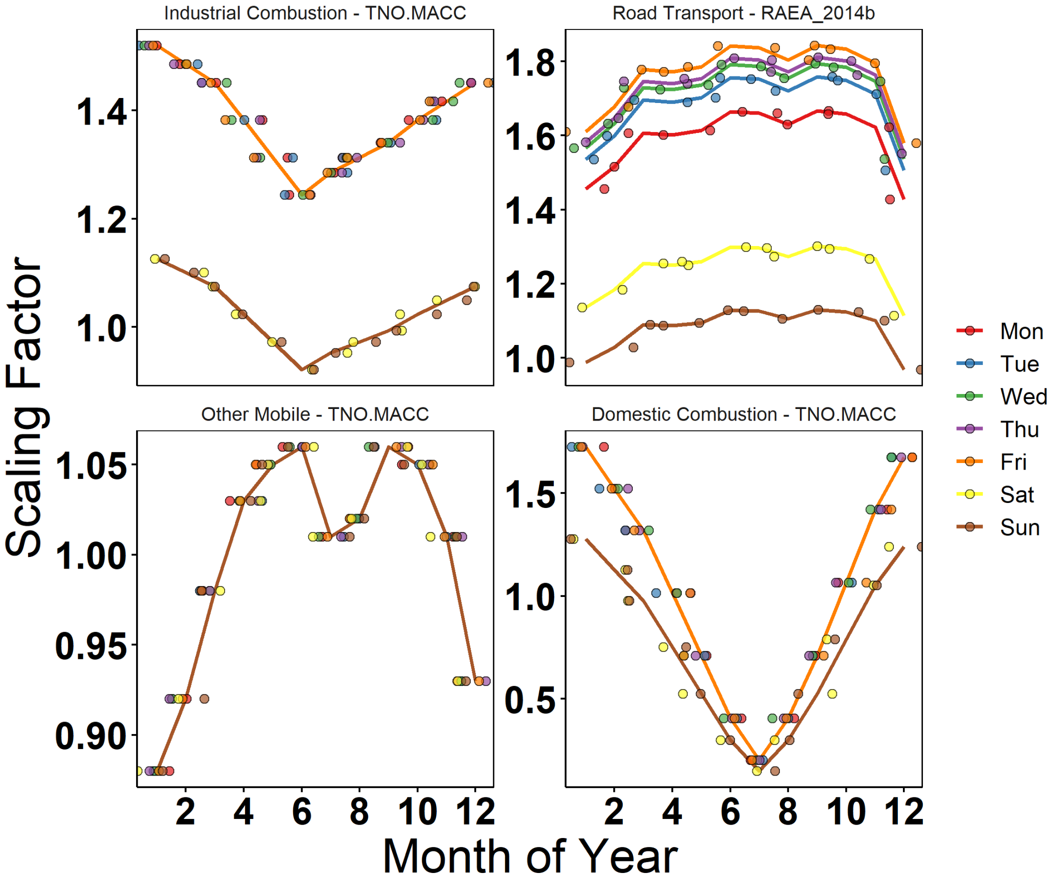

Figure 3.20: Month of year scaling factors for the four SNAP sectors (07, 02, 03, and 08, see table 3.4) contributing to the majority of NO_x emission around the BT Tower, coloured by day of week. Points have been jittered in the x direction to show profiles that are identical

3.3.3 Comparing Eddy Covariance and Inventories

By combining the footprint analysis (section 3.2) with the spatially resolved, temporally scaled NAEI (sections 3.3.1 and 3.3.2) a predicted emission per hourly flux measurement was generated. This was achieved by projecting the flux footprint into the coordinate system of the inventory, and extracting its value at the centre of each of the footprints grid boxes. Each inventory value was scaled to its theoretical contribution to the measured flux by multiplying these extracted data by the footprint weighting matrix, which was subsequently summed to give a single value for the inventory estimate. This approach was applied to each of the source sectors for the inventory. Point sources are not explicitly provided as an inventory layer, but were generated as the difference between the total emission and the sum of the 11 SNAP sectors (dubbed *reactive* in the NAEI data product), resulting in 12 categories. Each sector was scaled by the product of its corresponding hour of day, day of week and month of year scaling factor. Where one or all of these factors were unavailable, a value of 1 (no scaling) was used. For those sectors that are the majority contributors to NO_x near the BT Tower, no scaling factors were missing, though the hour of day and day of week scaling factors for other transport are reported as 1. See section 3.3.2 for more details. In the discussion that follows, these scaled inventory data from within the flux footprint are presented as the sum total of all sectors or as the 4 primary SNAP sectors (road transport, domestic combustion, industrial combustion and other transport) separate, with all other sectors combined as *other*.

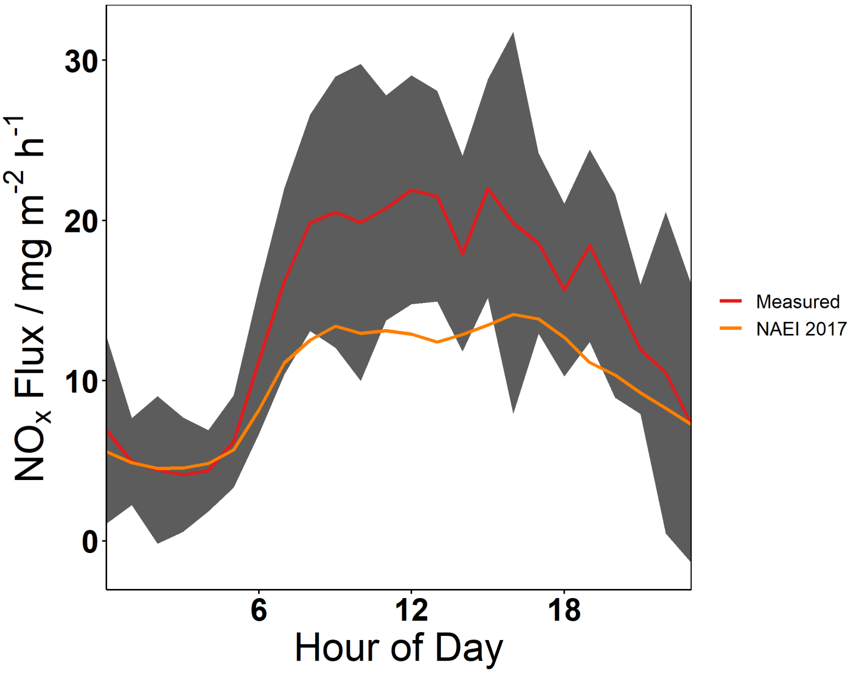

Figure 3.21: Average diurnal profiles of NO_x emissions measured (red) at the BT Tower March - July 2017 and the NAEI's estimated emission (orange) from within the flux footprint. Shaded region shows total (random + systematic) error in flux measurement.

The overall average diurnal profile (figure 3.21) showed good agreement overnight between 0000 until 0600 from which measurements were higher throughout the day. When the uncertainty surrounding the measured flux being biased high due to removal of data points during QA/QC (section 3.1.5) is considered, it is possible that the inventory overestimated emission during this time, though this would still fall within the total error in the flux measurements. The inventory underestimates the measured flux the greatest at 1300, where the inventory was 1.7 × lower than the measured flux. Agreement in magnitudes improved from 1800 onwards, where the measured flux decreases more rapidly to its nighttime value than the inventory. The inventory also showed a double peak during the day time, driven primarily by road transport and domestic combustion scaling factors. This structure was not present in the measurements, instead remaining relatively stable throughout the day.

Through comparison of the diurnal profiles by wind sector (figure 3.22) variation in the degree of underestimation is revealed. The maximum underestimation of 2.6 × was observed to the north during the peaks measured around 0700 and 1900. Only in this direction was a double peak structure observed in the measurements, but there was also limited sampling from this direction (figure 3.9-A), so these enhancements may simply be due to noise in the average. The greatest sustained underestimation (1.7 × ± 0.3) was observed to the south between 0800 and 1900. To the east there was agreement to within the flux error during the afternoon, but significant underestimation between 0800 and 1200. Figure 3.9-D highlighted an enhancement to the north east, which is more significant in the morning. The lack of this in the inventory suggests that this sources' activity has not been described sufficiently. There are two points sources attributed to University College London within the flux footprint to the east of the BT Tower, which combined are estimated to emit ~2.05 mg m^{-2} h^{-1}. They are contained within a 1 x 1 km grid cell which in total is estimated to emit ~13.7 mg m^{-2} h^{-1}. Point sources have not been scaled, as they would required their own specific activity information and as such it is possible that these point sources contribute to the shape of the eastward diurnal.

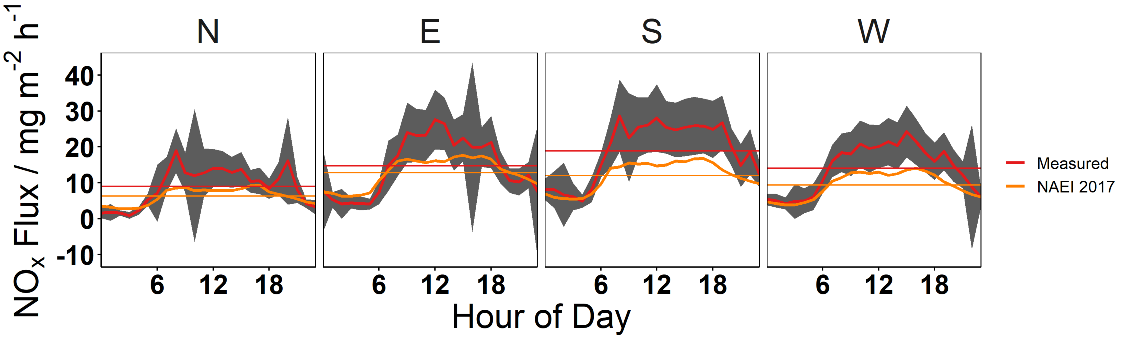

Figure 3.22: Average diurnal profiles of NO_x emissions measured (red) at the BT Tower March - July 2017 and the NAEI's estimated emission (orange) from within the flux footprint, separated by wind sector. Shaded region shows total (random + systematic) error in flux measurement. Horizontal lines show the daily mean emissions value for both measurements and inventory estimates.

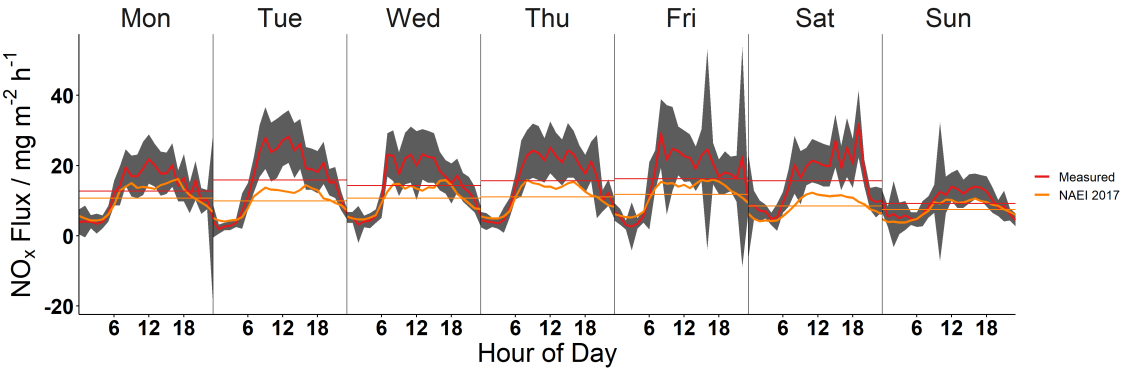

Figure 3.23: Average diurnal profiles of NO_x emissions measured (red) at the BT Tower March - July 2017 and the NAEI's estimated emission (orange) from within the flux footprint, separated by day of week. Shaded region shows total (random + systematic) error in flux measurement. Horizontal lines show the daily mean emissions value for both measurements and inventory estimates.

In a comparison between measurement and inventory by weekday (figure 3.23) the greatest underestimation (3.3 ×) is found at 2000 on Saturdays. During this time the measured flux was enhanced between 1700 and 2000 where on other days NO_x emission decreased. Scaling factors weighted Saturdays and Sundays lower (figures 3.19 and 3.20) but measurements suggest that days of the week are instead better grouped as Tuesday - Saturday as higher than Monday as higher than Sunday. The combined effect of these lead to significant difference between inventory and measurement at this time. Sunday saw the best agreement out of all days of the week, with both magnitude (to within flux error) and profile being well captured. Both Friday and Tuesday exhibit the same morning enhancement seen from the east in figures 3.22, but this could be due to uneven sampling of wind directions on these days. A longer time series would be required to explore this, as to break down these data into day of week and wind direction simultaneously would lead to 3 data points per hour (assuming even distribution across all groups). The increasing NO_x emission measured between 0600 and 1800 on Saturdays was likely activity driven, as this was not seen in the wind sector break down. To explore this further, figures 3.24 and 3.25 break down the inventory by sector.

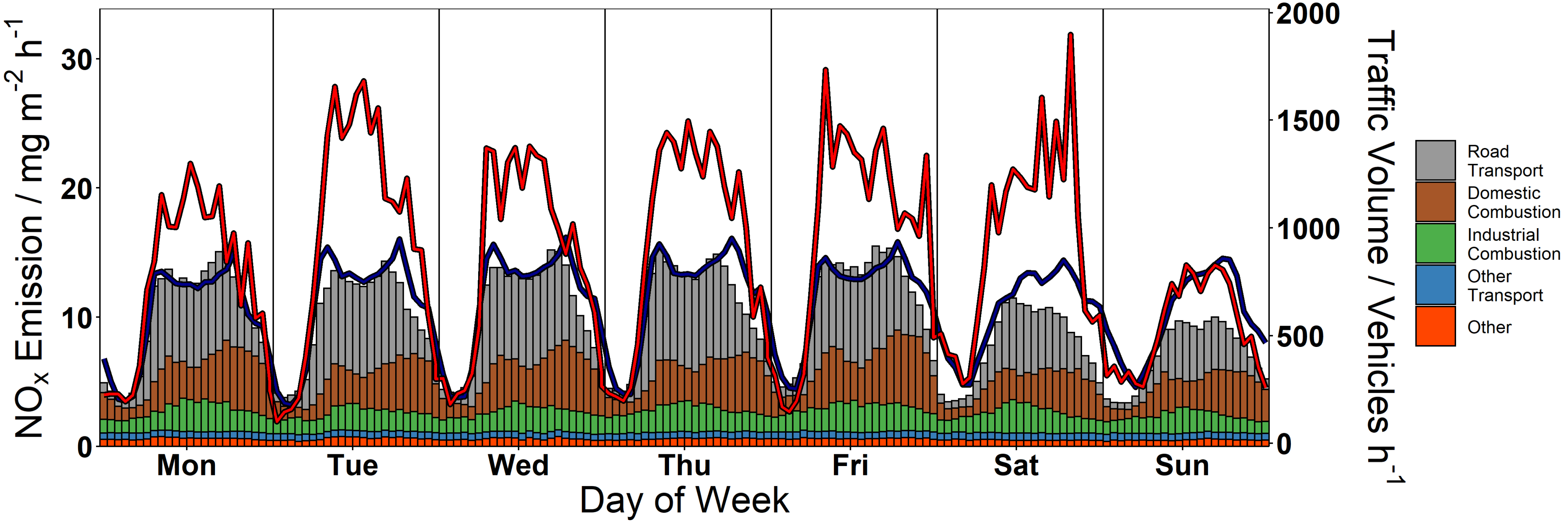

Figure 3.24: Average diurnal profiles of NO_x emissions measured (red) at the BT Tower March - July 2017 and the NAEI's estimated emission (bars) from within the flux footprint, separated by day of week. NAEI emissions are coloured by source sector contribution. Median traffic volume from 24 automatic traffic counters surrounding the site are shown in blue [125].

From this breakdown, road transport was shown to be the primary contributor to magnitude of the emissions estimate and the primary driver of the diurnal variability. This was followed by domestic combustion industrial combustion and finally other transport. Road transport and domestic combustion had a bimodal distribution peaking in the morning and evening Monday - Friday, with this feature being less apparent Saturday - Sunday. Together these drive the double peak seen in the overall inventory. This was however suppressed by industrial combustion peaking at midday. As disagreement between measurement and inventory was greatest during the day, the road transport sector or scaling factors likely encompasses much of this error and indeed overnight, where there is little contribution from road transport, the agreement was best. This nighttime agreement was best for Sunday - Thursday (or the early hours of Monday - Friday).

This has been further demonstrated on figure 3.24, where median traffic volume has been over-plotted. Traffic volume data was obtained from 24 automatic traffic counters (ATCs), operated by Transport for London (TfL), for each hour of flux data. The ATCs were selected as those which were weighed highest by the average footprint for whole measurement period (figure 3.16). A mean day of week diurnal profile for each of these ATCs was calculated, followed by the median day of week diurnal profile of all the sites.

The decrease in traffic volume was not as pronounced as the decrease in the road transport sector between weekday and weekend. Additionally on Saturday - Sunday reached their first peak later in the morning compared with Monday - Friday, increase between 0800 and 1800 and remain higher overnight which is consistent with the measured flux. The former of these was reflected in the road transport scaling factors for the weekend, but they then go on to decrease after the first peak (with a slight inflection around 1700) and return to the same nighttime levels as the weekday factors.

From figure 3.25 it can be seen that although the under prediction was ever-present during the day, on average it was not a constant spatially. To the north north east, in the direction of the enhancements seen in figure 3.17, near Euston station, there was a 2.8 × underestimation, and to the south west an underestimation by 1.5 ×. To the east south east the NAEI showed good agreement with measurement, split between slight underestimation during the day and slight overestimation overnight. In the north west, towards The Regent's Park, there was an overestimation of ~2 ×. By applying the footprint mapping approach introduced in figure 3.17 to the scaled inventory data the differences can be shown in the context of the area surrounding the tower. This was created from panels A and B of figure 3.26, with the difference map being shown in panel C. Those areas that have been highlighted by the measurements as significant sources, are not captured by the inventory in this treatment. This is partly due to the resolution of the NAEI. The BT Tower is located on the border between 4 grid cells (figure 3.18), with those to the north being distinctly lower than those to the south, as is clear from figure 3.22. Euston station falls on the cusp of the change in grid

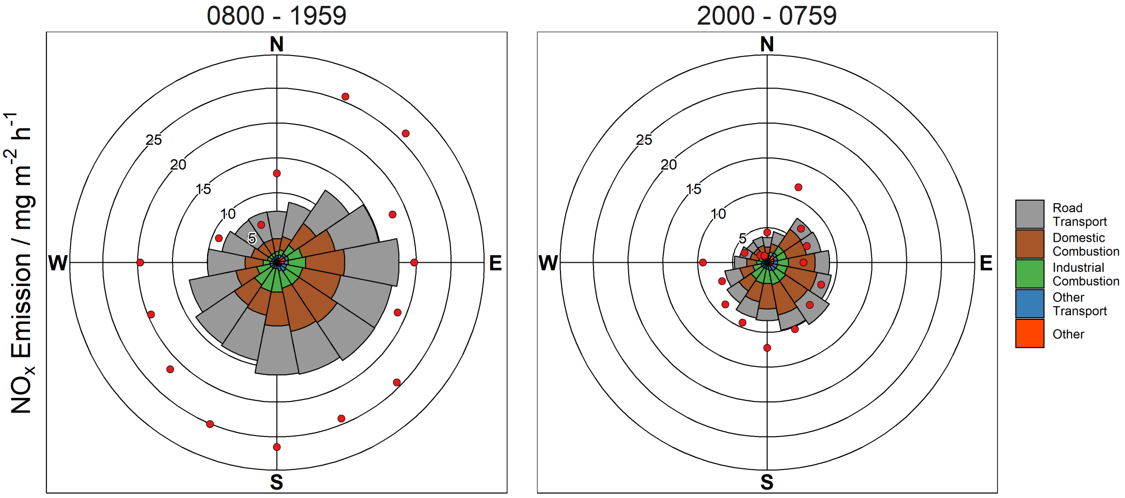

Figure 3.25: NO$_x$ emissions (red) measured at the BT Tower March - July 2017 and the NAEI's estimated emission (bars) from within the flux footprint, averaged by 22.5 ° wind sector bins. NAEI emissions are coloured by source sector contribution. The left hand panel shows all data between 0800 - 1959 and the right hand panel shows all data between 2000 - 0759.

cells, and may have lead to it not being completely resolved by this method. However, the enhancement in the south west was more pronounced. This may point to the proxies that are responsible for the south east's improved agreement may also apply to the south west. Greater exploration of the inventories construction would be required to test this, which is outside the scope of this work.

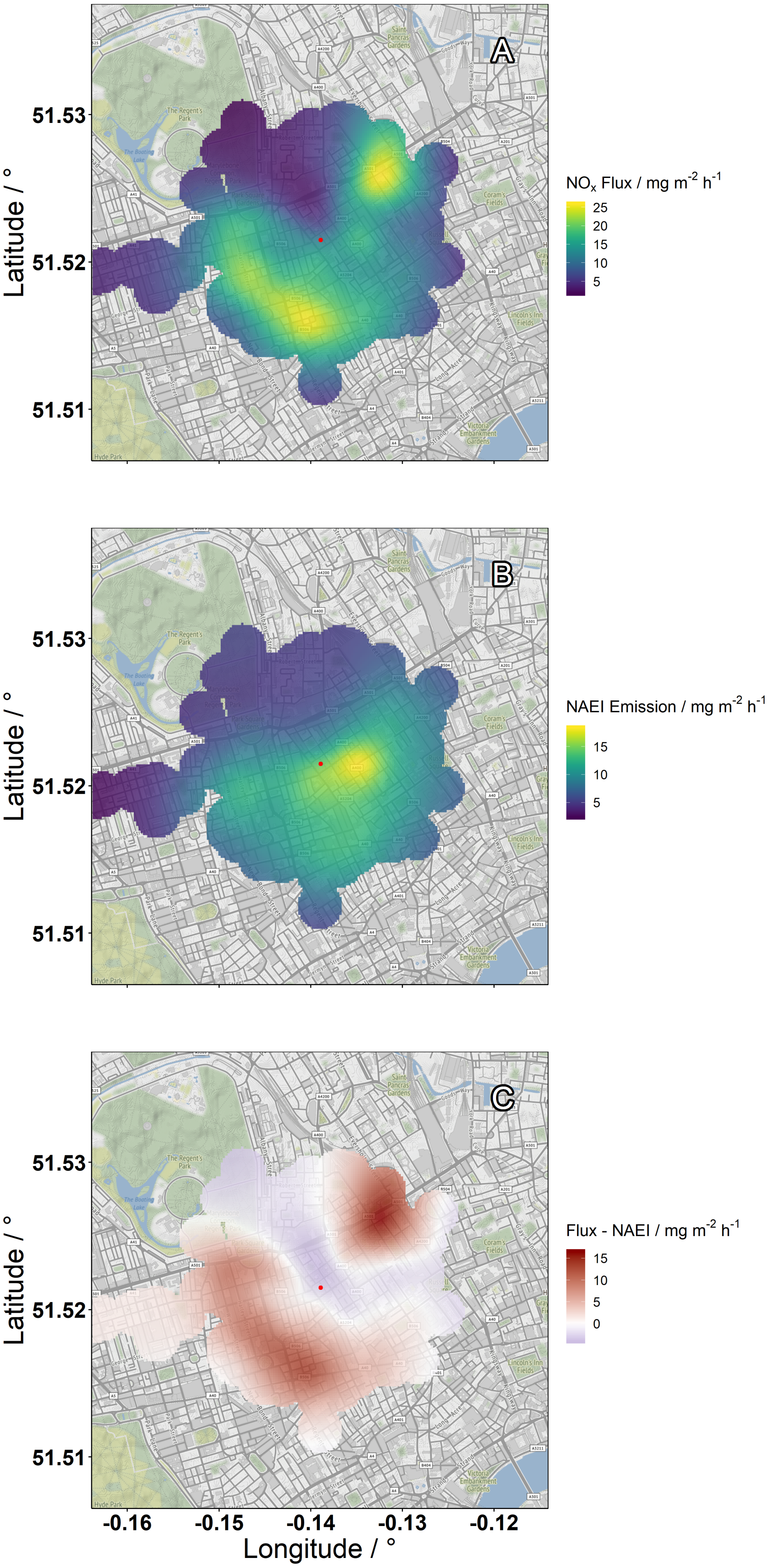

Figure 3.26: A - Measured NO$_x$ flux as a function of along-wind distance to the maximum flux contribution on the radius, separated by wind direction (figure 3.17). B - NAEI NO$_x$ emissions estimate as a function of along-wind distance to the maximum flux contribution on the radius, separated by wind direction. C - B subtracted from A, red shows measurement greater than inventory, blue shows inventory greater than measurement

3.4 Comparison with 2013 Measurements

The NO and NO_2 data collected by Lee et al in 2013 has been reprocessed using the same methods used throughout this chapter. Footprints were calculated and using the scaling factors from section 3.3.2 were used to generate an equivalent inventory estimate using the 2012 version of the NAEI. Figure 3.27-A compares the average diurnal profile of the 2013 and 2017 measurements and their respective inventory estimates. A stronger morning emission was observed in 2013 than in 2017, peaking at 30.8 mg m^{-2} h^{-1} at 1200. Based on the wind rose for the 2013 measurements (figure 3.27-B), east was the predominant wind direction. This peak may have been caused by the same source seen in the eastward 2017 measurements (figure 3.22) and due to the smaller data set for 2013 (315 records) was more prominent in the diurnal average. It should be noted that compared to the data published by Lee et al, this feature is more noticeable due to the lack of afternoon peak in the reprocessed data. Due to the small data set, these slight changes in diurnal profile can be attributed to how the QA/QC criteria differ between processing methods. Nevertheless, this morning peak is within the combined error of the measurements and during the rest of the diurnal profile there is reasonably good agreement, suggesting there was little reduction in NO_x emission between these times.

Similar underestimations were found when comparing NAEI for 2012 to the 2013 measurements and the NAEI for 2017 to the 2017 measurements (table 3.5). The underestimation of the daily mean emission by the inventories was 1.3 × for the 2013 measurements and 1.4 × for the 2017 measurements. The measured daily mean emission was shown to have reduced by ~9 % between 2013 and 2017, but this value is likely smaller if the higher value for the 2013 measurements is attributed to the morning peak from uneven sampling of wind directions. In contrast, the NAEI (which was already underestimating in 2013), has reduced by ~12 % between 2012 and 2017.

Table 3.5: Daily mean values of measured and inventory NO_x emission for the 2013 and 2017 measurement periods

	Daily Mean NO_x Emission mg m^{-2} h^{-1}
Measured 2017	14.29
Measured 2013	15.65
NAEI 2012	11.74
NAEI 2017	10.00

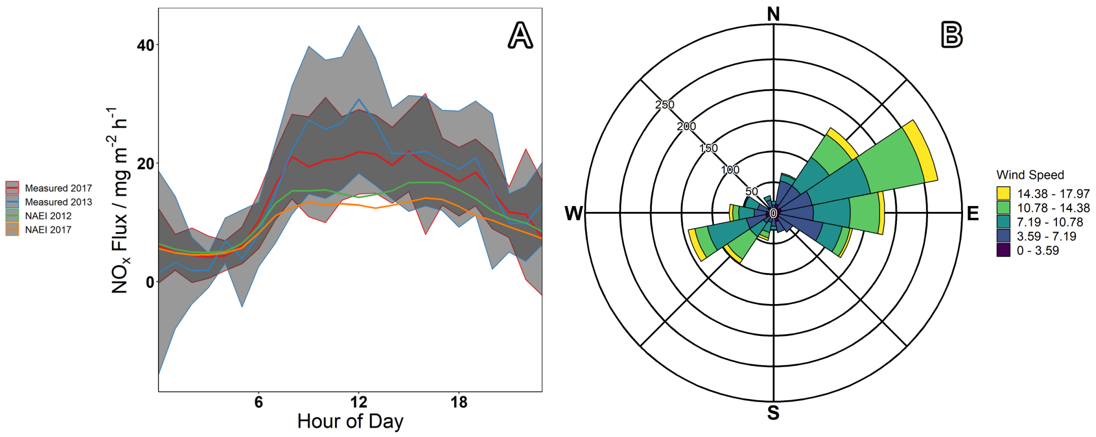

Figure 3.27: A - Comparison of the average diurnal cycle of NO_x flux measured in 2013 (blue) and 2017 (red). Corresponding inventory emissions estimates are shown for the 2012 (green) and 2017 (orange) versions of the NAEI, using 2013 and 2017 footprint models respectively. B - Wind rose for the BT Tower measurements made in 2013. Radial distance shows counts of wind speed measured in a given direction. Paddles are coloured by wind speed bins.

3.5 Summary

During March - June 2017 NO_x flux was measured at the BT Tower in central London via eddy covariance. Maximum daily average emission was observed to the south of the tower, and minimum to the north. The daily averages from the east and west were similar, but the shape of the diurnal profile suggested that there was greater emission the morning than afternoon in the east, whereas emission was more constant throughout the daytime to the west. Using footprint modelling the source area for each hourly measured flux was calculated and used to map emissions to the surface. Enhancements were observed over Euston station to the north east and busy roads to the west and south. Lowest emissions were seen in the area of The Regent's Park to the north east of the site.

The footprint model was used to extract emissions from the National Atmospheric Emissions Inventory. These annual estimates were converted to hourly estimates using a combination of hour of day, day of week and month of year scaling factors for each sector of the inventory. The inventory underestimated the measured NO_x emissions by 1.4 × on average and by a maximum 3.3 × on Saturday afternoons. The inventory showed good agreement with measurements overnight. The traffic sector was found to drive the diurnal variation in the inventory and was as such expected to the source of much of the daytime discrepancy. Comparison with traffic volumes from automatic traffic counters near the BT Tower showed that the decrease in traffic volume at the weekend was less than the decrease in contributions from the traffic sector of the inventory. This suggested that the scaling factors applied may not reflect the traffic activity in central London.

Finally, these data were compared with similar measurements of NO_x emission made at the BT Tower during 2013. Within error, the average measured daily emissions of NO_x had not decreased between the measurement periods, whereas the emissions inventory estimates had decreased by ~12 %. With this underestimation having been shown to be greater in central London (Vaughan et al.) it may be the case that emission from the Greater London area has decreased, but locating these emissions in the region around the tower is not possible with the spatial proxies used to produced the inventory or inventories at resolutions finer than 1 km^2 would be needed to resolve these.

Chapter 4

NO_x Emission Measurement in Delhi

There is continued concern surrounding the effects of air pollution on human health globally. Recently air quality in Asia has been of significant focus, with World Health Organisation reports consistently featuring poor air quality rankings from $PM_{2.5}$ dominated by cites from this region [126]. For the year 2012 India ranked 3rd globally for NO_x and non-methane volatile organic carbon (NMVOC) emissions and 2nd for black carbon (BC) and CO emissions (figure 4.1) [127]. China has the highest emissions for all species in 2012, but recent satellite observations have shown decreases in column NO_2 concentrations [128, 129] however, India's emissions are not thought to have begun to decrease [130].

In India, large population growth has driven worsening air pollution, despite some interventions, beginning with the Air (Prevention and Pollution Control) Act in 1981 which provided powers for the Central Pollution Control Board to introduce measures to manage air pollution. Since then India has adopted emissions control standards (Bharat stages) which mirror Euro standards and apply to newly manufactured vehicles. Many vehicles including all buses, taxis and auto-rickshaws have been converted to compressed natural gas fuel to help meet these standards. However, vehicle density as a function of population doubling in cities across India between 1999 and 2009 coupled with increasing populations means that emissions controls have had limited impact [131]. Some focus has also been placed on improving public transport through building a metro system in Delhi to ease the number of road users, though construction is ongoing.

Premature mortality in Delhi due to poor air quality has been predicted to increase by more than 30,000 deaths per year between 2010 - 2050 (from 19,700 to 52,000 deaths yr^{-1}) if no interventions are made, based on the health effects of O_3 alone [10]. Figure 4.2 shows many air quality monitoring sites in the city breached in the 40 $\mu g\ m^{-3}$ annual air quality limit across during 2018. To further the understanding of air quality in the region, the DelhiFlux project was conducted in 2018, seeking to make direct emissions measurements of a wide variety of air pollutants and use these to assess existing and produce improved inventories.

This chapter details NO_x emissions measurements from two sites and comparisons with the System of Air Quality and Weather Forecasting and Research 2018 inventory.

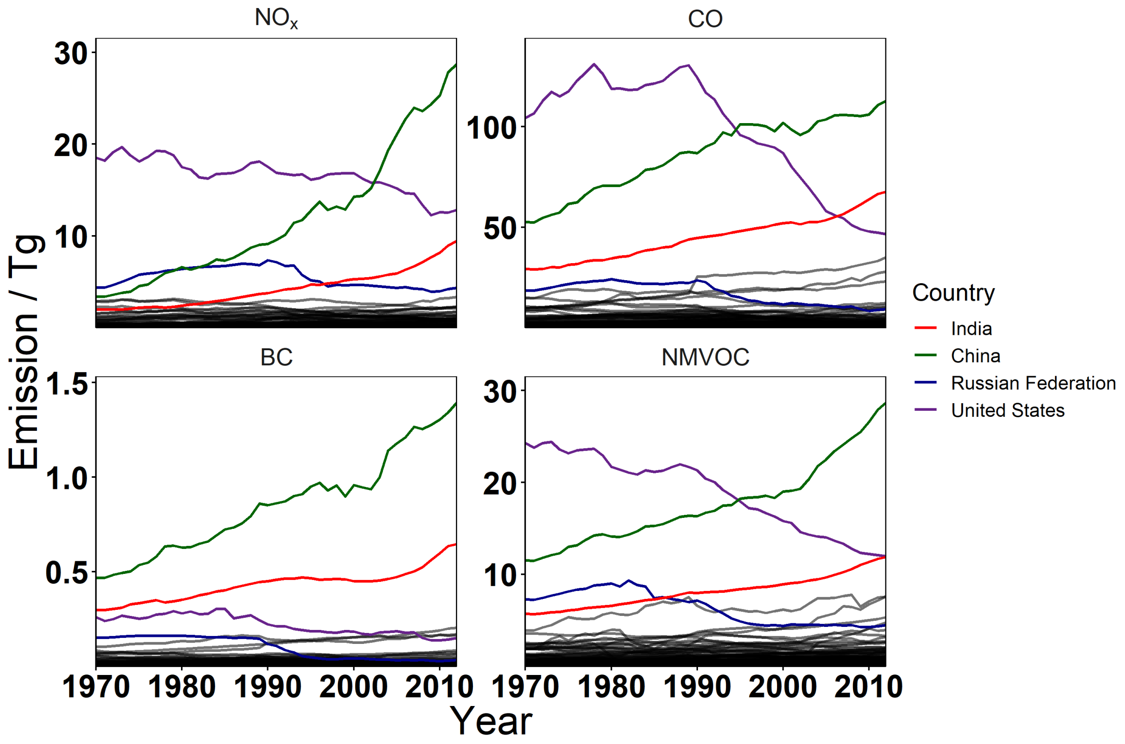

Figure 4.1: Top left - bottom right right; Annual emissions of NO_x, CO, clack carbon (BC) and non-methane volatile organic compounds (NMVOC) by country from 1970 - 2012. The 4 highest emitters of NO_x in 2012 are highlighted on all panes. Data from the Emissions Database for Global Atmospheric Research (EDGAR) [127]

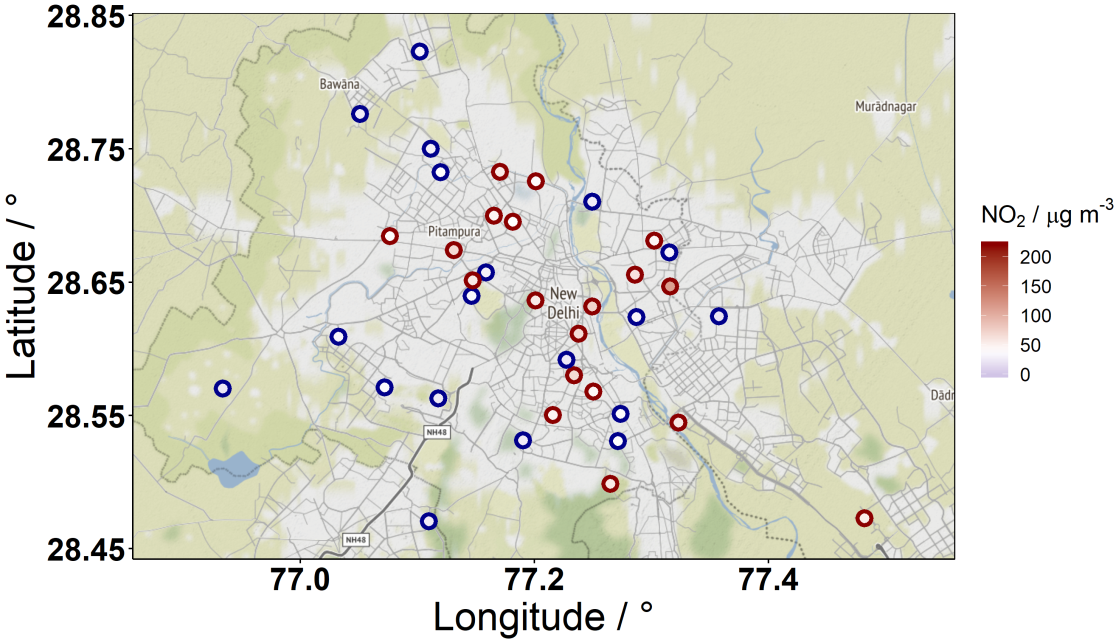

Figure 4.2: Air Quality sites in Delhi. Red border indicates breach of 40 μg m^{-3} annual air quality limit in 2018. Fill indicates annual average concentration measured during 2018 [61].

4.1 Measurements in Delhi

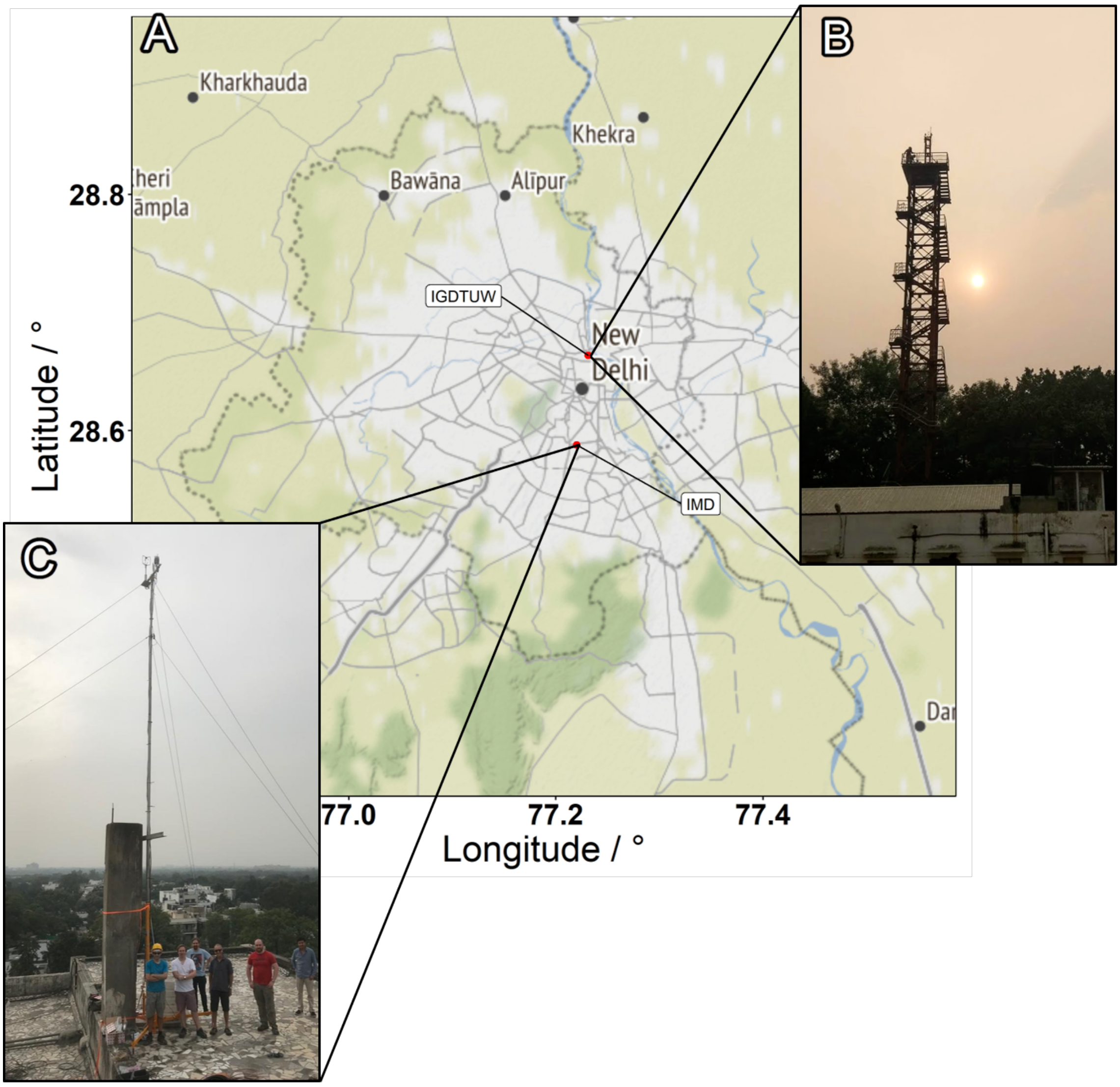

Figure 4.3: A - Location of the Indira Gandhi Delhi Technical University for Women and India Meteorological Department sites. B and C - The flux towers at their respective sites.

4.1.1 Indira Gandhi Delhi Technical University for Women Site Description

The first site was located at Indira Gandhi Delhi Technical University for Women (IGDTUW), on the edge of Old Delhi (lat/lon: 28.664/77.231 °). The area was densely packed with roads with buildings filling most available space, with the exception of the University campus where there was slightly more green space. The roads were highly congested by nature of being located near the Red Fort and Kashmiri Gate - a National Rail station. Measurements of NO, NO_2 , O_3 , CO and SO_2 (instruments detailed in table 4.1) were first taken between 7th October - 1st November from an roof mounted inlet at ~7 m above the ground and were subsequently taken from a 33 m free standing tower during 9th - 23rd November 2018, with the exception of NO_y which was not measured after the move to the tower. Air was pumped down the ~50 m sample line (PFA OD 1/2") at 30-35 ℓ min^{-1} to the instrument located in a 19" rack in a laboratory at the base of the tower.

Table 4.1: Instruments deployed to Indira Gandhi Delhi Technical University for Women, used for concentration and flux measurement during the pre and post monsoon measurement periods. Limit of detection quoted at the listed time resolution, except Aerolaser 5002 where manufacturer quotes at 0.1 Hz. * - Calculated as the median of the standard deviation in the hourly zeros of the instrument during campaign. ** - Temperature calculated from speed of sound.

Quantity	Instrument	Time Resolution / Hz	Limit of Detection	Precision
NO / ppbv	Air Quality Design	5	234*	3 %
NO_2 / ppbv	Air Quality Design	5	294*	4.7 %
O_3 / ppbv	Thermo 49i	0.1	1 ppbv	-
CO / ppbv	Aerolaser 5002	10, resampled to 5	0.8 ppbv	-
SO_2 / ppbv	Thermo 43i	0.1	2 ppbv	-
u, v, w / m s^{-1}	Gill HS-50	20, resampled to 5	0.01 m s^{-1}	-
Temperature** / K	Gill HS-50	20, resampled to 5	0.01 m s^{-1}	-

4.1.2 India Meteorological Department Site Description

The second site was located at the India Meteorological Department (IMD), on Lohdi Road (lat/lon: 28.588/77.220 °). The surrounding area was much less densely packed; many of the structures were civil buildings with large grounds, and the roads were comprised of multiple lanes and as such much more rarely congested. At IMD data coverage is more limited than IGDTUW, with NO and NO_2 (instruments detailed in table 4.2) measured between 29th October - 6th November from a pump up mast situated on the roof of a 6 storey building, providing a similar sampling height of 33 m. Air was pumped down the ~25 m sample line (PFA OD 1/2") at 30-35 ℓ min^{-1} to the instrument located in a 19" rack in laboratory on the 5th storey.

Table 4.2: Instruments deployed to India Meteorological Department, used for concentration and flux measurement during the pre and post monsoon measurement periods. Limit of detection quoted at the listed time resolution. * - Calculated as the the median of the standard deviation in the hourly zeros of the instrument during campaign. ** - Temperature calculated from speed of sound.

Quantity	Instrument	Time Resolution / Hz	Limit of Detection	Precision
NO / ppbv	Air Quality Design	5	216*	3 %
NO_2 / ppbv	Air Quality Design	5	509*	4.7 %
u, v, w / m s^{-1}	Gill R3-50	20, resampled to 5	0.01 m s^{-1}	-
Temperature** / K	Gill R3-50	20, resampled to 5	0.01 m s^{-1}	-

4.2 Air Quality Measurements at IGDTUW

Average NO_x concentrations (figure 4.4) at IGDTUW were lowest at 1400 h (29 ± 9) ppbv but increased drastically overnight to (389 ± 220) ppbv by 2100 h, levels remained high overnight, beginning to decrease again at 0600. This profile was driven by the NO component of NO_x. NO_2 showed two peaks at 0900 and 1700 h of (63 ± 34) and (69 ± 19) ppbv. CO had a similar profile to NO, with its lowest concentration at 1400 (569 ± 155) ppbv and reaching its peak overnight at 2100 h (4382 ± 2306) ppbv. SO_2 had a similar profile to NO_2 , with peak of (8 ± 5) ppbv at 0900 and a slightly later peak at 2100 h of (7 ± 9) ppbv. O_3 peaked at 1300 h with an average concentration of (79 ± 21) ppbv. Overnight the concentration was between 3 and 12 ppbv, however, due to the high concentration of NO at night, this is unlikely to be realistic, and was likely due to interferences from other compounds e.g. the extremely high concentrations and broad mix of VOCs measured at the site [17]. Some peaks were seen in the SO_2 time series at the same time as high concentrations of nighttime O_3 was observed. The UV absorption detection employed by the Thermo 49i detector does have some reported interferences with SO_2 [132]. Because of this O_3 data on the 8th, 16th and 25th of October has been removed, pending further investigation, as high night time O_3 values coincided with high SO_2 concentrations (figure 4.5).

A strong decrease in day time concentrations was observed in all of the measured species except O_3. This was due to extreme dilution from large boundary layer growth; from very low overnight, (40 ± 14) m, to (1350 ± 355) m at its peak during the day. O_3 was formed rapidly enough throughout the day for this effect not to be seen in the diurnal profile. Conversely, high nighttime concentrations are driven by the very low overnight boundary layer. For context the modeled ERA5 nighttime boundary layer height for IGDTUW during the campaign was 10 × lower than at the BT Tower in 2017 (figure 3.8).

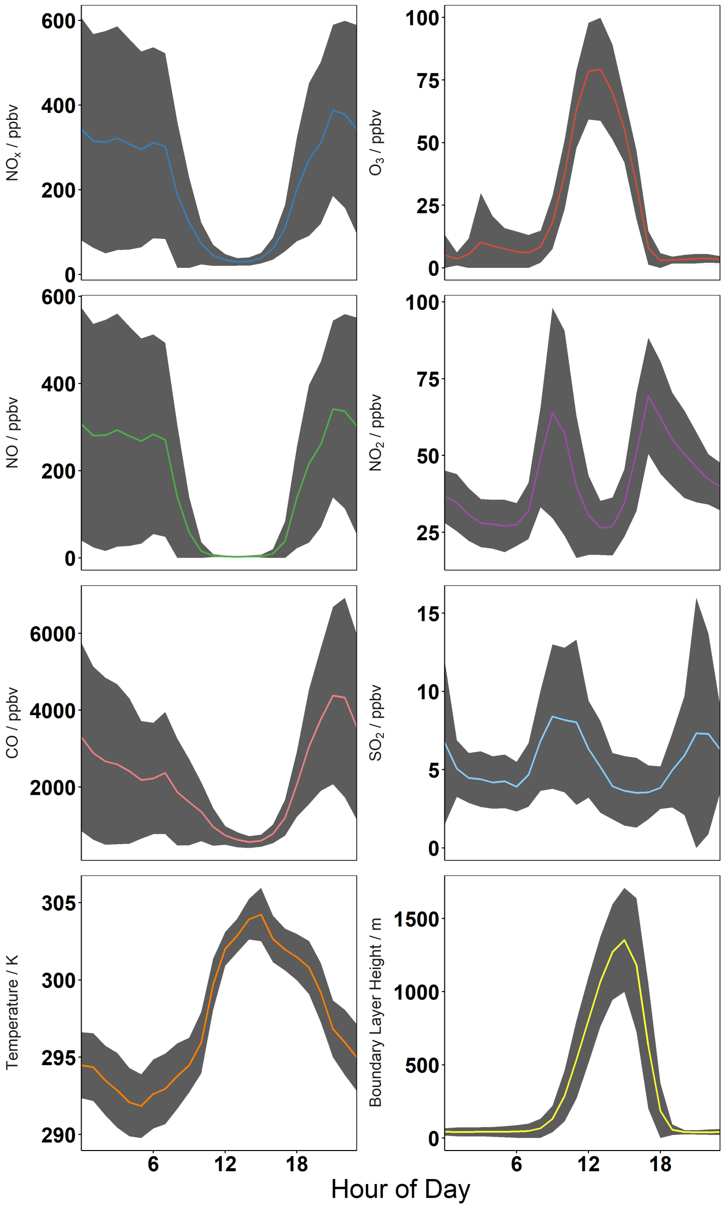

Figure 4.4: Top left - middle right; Diurnal profiles of CO, O_3, NO and NO_2 concentrations (ppbv) measured at the Indira Gandhi Delhi Technical University for Women between 2018-10-07 and 2018-11-01 inclusive. Bottom left - bottom right; modelled temperature (K) and boundary layer height (m) from ERA5 [113]. Shaded regions correspond to standard deviation in diurnal averaging

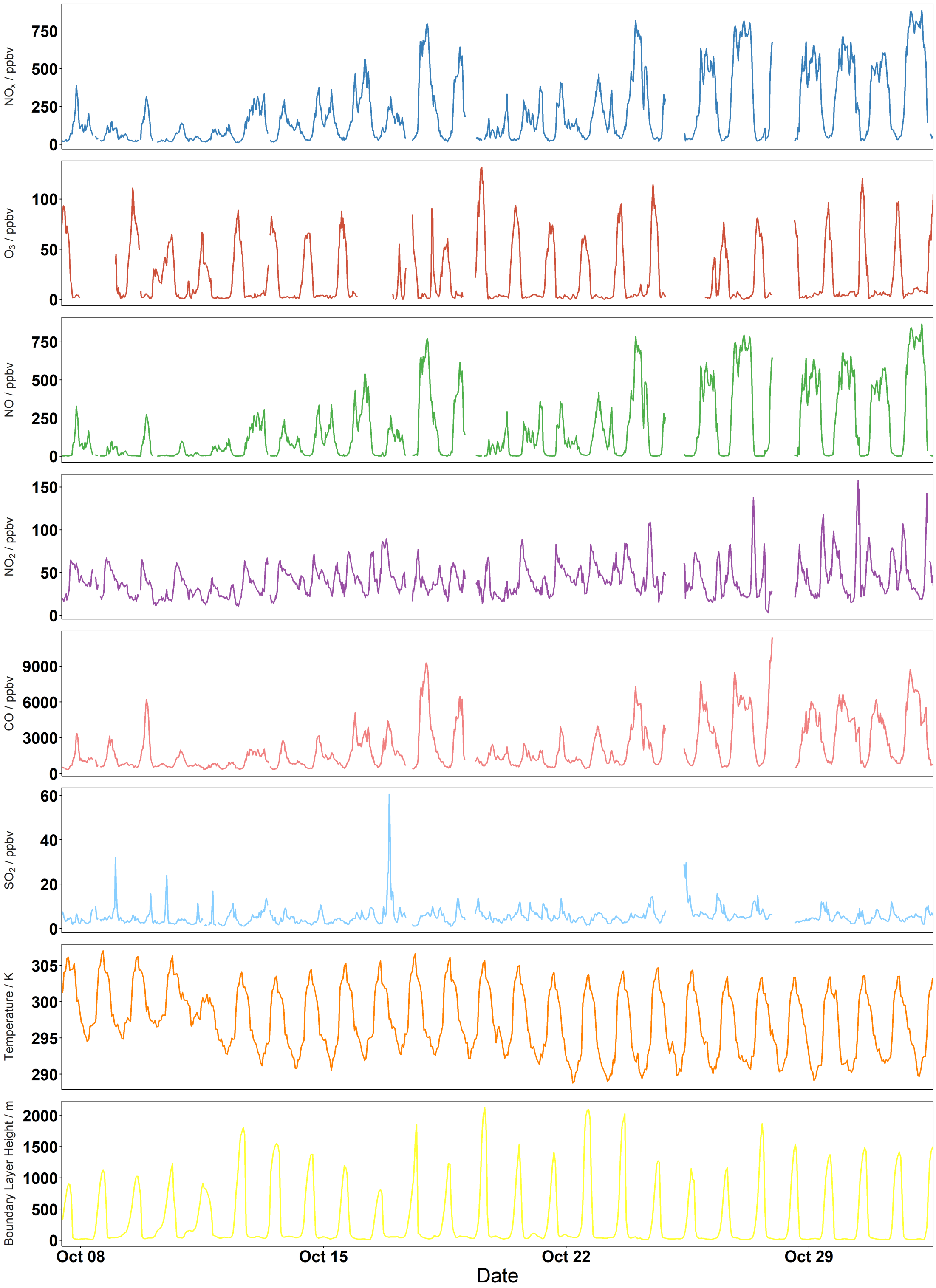

Figure 4.5: Top - bottom; Time Series of CO, O_3, NO and NO_2 concentrations (ppbv) measured at the Indira Gandhi Delhi Technical University for Women between 2018-10-07 and 2018-11-01 inclusive. Modelled temperature (K) and boundary layer height (m) from ERA5 [113]. Shaded regions correspond to standard deviation in diurnal averaging

In figure 4.6 the concentrations of NO_x and CO are compared with respect to wind speed and direction. Panels A and B show that both NO_x and CO were enhanced at lower wind speeds and between 180 ° and 270 °. The NO_x to CO ratio shown in panel C shows higher ratios to the west than east. Both NO_x and CO share combustion sources but as CO's lifetime is much longer in the atmosphere than NO_x , a higher NO_x / CO ratio is indicative of one of these sources nearby. Enhancement in NO_x / CO was observed in most directions at a range of wind speeds suggesting a well distributed source. Traffic is the only source that was homogeneous enough nearby for this. In addition, the site was located on the western edge of IGDTUW, closer to congested roads, whereas to the east, although the major traffic source was a highway, this was less congested and separated from the site by green space and buildings within the campus, furthering traffic as the dominant local source of NO_x. Panel D shows the Pearson correlation between NO_x and CO. Variation in the correlation would be suggestive of separate sources dominating the NO_x and CO concentrations respectively. For the majority of wind speeds and directions this was not the case, with correlation being > 0.75. The exception to this being at higher wind speeds to the south-east. In the time series, CO is enhanced but NO_x is not, suggesting either a separate source for CO, or that this was from a long-range source, far enough that NO_x was mostly lost. These particular conditions were only sampled during one short contiguous period on 10th October, requiring more data before this can be understood.

In figure 4.7 SO_2 and CO concentrations are compared, again with respect to wind speed and direction. The profile of SO_2 differs to that of CO, indicating non-traffic sources. Indeed, SO_2 is primarily emitted from the burning of coal based solid fuels, such as those used in power generation or industrial processes. The main enhancements in SO_2 were seen 1 - 2 m s^{-1} to the east and at wind speeds $\geqslant$ 4 m s^{-1} in the south-east, the latter aligning with the decreased correlation of NO_x / CO. The former was driven by one high SO_2 event on 16th October, where concentrations peaked at 2130 at 60 ppbv. Filtering this event removes the enhancement from figure 4.7-A, suggesting that this was driven by a local, irregular event. The enhancement to the south-east is highlighted by figure 4.7-C, suggestive of a longer range combustion source. As noted in the NO_x / CO comparison this air mass was sampled on the 10th of October. These were the final few days of operation of the Badarpur Thermal Power Station, which shutdown on the 15th of October, which is possibly the source of this enhancement, being far enough away that the signature from NO_x / CO was not present due to NO_x loss processes, but SO_2 remained [133]. Panel D shows increased correlation between SO_2 and CO in small areas to both the east and west of the site at moderate wind speeds. These may indicate domestic solid fuel burning, as their effects on overall concentrations are limited, but do correlate with CO as burning sources.

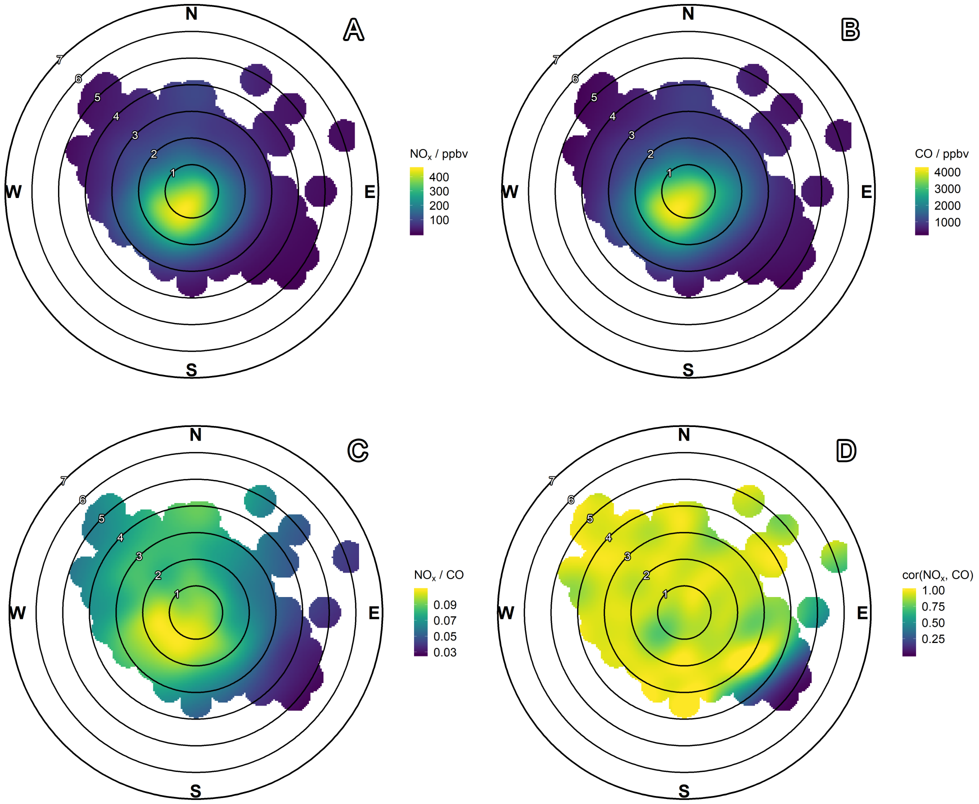

Figure 4.6: Concentration surfaces measured at IGDTUW by wind speed and direction. A - NO$_x$ /ppbv, B - CO /ppbv, C - NO$_x$ /CO ratio, D - NO$_x$ - CO Pearson correlation.

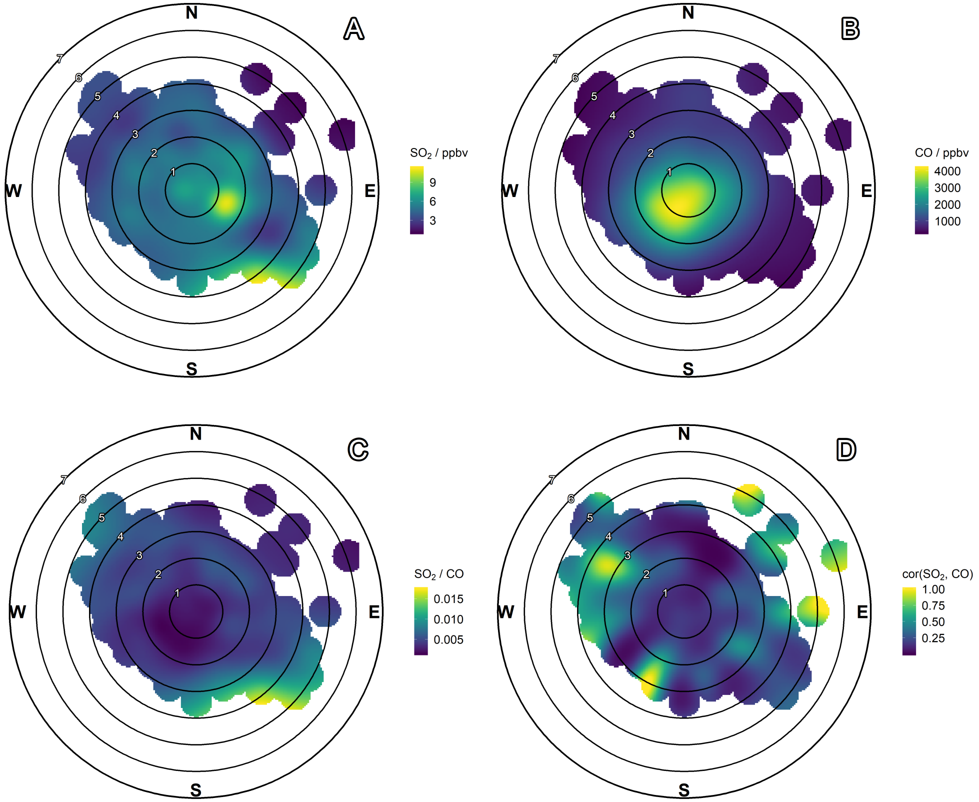

Figure 4.7: Concentration surfaces measured at IGDTUW by wind speed and direction. A - SO_2 /ppbv, B - CO /ppbv, C - SO_2 /CO ratio, D - SO_2 - CO Pearson correlation.

4.3 Eddy Covariance: The Two Towers

4.3.1 Instrument Calibration

Manual calibrations were run on the instruments at regular intervals throughout the campaign, following the proceed described in section 2.1.2. Sensitives at IMD remained relatively constant (CH1: ~1.4 CH2: ~2.4) where as at IGDTUW they declined steadily over the measurement period. Beginning at CH1: ~4.2 , CH2: ~3.6, they ended the campaign as CH1: ~2.4, CH2: ~1.9 (counts pptv$_{-1}$) so coefficients were linearly interpolated over the measurement period. NO standards traceable to the NPL NO scale were flowed into the instruments at ~10 sccm to provide the span for calibration. Calibrations were repeated in field until coefficients were stable and anomalous calibrations were ignored during data workup.

4.3.2 Eddy Covariance Methods

Data pre-processing and eddy covariance methods used for these data were selected (table 4.3) as a part of a working group to unify the processing methods across the DelhiFlux project. These were identical to those applied in section 3.1.3 with the exception of the aggregation period. The lower sampling height allowed the use of a 30 minute aggregation period due to the reduced low frequency eddy contributions.

Table 4.3: Eddy Covariance Settings for IGDTUW and IMD

	Setting
Aggregation Period	30 minutes
Detrending	Linear
Lag Time	Windowed Range -20 - 0
Rotation Method	Double

4.3.3 Results

At IGDTUW 665 thirty minute NO and NO$_2$ fluxes were calculated between 9th - 23rd November 2018. Of these 457 were considered to be of high quality by the eddy4R QA/QC routines (section 2.3.1). At IMD 386 thirty minute NO and NO$_2$ fluxes were calculated between 29th October - 6th November 2018 (figure 4.8) . Of these 181 were considered to be of high quality. Both measurement locations suffered from periods of low turbulence, especially at IMD, so data obtained when u^* was less than 0.175 m s^{-1} was flagged in addition to the QA/QC routines. Figure 4.8 shows data filtered based on the eddy4r QA/QC, and flagged by u^*. The combined QA/QC and u^* filters are applied in future data processing.

Under these low turbulence conditions there was increased probability of emission being trapped below the sample inlet by residual layers and being released at a later time and as such a storage flux correction term was applied. This correction factor was calculated as of equation 4.1 and was added to the calculated flux [134, 135].

$$Fs_t = \frac{C_{t+i} - C_{t-i}}{2 \cdot t_{agg}} \cdot h \tag{4.1}$$

Where:

- Fs_t - Storage correction factor at time t
- $C_{t\pm i}$ - Concentration one aggregation period before or after time t
- t_{agg} - Duration over which the flux has been aggregated
- h - Tower height

In figure 4.9 the average diurnal profiles of NO_x concentration (A) and flux (B) are compared between sites. Both sites saw similar concentration profiles, with the lowest concentrations during the day and highest overnight caused by dilution/concentration from the boundary layer (section 4.2). Although, the NO_x concentrations were similar at both sites, emission was 4 - 5 × higher at IGDTUW. At both sites emission began to increase at 0600, at IMD it reached (2.8 ± 5.0) mg m^{-2} h^{-1} at 1000 and peaked at (4.52 ± 1.3) mg m^{-2} h^{-1} by 1500, whereas at IGDTUW it peaked at 1000 with a value of (19.4 ± 6.1) mg m^{-2} h^{-1} and remained above 10 mg m^{-2} h^{-1} until 1800, at which point it decreases to its overnight value of ~ 3 mg m^{-2} h^{-1}. At IMD this decline was less pronounced, with emission remaining around ~ 3 mg m^{-2} h^{-1} until 0000 where it declined to (0.5 ± 0.42) mg m^{-2} h^{-1} by 0400. This sustained nighttime emission may have contributed to the higher overnight concentrations observed at IMD.

This difference in emission may be due to the limited spatial area sampled by the emissions measurements. Mixing of ambient concentrations will occur on larger spatial scales than the areas from which emission was sampled. For example, although the emission measured at IMD was lower, there may have been emission from outside the flux footprint that was responsible for the increased concentration. By nature of the EC method, this increased background does not influence the emission as it has no impact on the covariance between the immediate fluctuations of the vertical wind and concentration.

The overall effect on the diurnal profile was minimal, with a small decrease of emission in the morning and a slight increase in the afternoon, and the storage corrected data has been used going forward, except in the sensor comparison in the following section.

Figure 4.9 shows the average diurnal profiles of NO_x concentration and storage corrected flux at both sites. The measured emission was ~4 - 5 × higher at IGDTUW than IMD across the day. Based on the locations of the measurement towers, this is expected, significantly less busy roads around IMD compared with the near constant congestion around IGDTUW would mean any similarity in magnitude of NO_x flux between the sites would be surprising. However, what is unexpected is the lack of difference between the concentration profiles. With the exception of a slightly lower early morning concentration at IGDTUW, which may simply be due to the greater amount of data available to average over, the profiles are identical. It is noted that ambient concentrations would not be expected to be entirely correlated with local emission, as they are determined by transport from surrounding areas as well, the seeming complete lack of response is curious. The measurement platform location could be the route cause; these concentrations are measured aloft, if roadside concentrations were measured at both sites, it may be found that IGDTUW does indeed have higher concentrations. Alternatively, emissions at the site may be comparable, but the footprint at IMD does not substantially capture the local sources that drive the concentrations measured. Neither of these points can be refuted satisfactorily from these measurements, but counter arguments may go as follows: both sites concentrations were measured at similar heights, and whilst IGDTUW measured closer to the roads, IMD would not be considered distant, and as such any loss or dispersion masking the road side concentrations would be minimal. Based upon the footprint analysis conducted in section 4.3.4, IMD does capture local roads, so will see contribution from them.

If it can be accepted from this that the similarity of measured concentrations at the two sites, when compared to their remarkably different local emissions is indeed unexpected, some questions are raised about how policy interventions based upon concentration measurements alone would fair. Based upon the similarity of the concentrations, it may be expected that interventions may be equally effective at both locations, whereas when looking at the emissions there is more potential for reduction at IGDTUW than IMD. It is of course impractical to have emission measurements of large areas of a city, so instead linking them with emissions inventories can be used to scale their findings to the wider area. To this end section 4.4 will compare these measurements with a local inventory.

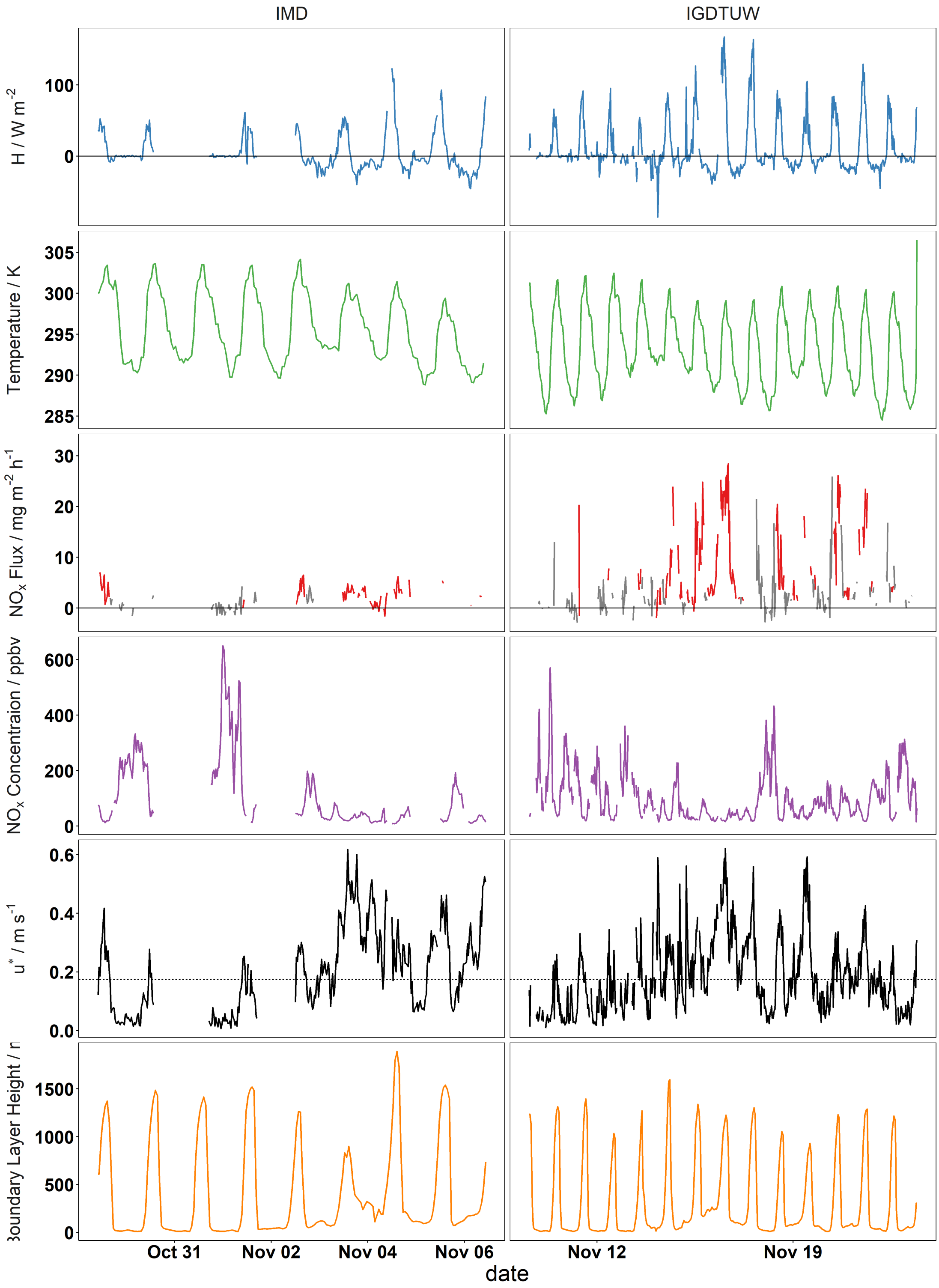

Figure 4.8: Left - Right: Time series data measured during the flux period at IMD and IGDTUW. Top - Bottom: Sensible heat flux (W m^{-2}), temperature (K), NO$_x$ flux (mg m^{-2} h$_{-1}$), NO$_x$ concentration (ppbv), friction velocity (m s^{-1}) and modelled boundary layer height (m). Broad data gaps at IMD are due to instrument failure caused by a faulty O$_2$ generator . NO$_x$ flux is only shown where it has passed the QA/QC routines, and is coloured grey when friction velocity falls below 0.175 m s^{-1}.

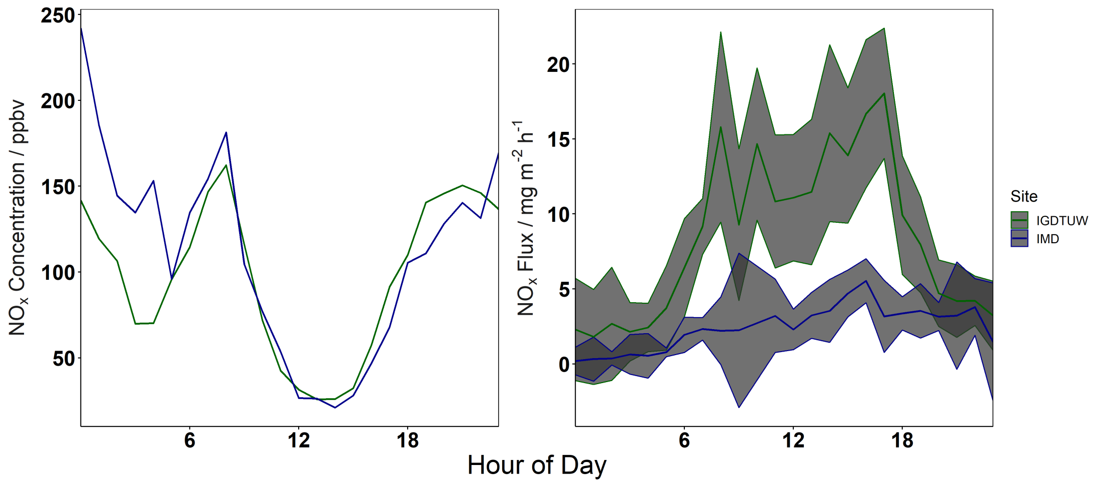

Figure 4.9: Left - Hourly averaged, storage corrected NO_x concentrations at IGDTUW (green) and IMD (blue). Right - Hourly averaged NO_x flux for both sites.

4.3.4 Footprint Modelling

Footprint models were run for both sites using the method described in section 3.2. Both sites mean footprint maxima distance were ~225 m from the tower and had a mean 90 % fetch of 950 m. The campaign averaged footprint have been mapped in figure 4.10. From these maps some of the differences between the emissions at each site can begin to be inferred. The source area for IGDTUW includes the highway interchange to the north east, a significant source of traffic emission on roads with much greater traffic flow than the roads surrounding the IMD site. Indeed, using the same mapping method from section 3.2 the northerly direction towards this interchange was highlighted as a source of NO_x emission (figure 4.11-A). Moreover, a general east/west split was observed, with enhanced NO_x emission in the western portion. From the satellite images which these emissions maps are overlaid, the increased road density is visible to the west of the measurement site, which explains why there was increased emission in this direction; even thought the highway runs to the east, it is surrounded by green space and bounded by the river, limiting addition emission. It should be noted that there was somewhat less data to input for this analysis so the uncertainties discussed alongside the London analysis are amplified, and it is not possible to be as specific about sources.

There was not enough NO_x data available at the IMD site to perform this analysis, however, NO_2 was measured via a quantum cascade laser (QCL) by the Centre for Ecology and Hydrology (CEH) co-located with the AQD instrument. Figure 4.12 shows the time series and diurnal cycle of the two sets of measurements. While there are co-temporal data from both instruments, the NO_2 fluxes show reasonable agreement (Pearson correlation 0.86), and the additional data in the CEH time series does not largely change the average diurnal from the shorter time series. As the shorter time series appears to be representative of the longer

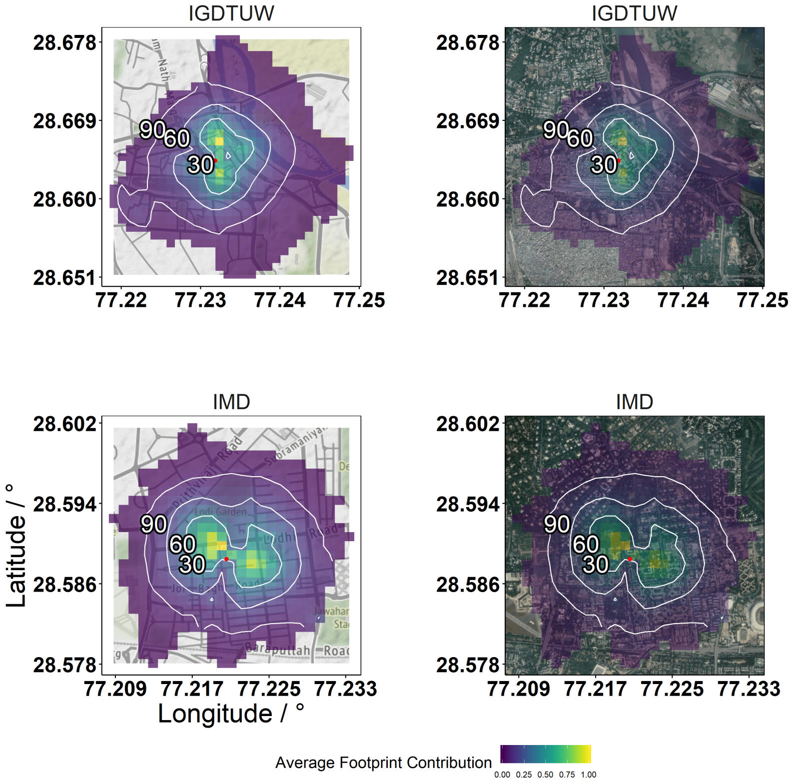

Figure 4.10: Flux footprint averaged over the sampling period. Colour represents normalised contribution to the measured flux. Contours mark the regions of 30, 60 and 90 % contribution to flux. Red point shows the location of the flux towers as IGDTUW and IMD.

NO_2 measurements made at IMD and under the assumption that NO measurements are similarly representative, the shorter time series but containing both NO and NO_2 measurements has been used for the inventory analysis (section 4.4). However, for the surface mapping exercise, the longer combined UOY and CEH NO_2 time series has been used, where CEH gap fills where UOY data was unavailable. This is because more individual footprints are required to drive the analysis. Using NO_2 adds uncertainty to the source of emission as it is not a conserved quantity, but in an attempt to demonstrate this the IGDTUW analysis has been performed for both NO_x and NO_2. Figure 4.11-B does not show a significantly different pattern from figure 4.11-A, so using NO_2 at IMD is not completely misleading. Figure 4.11-C shows the mapped NO_2 emission from the combined time series. The emissions are much more uniform surrounding IMD, but there was slight enhancement to the north, towards the main road outside of the compound, and reduced emission with the compound.

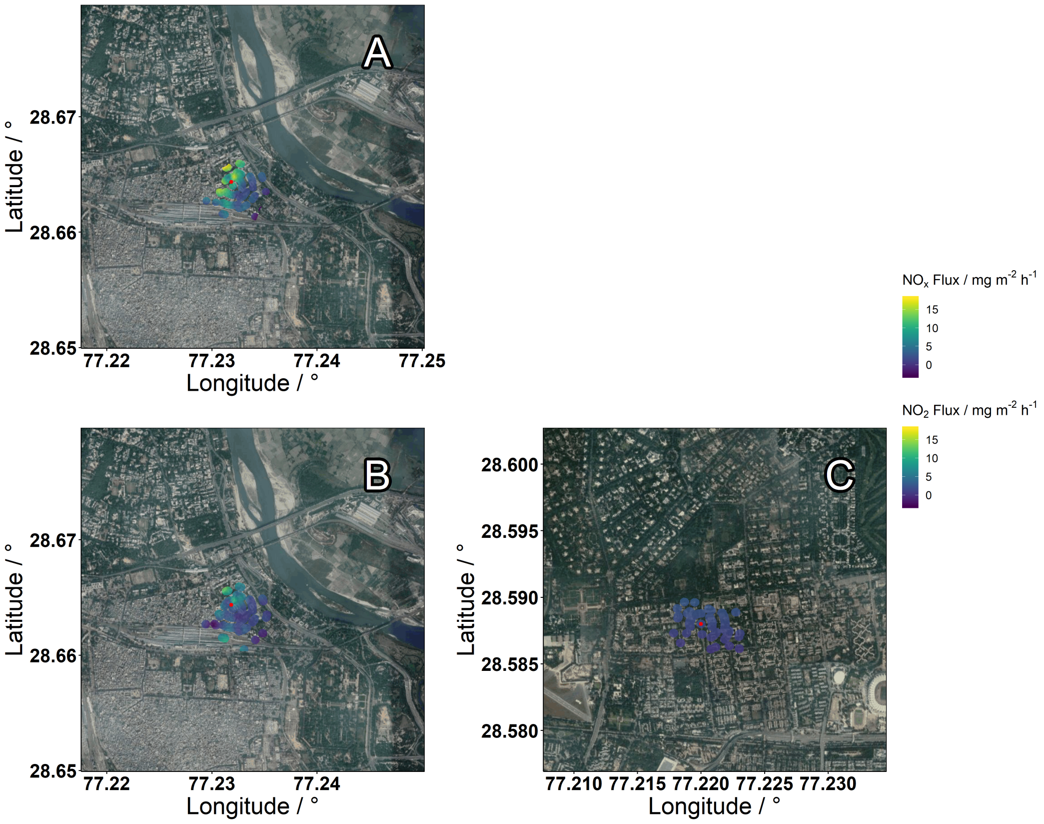

Figure 4.11: Flux surface as a function of along-wind distance to the maximum flux contribution on the radius and wind direction. A - NO$_x$ flux at IGDTUW, B - NO$_2$ at IGDTUW, C - NO$_2$ flux at IMD.

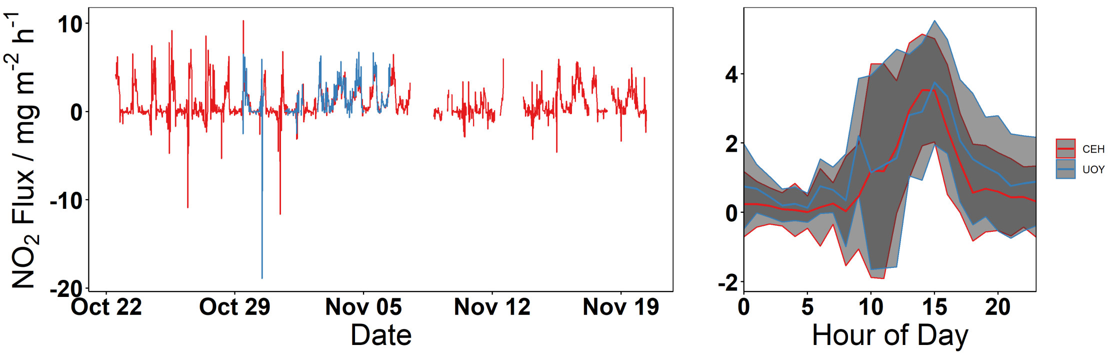

Figure 4.12: Comparison of raw NO_2 fluxes measured using the University of York's AQD instrument (UOY, blue) and the Centre for Ecology and Hydrology's QCL (CEH, red). Both the time series (left) and average diurnal profile (right) are shown. Shaded region on the diurnal profile shows the standard deviation in diurnal averaging

4.4 Inventory Analysis

4.4.1 The SAFAR Inventory

The System of Air Quality and Weather Forecasting and Research (SAFAR) inventory is developed by the Indian Institute of Tropical Meteorology, Pune, the IMD and the National Centre for Medium Range Weather Forecasting. It is a programme designed to provide air quality and weather forecasts in several cities across India, combining monitoring network data and models to produce the air quality index and communicate this to the public. As a part of the APHH - Delhi programme, an emissions inventory was provided by SAFAR. The inventory gave 400 $\times$ 400 m resolution across the Delhi, and was separated in 5 source sectors; transport, residential, industry, thermal power and other. The residential sector included emissions from cow dung, slum areas, diesel generators, street vendors, residential cooking and crop residues and the other sector included emissions from municipal solid waste burning, crematoriums, incense sticks and brick kilns. The transport, residential, other and industry sectors are shown in figure 4.13, thermal power is not displayed as there are few grid cells that this sectors affects, and they do not appear withing the flux footprints of the measured emissions. Note that the values are shown on a $\log_{10}$ scale to preserve structure, as the transport layer contributes the overwhelming majority of NO_x emissions.

4.4.2 The Traffic Sector

As mentioned in section 4.4.1, the transport sector contributes large amounts to the NO_x emissions described by the inventory. Through other investigations within the project by the Cambridge Environmental Research Consultants (CERC, [136],[137]), the road transport section was shown to be overestimating NO_x emission. Back calculated annual average daily traffic (AADT) flow from the inventory showed unrealistic traffic flows (~3 million vehicles per day) on some roads. An estimated emission was calculated based on vehicle age and type in the Delhi fleet, and applied by road type to the inventory grid. When AADT flows were recalculated, most road types fell within expected ranges. This version of the inventory is referred to as CERC V1 herein. Additionally, for minor and unmetalled (gravel) roads, AADT flows were still somewhat higher than expected, so emissions from these were reduced to a quarter of the modal flow. This version of the inventory in referred to as CERC V2 herein. Finally, the traffic sector shows a regular pixelation, which appears to be an gridding artefact. An additional processing step was applied, where grid cells that occur on this regular pattern were replaced with the median of the surrounding tiles. This method does cause some of the spatial information to be lost, as this correction has been applied geometrically rather than reconstructing the inventory to whilst avoiding the artefacts. Because of this the original inventory is also compared against the improved versions, resulting in six versions of

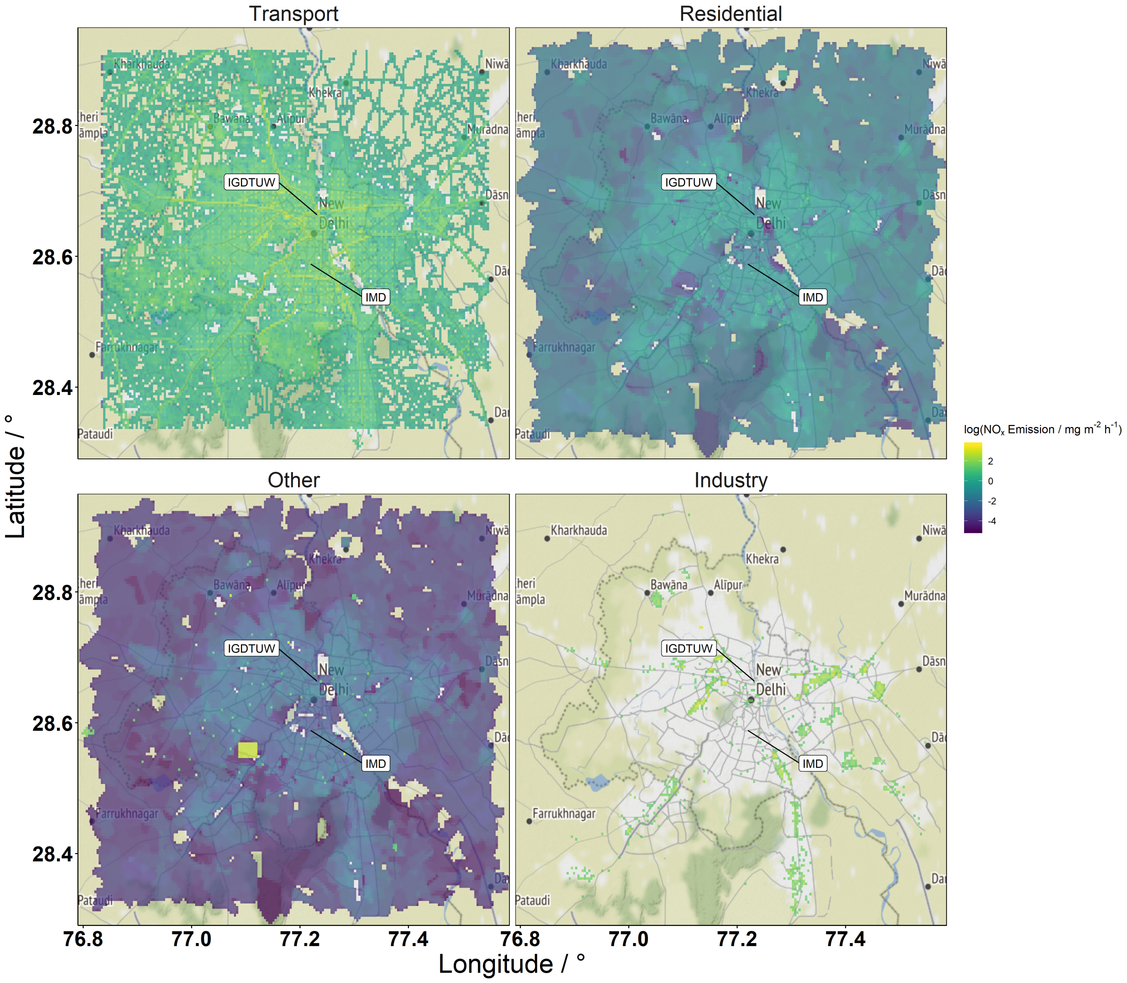

Figure 4.13: The four layers of the SAFAR inventory for 2018 coloured by log$_{10}$(NO$_x$ Flux / mg m^{-2} s^{-1}).

the transport layer.

In figure 4.14 the three versions of the transport layer of the inventory are shown with and without the median removal post-processing of the pixelation. There was significant reduction of NO$_x$ emission from transport between the base SAFAR inventory and the two CERC inventories and high values due to pixelation are not present in the median version of each. Due to a lack of scaling factors for this inventory, the factors used in 3.3.2 have been applied to the data, and average diurnal profiles of estimated emission from the SAFAR inventory for each of the transport layers. The clearest difference between the base SAFAR inventory and those that used the CERC transport layers was seen at IGDTUW, with both the CERC versions ~3- 4 × lower. At IMD the major difference was between the CERC V1 and V2 inventories. This shows that emission at IGDTUW was being influenced mainly by larger roads and highways, such that first AADT flow correction influenced these the most, whereas emission at IMD has more influence from minor roads, so the reduction in emission from these has the greater effect. CERC V2 with median correction was selected for further comparison as this had the best agreement with both measurement sites (figure 4.14-bottom).

4.4.3 Comparing Eddy Covariance and Inventories

From figure 4.15 the inventory, after all the corrections, still overestimates the emissions at both sites by ~2 × at IGDTUW and ~4 × at IMD, during the day. Both sites see improved agreement overnight, but the inventory does not reach the nighttime values as rapidly as the measurements. However, the diurnal profile of the inventory was imposed entirely by the scaling factors, which may not accurately describe the activity in an India city, as they have been derived for use in Europe [122–124]. As such, the measured diurnal cycle was used to impose a second set of scaling factors. These were created from the measured and inventory IGDTUW time series, as these are longer than IMD. The average diurnal profile of the un-scaled inventory time series was first down-scaled by the by the ratio of the daily mean of measured and un-scaled inventory diurnals, effectively normalising the un-scaled profile about 1 . The ratio between the newly scaled inventory profile and the measured was calculated, producing hourly scaling factors. These factors were then applied in place of the European scaling factors to both the IMD and IGDTUW emissions estimates. There was only slightly improved correlation between time series at IGDTUW (Pearson correlation coefficient 0.55 -> 0.58) but much greater improvement at IMD (0.09 -> 0.31), however it remained that neither site's inventory time series showed excellent correlation with measurements (figure 4.16).

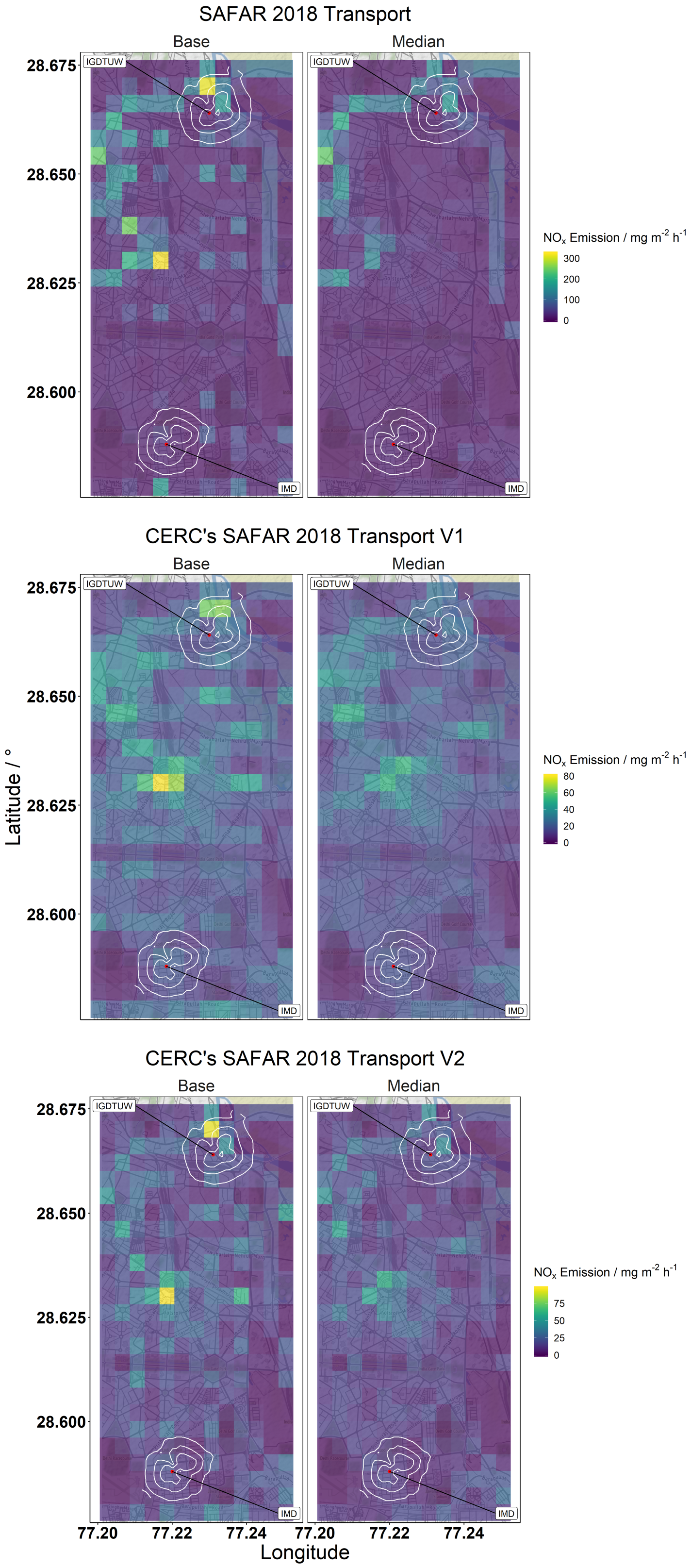

Figure 4.14: Inventory Transport Layers. Top - Bottom; the three source inventories - Original SAFAR, CERC v1 (traffic flow recalculation), CERC v2 (minor road adjustments). Left - Right; base inventory, pixelation pattern replaced by median of surrounding cells.

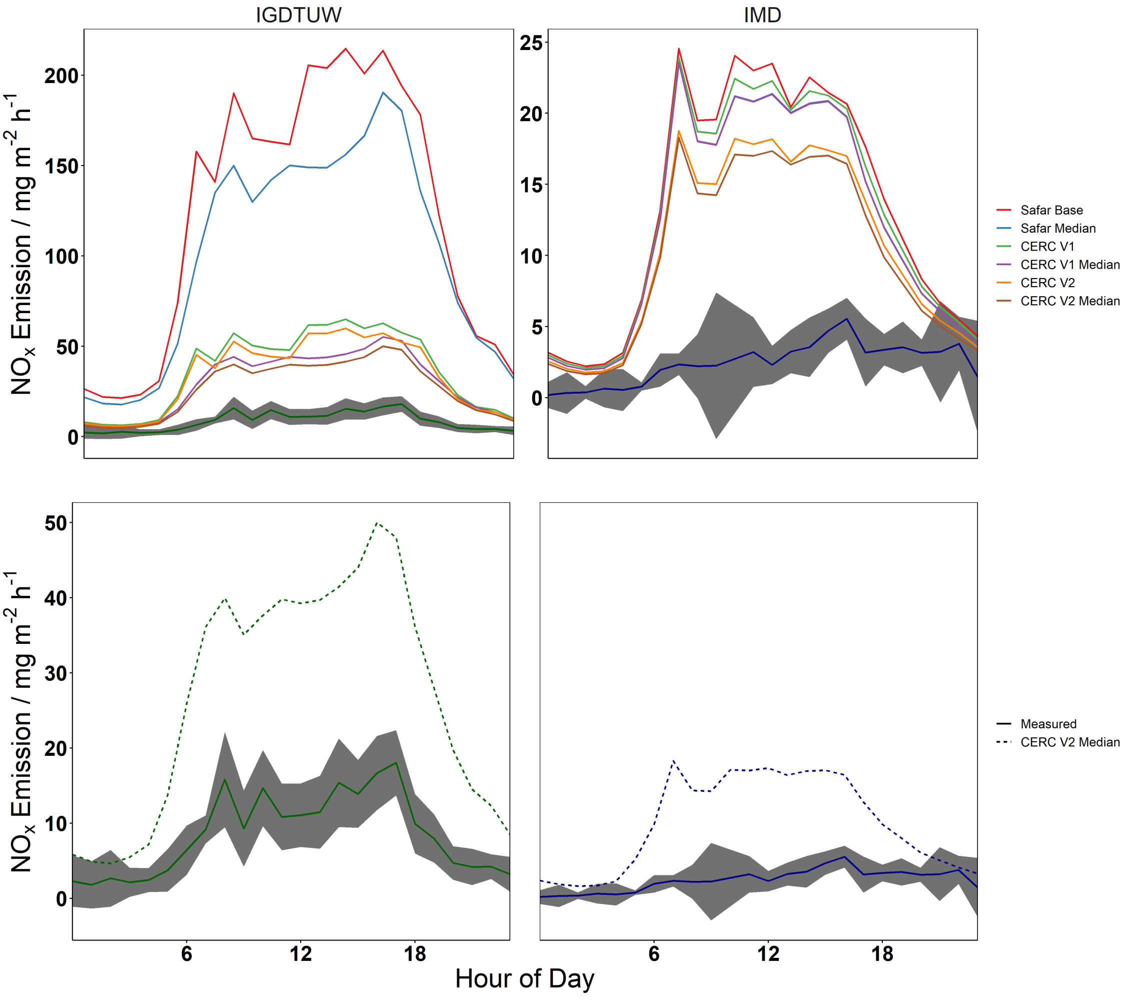

Figure 4.15: Comparison of the average diurnal profiles of measured flux and estimated emission from inventories. Left - right; IGDTUW - IMD. Top - Bottom; All inventory types (see figure 4.14) on site specific y scales, measured and CERC v2 emissions on shared y scale.

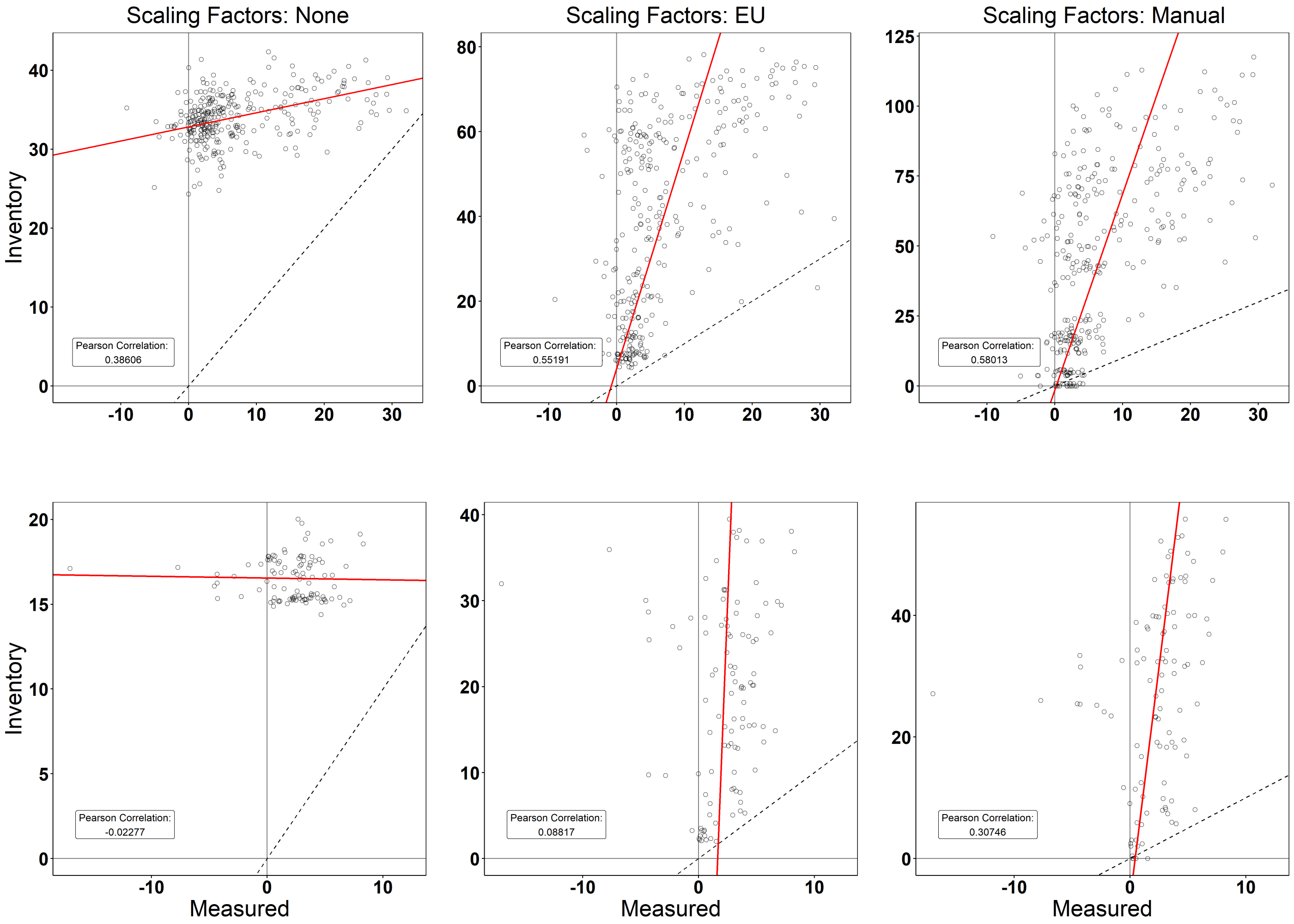

Figure 4.16: Inventory vs measured NO$_x$ emission time series at IGDTUW (top) and IMD (bottom) using, from left to right, no scaling, European scaling, and experimentally derived scaling factors on the inventory data. The red line shows an orthogonal regression, and the dashed line is x = y.

The inventory does capture the relative difference between the sites reasonably well. The measured daytime emission was ~3 - 4 × lower at IMD than at IGDTUW and the emissions estimate was ~2 - 3 × lower. As discussed previously, one of the differences between the measurements may be that local emissions were not fully captured at IMD due to the small flux footprint and as such the emissions from IMD might be expected to be higher if more of the surrounding roads were captured. As the inventory is limited by its spatial resolution, these road emissions span the whole grid cell, raising the emissions estimate leading to the lower IGDTUW/IMD ratio when compared to the measurements. The limited spatial resolution may also describe why low correlation between the measured and estimated emission was observed. The effect of road traffic sources dominating entire grid boxes is diminished when averaged over the measurement periods, meaning that the relative difference between average diurnal profiles for the sites was well represented, but the low correlation for each site with the inventory was due to the footprints sensitivity to these over represented roads.

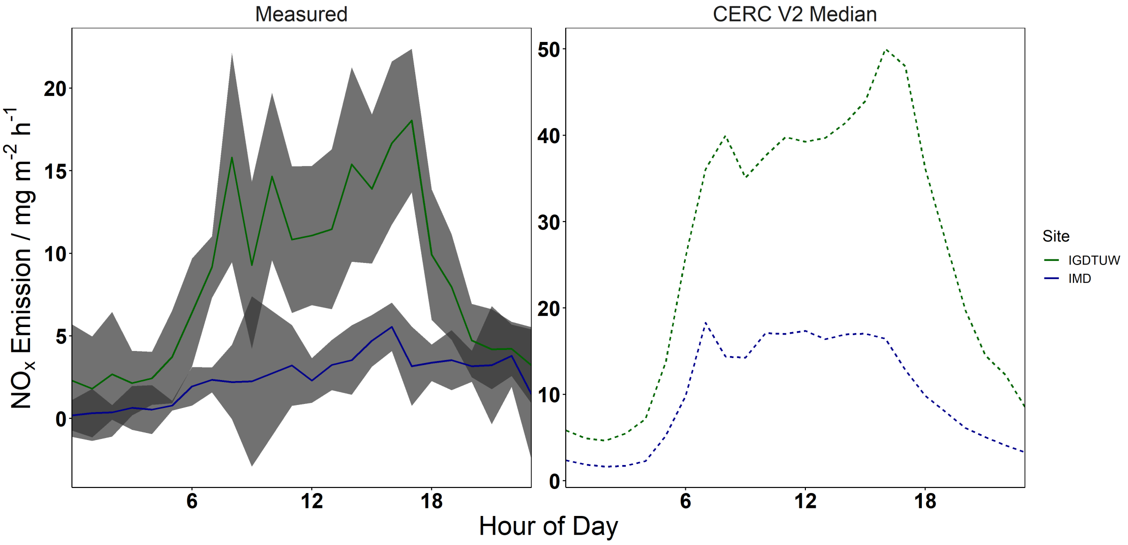

Figure 4.17: Average diurnal profiles of measured (left) and estimated (right) emissions. Although the estimated emissions overestimate when compared to the measured, the ratio between the sites is similar in both cases.

4.5 Summary

NO_x emission was measured at two sites in Delhi during October and November 2018. These sites had starkly different surroundings and measured emissions reflected that. At the India Gandhi Delhi Technical University for Women site, a site surrounded by densely packed roads and little green space, average daily emission of NO_x was 4 - 5 × higher than at the India Meteorological Department. This site had contrasting less traffic and more green and open space. Despite a significant difference in local emission, concentration measurements at both sites were roughly similar on average. The agreement amongst the concentration measurements was due to the more background measurement of concentration, allowing for mixing from emission sources outside of the flux footprint. However, this does demonstrate that a good understanding of the heterogeneity in emissions, not just concentration, in an urban area is key for allowing interventions to be targeted in areas where they will have the greatest effect.

As it is infeasible to take eddy covariance measurements over the whole of a city, these measurements were compared to the several versions of the SAFAR emissions inventory. The version with corrections to the traffic emissions layer and gridding artefacts had the best agreement with measured emission, though still overestimated by 2 - 3 ×. Some of this was due to the lack of local scaling factors to transform the inventory from an annual estimate to a diurnal profile, but much was likely due to the remaining uncertainty in the traffic emissions in Delhi. Although the inventory did not accurately capture the emissions in absolute terms, the difference between the sites was reasonably well reflected. In the inventory emissions surrounding similarly higher at IGDTUW than those at IMD, suggesting that the underlying data which allows the emissions to be spatially resolved in the SAFAR inventory are fairly good. The main discrepancy between measurement and inventory was in the absolute magnitude, although experimentally derived emissions factors gave limited improvements to correlation with measurement, suggesting that the large traffic sources being spread across whole grid cells is not compatible with the footprint modelling at a time series level.

Chapter 5

Bulk London NO_x Emissions measured from an Airborne Platform

Data collected on three flights by the UK's Facility for Airborne Atmospheric Measurement (FAAM), one in 2016 and two in 2017, were used to calculate the NO_x emission from London, UK. These aimed to provide an emissions estimate from Greater London and the surrounding areas, in contrast to a small area of central London measured in chapter 3. To do this a mass balance approach was employed, using data collected in westerly outflows into the Thames Estuary to construct a vertical profile of the plume via kriging interpolation. Combined with the vertical profile of horizontal wind speed an and an estimation of the background concentration an emissions rate can be calculated.

To link these emissions to the surface and allow for comparisons to the NAEI, a footprint was constructed using backwards particle dispersion models from the Hybrid Single Particle Lagrangian Integrated Trajectory Model (HYSPLIT).

In this chapter the mass balance method, including the kriging interpolation and background determination methods, are discussed, as are the methods used to generate the footprints. As well as using the footprint to determine the emissions source area, it was also used to help correct the inventory comparison for chemical loss of NO_x between emission and measurement, as this was on the order of several hours. Additionally, the inventory was scaled using the factors detailed in section 3.3.2. As the sampling area was much larger, the footprint was also used adjust the scaling factors to the estimated time a particular area of the surface was sampled.

The results highlighted high sensitivity to both background determination method and footprint area, though could be tailored to have reasonable agreement between measurement and NAEI. Section 5.5 discusses improvements that could be made to the current methods and how other methods of inventory assessment may be more suited to targets as large as Greater

London.

5.1 Measurement Platform

The FAAM aircraft is a BAE-146 is an airborne measurement platform. The aircraft can operate between ~30 - 9000 m and carries an instrument payload comprising a range of meteorology and chemistry instrumentation. Although there is some variation of payload with time, a core range of instruments are usually present, which are described in detail by Harris et al [138]. For this work, the key data was obtained from a Air Quality Design NO and NO_2 analyser, similar to that described in section 2.1 and deployed in chapters 3 and 4, however this version of the instrument operates at 1 Hz rather than 5 Hz.

5.2 Flight Summaries

All three of the flights used for this study consist of a lap around London and the South East of England, with stacked North-South runs at the mouth of the Thames Estuary, forming a curtain of measurements. The prevailing wind on each day was westerly, allowing the London plume to be captured during the stacked runs. There were some differences in the number and vertical spacing of transects in the curtain due to the conditions on the specific day, but the aim was to have a representative spread of measurements from near the sea surface to the top of the boundary layer. For this analysis the flights were split into their stacked runs, referred to as the kriged plane, and an upwind leg used in background determination. A brief summary of the flights is provided in table 5.1, the flight tracks are mapped in figure 5.1 and the data used to create the kriged planes are summarised in figures 5.2 - 5.4.

B948's stack consisted of 9 level runs at 150, 200, 300, 350, 450, 575,800, 950 and 1550 m, and one profile between 900 and 1550m. The 1550 m run contains limited NO_x data but is above the boundary layer (figure 5.2-C), so was included to aide with background determination. Due to the number of runs available on this flight, some of those that deviated from the plane were able to be removed, resulting in the 5 runs and 1 profile used overall. C016's stack consisted of 5 level runs at 100, 200, 350, 600 and 800 m (figure 5.3-C). C025's stack consisted of 6 runs, 5 level at 100, 150, 200, 300 and 550 m and one run beginning at 250 m and climbing in 3 steps to 400 m (figure 5.4-C). Although some runs deviated from the plane in these latter two flights, due to the more limited data available they were not removed.

Table 5.1: Summary of flights. Flights were a part of the following campaigns; B948 – Greenhouse gAs and Uk Global Emissions (GAUGE), C016 - School and Training on Aircraft New Techniques for Atmospheric Composition Observation(STANCO), C025 - Effect of Megacities on the Transport and Transformation of Pollutants on the Regional to Global Scales (EMeRGe)

Flight	Date	Range	Summary	Time	Mean	Std. Dev.
B948	2016-03-04	Full Flight	Start	08:55	-	-
			End	14:10	-	-
			Wind Speed	-	7	2.54
			Wind Direction	-	262	44.9
		Upwind Leg	Start	09:16	-	-
			End	09:42	-	-
			Wind Speed	-	9.51	3.06
			Wind Direction	-	281	64.4
		Kriged Plane	Start	10:58	-	-
			End	13:34	-	-
			Wind Speed	-	6.78	2.46
			Wind Direction	-	254	57.6
C016	2017-07-03	Full Flight	Start	11:02	-	-
			End	14:15	-	-
			Wind Speed	-	8.8	2.36
			Wind Direction	-	259	33.8
		Upwind Leg	Start	13:53	-	-
			End	14:03	-	-
			Wind Speed	-	7.17	1.02
			Wind Direction	-	265	35.9
		Kriged Plane	Start	11:43	-	-
			End	13:16	-	-
			Wind Speed	-	8.15	1.98
			Wind Direction	-	246	35.6
C025	2017-07-20	Full Flight	Start	12:29	-	-
			End	16:31	-	-
			Wind Speed	-	11.9	2.4
			Wind Direction	-	265	29
		Upwind Leg	Start	12:36	-	-
			End	12:57	-	-
			Wind Speed	-	10.6	1.89
			Wind Direction	-	267	56.8
		Kriged Plane	Start	13:32	-	-
			End	15:53	-	-
			Wind Speed	-	12.5	2.57
			Wind Direction	-	269	32.9

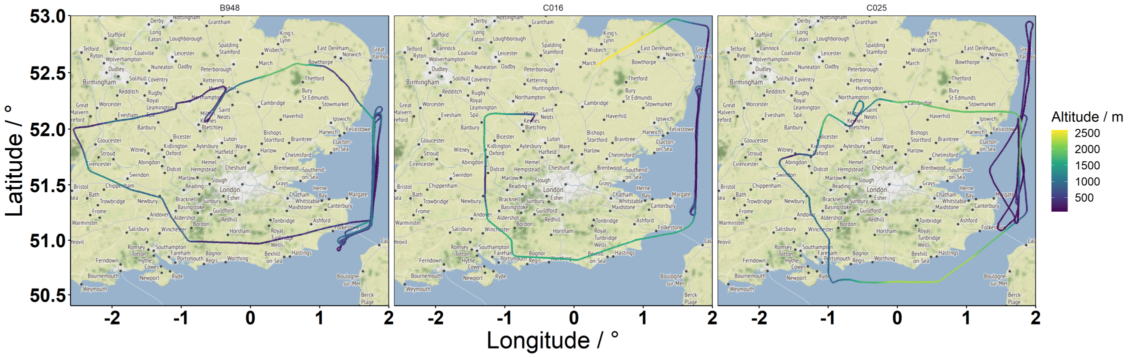

Figure 5.1: Flight tracks, left to right: B948, C016, C025

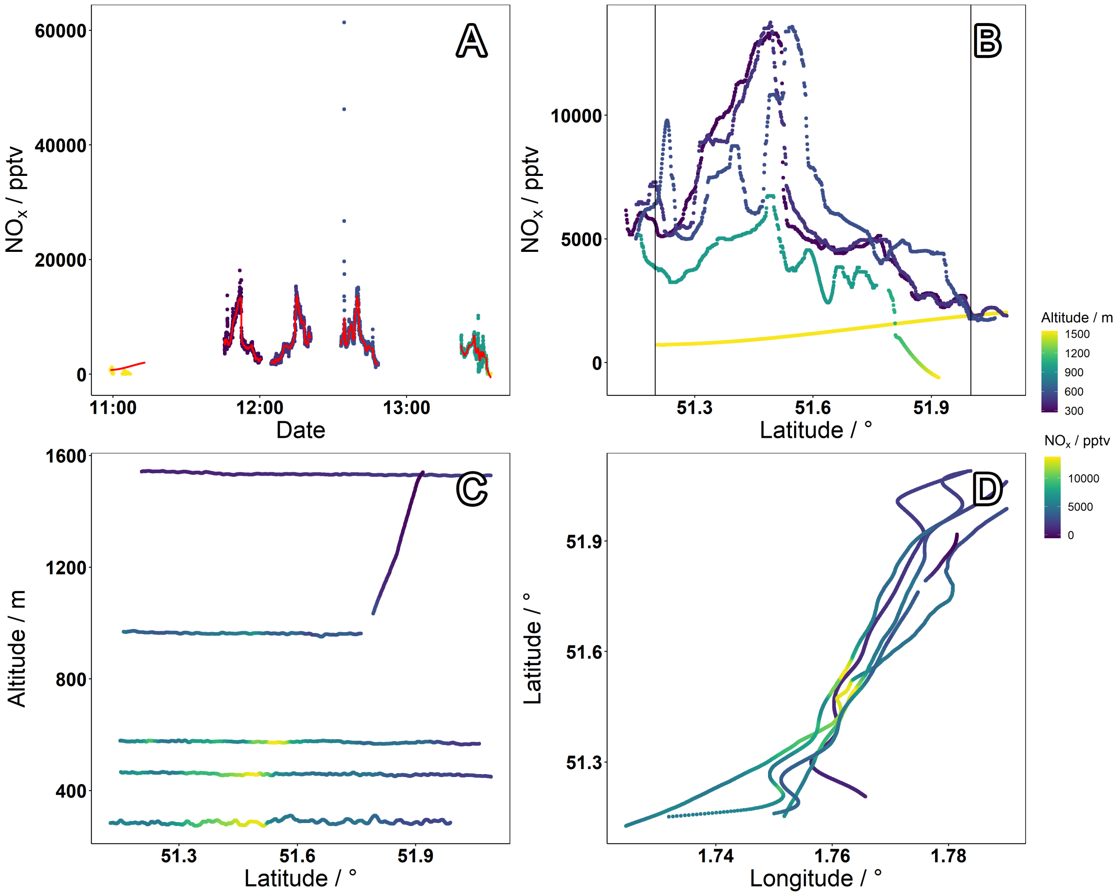

Figure 5.2: Summary of NO_x data from flight B948 used for mass balance calculations. A - NO_x concentration measured down wind of London. Points show raw data coloured by altitude and trace shows 31 s rolling median used to remove spikes. B - Rolling median NO_x concentration by latitude, coloured by altitude, showing that the plumes align in space. Vertical bars mark the "in-plume" areas for background determination (see section 5.4.2). C - Altitude/latitude positional data coloured by NO_x concentration. This is the plane used for kriging. D - Latitude/longitude positional data coloured by NO_x

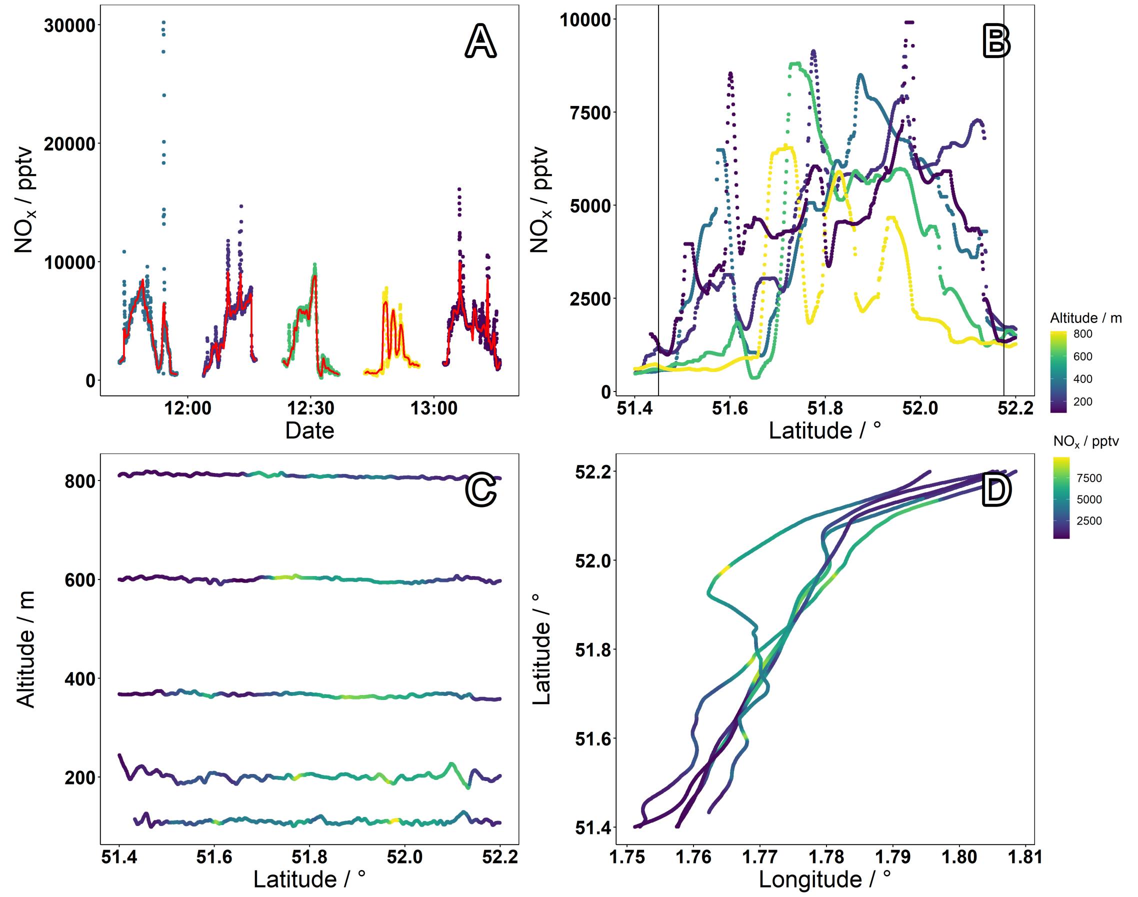

Figure 5.3: Summary of NO_x data from flight C016 used for mass balance calculations. A - NO_x concentration measured down wind of London. Points show raw data coloured by altitude and trace shows 31 s rolling median used to remove spikes. B - Rolling median NO_x concentration by latitude, coloured by altitude, showing that the plumes align in space. Vertical bars mark the "in-plume" areas for background determination (see section 5.4.2). C - Altitude/latitude positional data coloured by NO_x concentration. This is the plane used for kriging. D - Latitude/longitude positional data coloured by NO_x

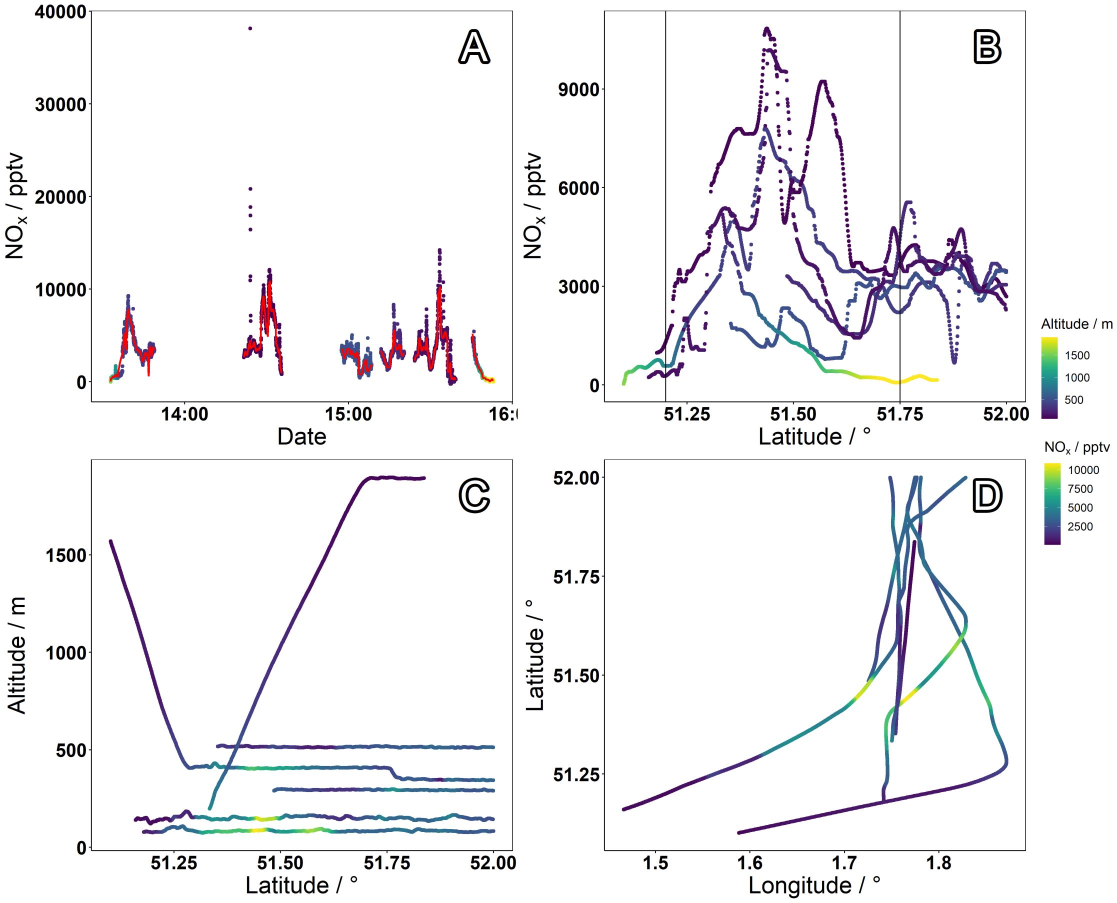

Figure 5.4: Summary of NO_x data from flight C025 used for mass balance calculations. A - NO_x concentration measured down wind of London. Points show raw data coloured by altitude and trace shows 31 s rolling median used to remove spikes. B - Rolling median NO_x concentration by latitude, coloured by altitude, showing that the plumes align in space. C - Altitude/latitude positional data coloured by NO_x concentration. Vertical bars mark the "in-plume" areas for background determination (see section 5.4.2). This is the plane used for kriging. D - Latitude/longitude positional data coloured by NO_x

5.3 Mass Balance Method

The mass balance method applied in the chapter refers to those used by several previous studies, and is described by equation 5.1 [139–143]. Here, S_{ij} is a concentration plane downwind of an emissions source and S_0 represents the background concentration. $(S_{ij} - S_0)$ then refers to the enhancement between these planes. $U_{\perp ij}$ is plane of perpendicular wind speed, allowing for the calculation of a flux across each grid cell. These planes are formed from sparse measurement data via kriging interpolation discussed in section 5.3.2. Vertical $(0 - z)$ and horizontal $(A - B)$ integration of the resulting plane provides a flux through the plane in mg s^{-1}. S_0 can be determined by measurements made upwind of the emissions source, above the boundary layer or from the edges of S_{ij} outside of the plume. Depending on available measurements S_0 either be a constant value or a plane of equal size to S_{ij}. When the emission source is distinct from it's surroundings, this flux can be attributed to it more readily (e.g. the use of forward trajectory models from oil rigs to confirm intersection with flight paths [144]).However, in the case of more complex terrain the area from which the measured emission originates must be defined. In this study backwards dispersion modelling was used to define this region, and is discussed in detail in section 5.4.2. An overview of the steps in this methods are shown in figure 5.5

$$Flux = \iint_{0A}^{zB} (S_{ij} - S_0) \cdot U_{\perp ij} \, dx \, dz \tag{5.1}$$

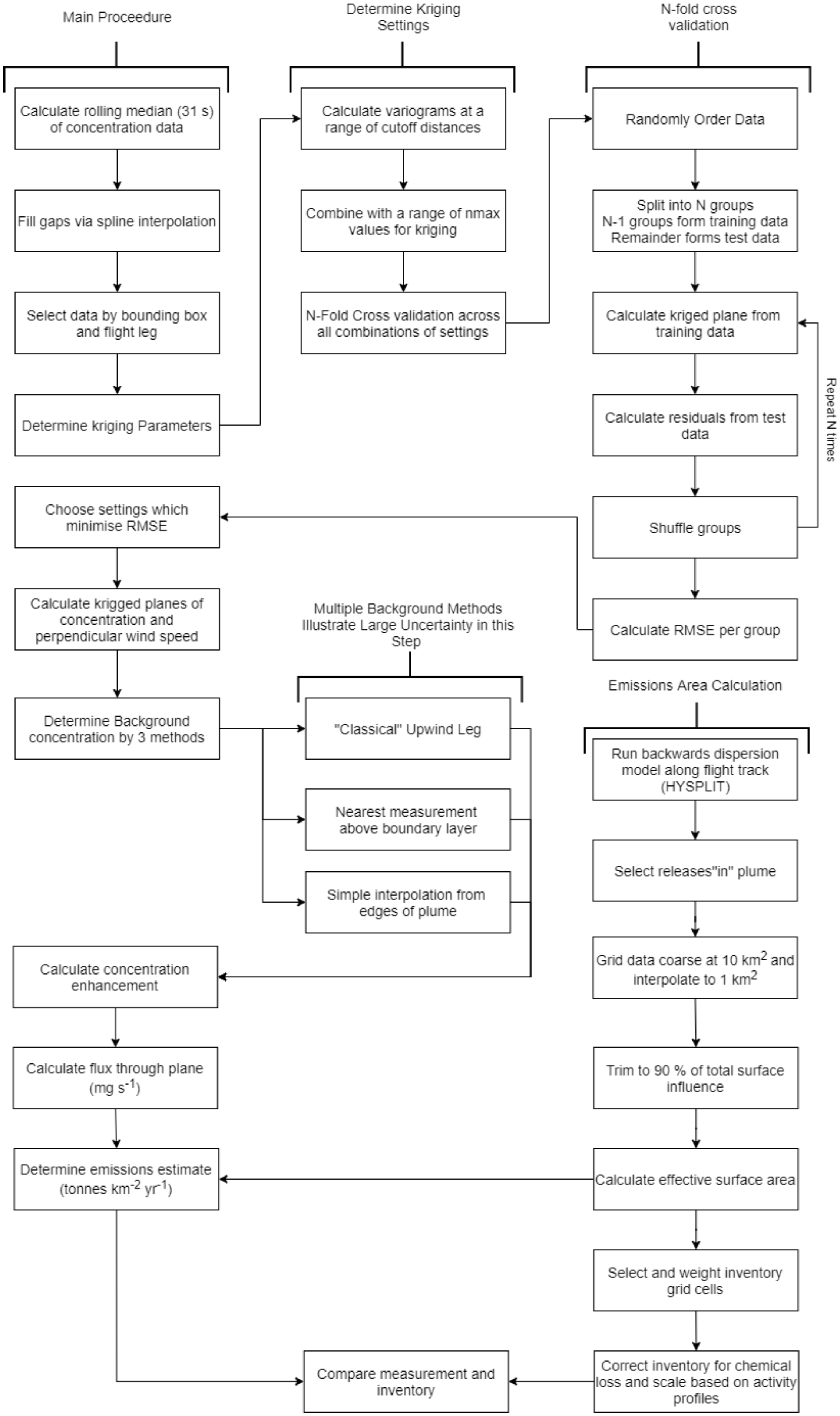

Figure 5.5: Mass balance method workflow

5.3.1 Data Pre-processing

To prepare the flight data for kriging the data underwent several pre-processing steps. Firstly the region of interest was selected. The segments of the flight downwind of London were selected, and the plume can be seen aligned by latitude in panel B of figures 5.2-5.4. Spikes were removed from the data as these can cause problems during variogram fitting, as these data vary a significantly different rate than the rest of the data, while the area they cover is small enough to have minimal impact on the final emission estimate. A spline interpolation was then run to produce a continuous data set per flight leg. The result of this process is shown by the red trace in panel A of the flight summary figures. NO_x mixing ratios were converted to mass volumes using the measured temperature and pressure at each point so that the final result of the mass balance calculation becomes mg s^{-1}.

5.3.2 Kriging

A plane of pollutant concentration is required by equation 5.1 and it is not feasible to make sufficient measurements that do not require gap filling in some capacity. Kriging interpolation has been regularly applied to produce the planes required for mass balance, and has also been used in this study. The kriging method is well suited for this application as it describes variability at differing length scales and as such does not require the plume to be "well mixed" up to the boundary layer. Kitanidis 1997 [145] provides a very detailed explanation of the workings of the kriging method, but in summary the method consists of the following steps:

— Re-scale distances - a assumption of kriging is that the data is stationary with respect to distance, i.e that variability is similar over similar length scales in all directions. For measurements of the atmosphere, there is generally greater variability in the vertical direction than over the same distance in the horizontal. In the case of the flights in this work, transects covered ~30 km in the latitudinal direction, but were spaced over 1-2 km vertically. To correct for this, latitudinal directions are first normalised to the range of the altitude covered, and then manually perturbed to so a radial variogram did not show significantly more variability in one direction or the other. The normalised altitude:latitude ratio was adjusted to 2:1, 2:1 and 3:2 for B948, C016, C025 respectively.

— Fitting of theoretical variogram - The theoretical variogram is a function fit to the differences of data points with respect to their separation. These data points are the γ values, and are defined in equation 5.2. The value of γ for a point, y_0, is defined as half of the mean of the square of the difference from all surrounding points, y_{i+h}, at given separation distance, h. By fitting a function to values of γ calculated over a range of separation distances and points at differing locations, a theoretical variogram is produced, $\gamma(h)$.

$$\gamma(h)_{experimental} = \frac{1}{2N}\sum_{i}^{N}(y_0 - y_{i+h})^2 \tag{5.2}$$

— Predict value at unmeasured locations. The theoretical variogram models how much a value varies with separation in a given data set. Assuming that the data set is a representative sub sample of the system being measured, predictions can now be made at locations with no measurement data. Let z_0 be a location where no data has been measured then $\hat{z}_{i+h}$ is a collection of points at varying separations from z_0. The theoretical variogram function $\gamma(h)$ can be used to produced a vector of weightings with a sum total of 1, $\hat{w}$ for each of $\hat{z}_{i+h}$. Calculating the weighted average of these points (equation 5.3) provides the estimated value at z_0.

$$z_0 = \frac{1}{N}\sum_{i}^{N}(\hat{w} \cdot \hat{z}_{i+h}) \tag{5.3}$$

Many previous studies have used the MATLAB software EasyKrig to apply the kriging method to the data, however, in this work the calculations have been performed using the R package gstat [146–148]. This was chosen so that the resulting interpolation could be evaluated using automated cross-validation methods, working to minimise route mean square error (RMSE), which would not have been possible using the manual EasyKrig software. Necessarily, the quality criteria presented by Kitanidis (Q1 and Q2) are not used here, in favour of the results from the cross-validation procedure.

The general procedure outlined above provides two parameters that can be optimised in the cross-validation step: the variogram range (h from equation 5.2) and the total number of points used when calculating the unknown point (N from equation 5.3). gstat returns the theoretical variogram that has the best least squares fit to the experimental variogram, so this was not directly controlled but was impacted indirectly whilst tuning the range.

Five fold cross-validation was used, where the data order was first randomised and divided into 5 randomly sampled subsets, 4 of which considered training sets and the 5th the test set. For each training set kriging was performed onto a grid of resolution 40 x 40 (arbitrary units after distance rescaling distances). The RMSE was calculated from the test set, and the combination of settings that provided the lowest RMSE were used for the final kriging. The range of the variogram was adjusted between 100 and a third the horizontal distance for the data (arb. unit), in 100 arb. unit increments. The number of points used when calculating the kriged value ranged between 50 and 400 in 50 point increments. Table 5.2 lists the results of this cross-validation.

Table 5.2: Results of cross-validation of kriging settings for flights B948, C016 and C025

Flight	Range / arb. units	nmax	RMSE / %
B948	300	50	0.9
C016	100	200	3.6
C025	200	350	4.8

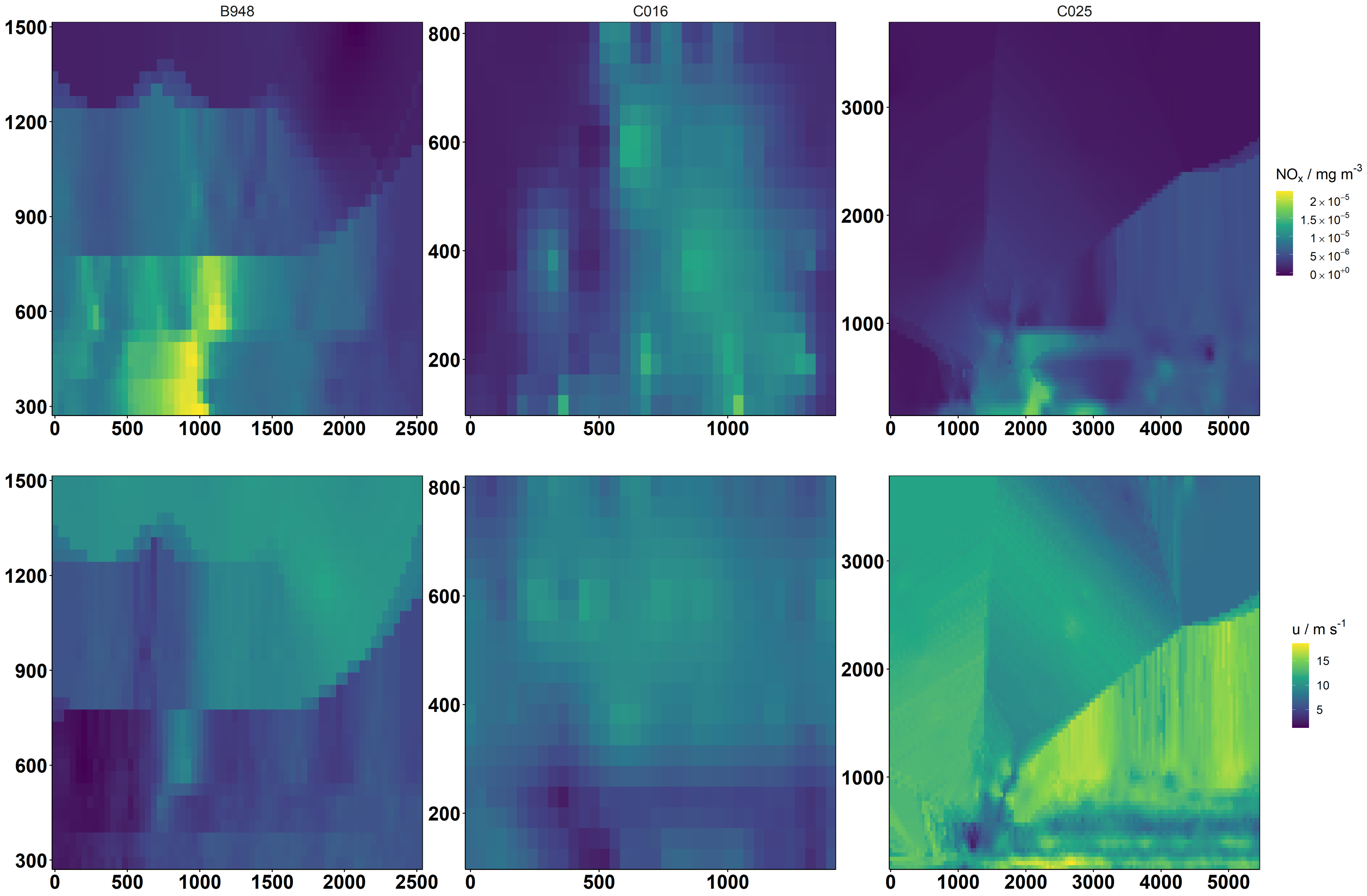

Figure 5.6: Kriged planes of NO$_x$ (top) and wind speed (bottom) for the three flights (left to right B948, C016, C025)

5.3.3 Determining the Background

The background concentration S_0, has been characterised by three methods:

- Average of concentrations measured upwind of plume. For small targets, flight plans can be designed such that both upwind and downwind planes can be measured. However, the time taken to fly around Greater London makes this infeasible within the FAAM aircraft's 4-5 hour range. In the case of these flights one single transect was measured upwind, and the average concentration measured here can be used as a background estimate. This estimate requires that these upwind measurements are representative of the background downwind, though, with it taking longer than an hour to fly between the upwind and downwind measurement areas changes in boundary layer height can mean that this is not the case. In figure 3.8 it was shown that the average boundary layer height in central London does not reach maximum until the early afternoon, so although flights were planned to minimise the effects of a changing boundary layer, these would not have been entirely mitigated.

- Average of the nearest measurements above the boundary layer. By definition the boundary layer is the highest point at which the atmosphere is directly influenced by the surface, often characterised by a temperature inversion "capping" emission from below. Mixing across this boundary is usually slow, so measurements from above could be considered a good background measurement as they are disjunct from the surface. This method may be more relevant than the upwind concentrations for distinct sources but is challenging due to the need for above boundary layer measurements, near the plume in flight. Identifying suitable data was possible for B948 and C025, but was not possible for C016, due to vertical profiles that in fact pass through the boundary layer being too temporally separated from the measurement of the plume, leading to similar issues as those discussed for the upwind background method. Furthermore, as movement in free tropospheric air is mainly driven by advection, so could lead to a much more aged air mass being sampled, resulting in a wholly unrepresentative value for the background. The data that was selected was above the major enhancement in NO_x, but did not necessarily coincide with changes in potential temperature. Although not strictly following the "above boundary layer" name for this method, it may be more representative that actual free tropospheric air due to the aforementioned ageing. Figure 5.7 shows NO_x and potential temperature profiles near the stacked runs for each flight along with horizontal lines for the selected boundary layer height for each flight.

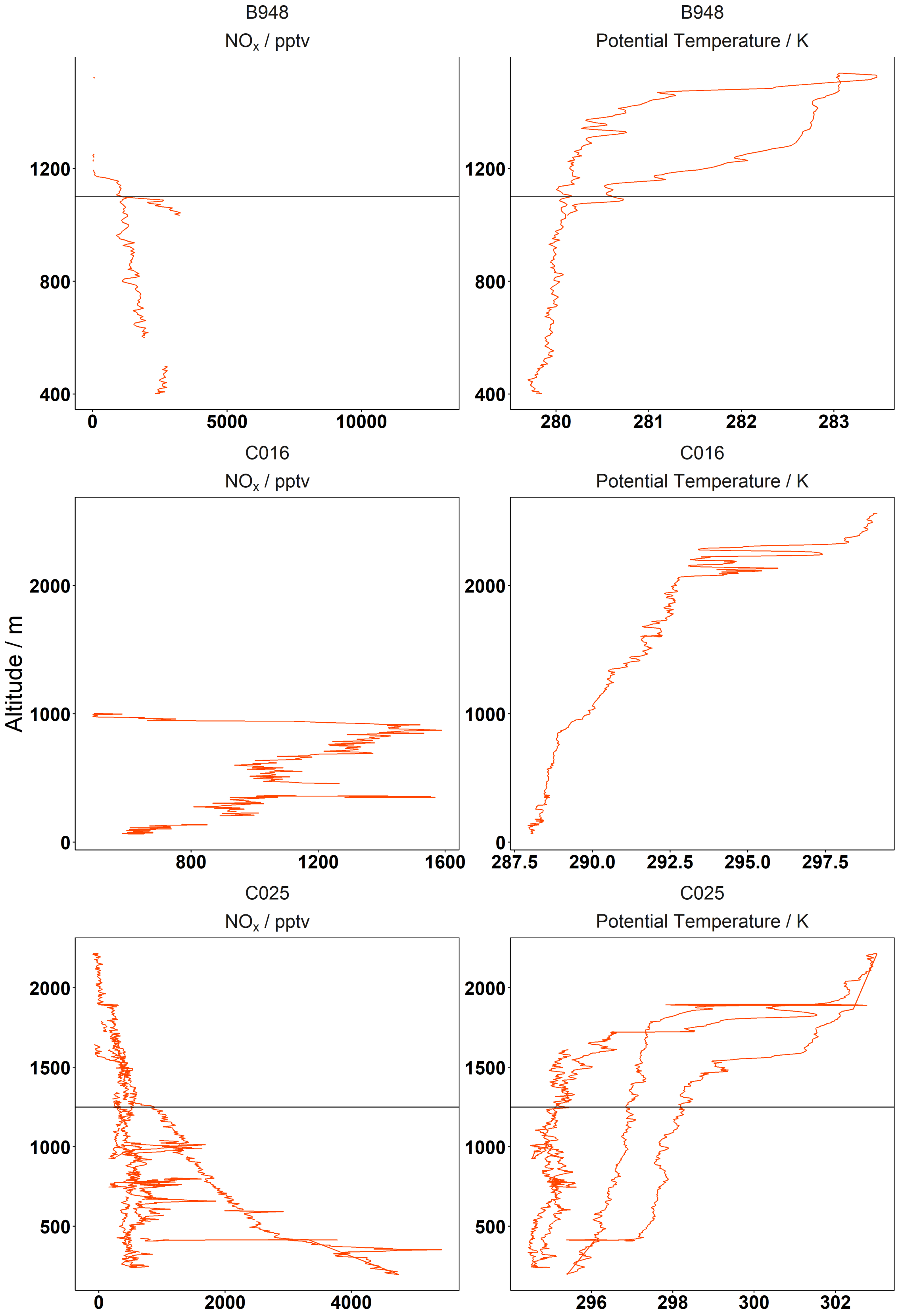

Figure 5.7: Vertical profiles of NO$_x$ (left) and potential temperature (K) for the three flight (top to bottom B948, C016, C025). Horizontal lines show heights used to determine "above boundary layer" background for flights B948 and C025. Due to lack of NO$_x$ measurements above 1000 m in C016, this method was not applied to this flight.

— Interpolate values measured at the edges of the plume. Using the values from the edges of the plume, outside the vertical bars marked on figures 5.2 - 5.4-B, focuses the measurement on the target by incorporating edge sources into the background measurement, and the measurements are made co-temporally with the in-plume measurements. These values could simply be averaged to provide one single value, as the other methods have done, but this neglects this methods increased measurement density. By linearly interpolating between edge measurements on each transect, a background data set can be generated and subsequently kriged using the same methods as the plume itself, similar to the implementation by Turnbull et al. 2019 and Ashworth et al. 2020 [142, 149]. This allows for the background to be spatially variant as it is described across the same grid as S_{ij}. The amount of interpolation in this method does introduce some increased uncertainties, but has the benefit that the values are much more spatially and temporally related to the in-plume measurements. The background planes that result from this method are shown in figure 5.8.

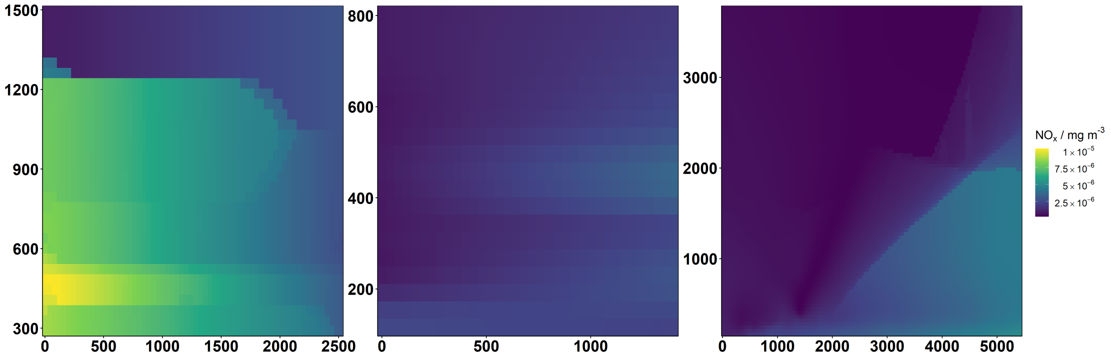

Figure 5.8: Kriged background NO$_x$ concentrations, based upon linearly interpolated edge of plume measurements for each flight (left to right B948, C016, C025)

5.4 Calculated NO_x Emission from the Greater London Area

Table 5.3 shows the emissions calculated using the previously described mass balance method from each of the three flights. Each emission has had the background calculated in the three ways outlined in section 5.3.3. These primarily demonstrate the variability in results that can be obtained using this method. Firstly, as a flight only provides a small temporal "snapshot" of the emissions, real differences from changes in activity due to time of day, day of week or month of year are present.

Secondly, the exact surface area sampled is currently undefined, hence these emissions are presented in mg s^{-1}. Section 5.4.2 describes the methods that have been used to estimate the source area, allowing comparison per unit area. This source area was also used to use correct for temporal variations somewhat during the comparison with the NAEI (section 5.4.4). Thirdly, the measured air mass has aged several hours since emission, so corrections for NO_2 loss to HNO_3 are calculated in section 5.4.3.

Finally, the selection of background determination method was demonstrated to introduce enormous variability into the final emissions values (the edge of plume versus upwind methods in flight B948 reduced the emission by 6 fold). These background methods can be sorted into an order of precedence for which intuitively should be closer to the "true" background based upon their descriptions in section 5.3.3, namely edge of plume > above boundary layer » upwind. However, as the results presented in table 5.4 show, this is not necessarily the case and it is not facile to choose which background method is the most representative.

5.4.1 Uncertainty Estimation

The uncertainty in the mass balance emissions estimate is a combination of the uncertainty in the NO_x concentration and the uncertainty in the kriged planes. The uncertainty in NO_x concentration was calculated as described in section 2.1.3, and for the instrument used to collect these data was 3 % in NO, and 4.3 % in NO_2, providing a total uncertainty in NO_x of 5.2 %.

For the kriged planes, while the RMSE calculated in table 5.2 was a metric of how well the interpolation compared with a testing set, uncertainty increases with distance from measured points. The gstat package provides a uncertainty for each grid cell of the kriged plane, examples of these are shown in figure 5.9. The relative uncertainty in the NO_x plane, wind speed plane and background was calculated as equation 5.4, where E is the calculated emission rate and $\sigma()$ represents the uncertainty in a given term.

$$\frac{\sigma(E)}{E} = \sqrt{\sum_{ij}\left(\left(\frac{\sigma(S_{ij})}{S_{ij}}\right)^2 + \left(\frac{\sigma(U_{ij})}{U_{ij}}\right)^2\right) + \left(\frac{\sigma(S_0)}{S_0}\right)^2} \tag{5.4}$$

This was then combined in quadrature with the NO_x measurement uncertainty, before being multiplied by the calculated emission to provide a combined absolute uncertainty, $\sigma(E)'$ (equation 5.5).

$$\sigma(E)' = \sqrt{\left(\frac{\sigma(E)}{E}\right)^2 + \left(\sigma(NO_x)\right)^2} \times E \tag{5.5}$$

The resultant uncertainty is quoted alongside the emissions estimate in table 5.3.

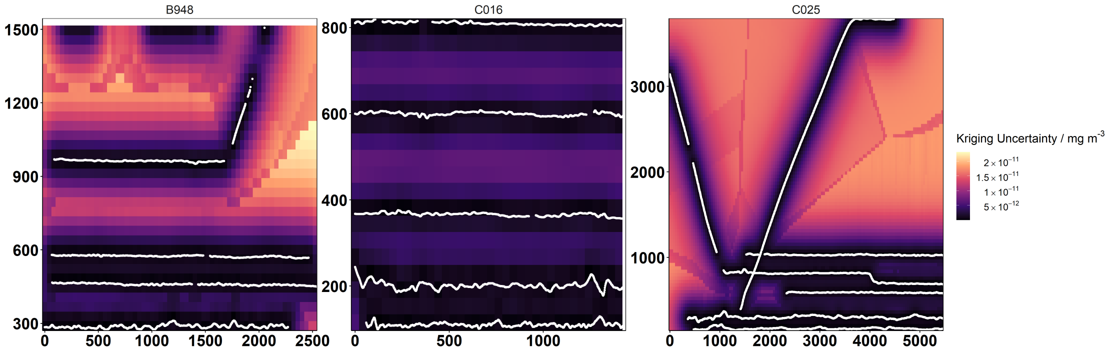

Figure 5.9: Uncertainty in kriged NO_x concentrations for the three flights, left to right B948, C016, C025. White trace shows location of measured data.

Table 5.3: NO_x emissions measured during flights B948, C016 and C025. A value is given for each of the methods of determining the background and the associated combined uncertainty from interpolation, background determination and NO_x measurement. *Above Boundary Layer

	NO_x Emission / mg s^{-1}								
Flight	Upwind	σ(E)	%	ABL*	σ(E)	%	Edge of Plume	σ(E)	%
B948	165000	± 8680	5.26	86800	± 4610	5.31	26300	± 1760	6.68
C016	140000	± 7320	5.22	-	-	-	115000	± 6210	5.42
C025	32500	± 2340	7.19	40800	± 2790	6.84	26300	± 2340	8.92

5.4.2 Estimating Source Area

The emission area associated with the mass balance calculation is crucial for the comparison with emission inventories. A coarse concentration footprint was generated for this analysis using Hybrid Single Particle Lagrangian Integrated Trajectory Model (HYSPLIT) backwards dispersion models, facilitated by the **SplitR** R package [150]. These models consisted of zero hour releases of 400 particles spaced 60 seconds apart along the flight track, run backwards in time for 12 hours, using GDAS 1° meteorology fields. The ensemble of these released was filtered on several criteria to form the footprint, resulting in a product not dissimilar to the footprints used in section 3.2, but on a much larger spatial scale and an additional temporal component.

1. An ”in plume” region was defined along the flight tracks, shown by the vertical bars in figures 5.2, 5.3 and 5.4. Releases that occurred outside of this area were removed as the surface influence they represent did not correspond to the enhancement.

2. A height of 100 m was defined as a height of surface connectivity. This was chosen to match the height Pitt et al. used as their definition for their time integrated dispersion model method. In this study the location where a particle first dropped below this height was recorded (in terms of the backwards model, in real time terms this is the last location a particle moved above 100 m), and all remaining particles or the same particles at different times, were removed.

3. This resulting particle distribution was summarised on a 1 km^2 grid (matching the resolution of the NAEI) calculating the sum total and average age of particles in a given grid cell. The the total of all the cells was normalised to 1, weighting each grid cell to its contribution to the measured emission. The age of each particle is release specific so this takes into account the 1 - 2.5 hour flight time.

4. Finally, cells were summed in order of descending contribution, once 90 % of the total contribution to emission was reached, the remaining cells were discarded. This crucially provides a spatial limit to the area of influence rather than from the legs used for background measurements upwind of the target.

At this point this method of footprint determination encountered an issue. Gridding the data to as fine a resolution as 1 x 1 km left a very small number of particles in each cell limiting the resolution of the grid cell contribution. Figure 5.10 demonstrates this moving across the rows right to left, decreasing the resolution from 10 to 1 km^2; the grid cell values have increasing stratification with decreasing cell resolution. The consequence of this being that the footprint is insensitive to filtering by percentage contribution. The number displayed on each panel shows the number of grid cells in each regime, and moving through the columns top to bottom shows a decreasing footprint contribution threshold, from 100 to 60 %. The amount of cells in the 1 km^2 footprint does not change, as none reach even the 60 % contribution threshold, whereas at 5 km^2 and above are sensitive from 100 to 90 % onwards. This sensitivity is required so that the total emissions area responds to filtering of the footprint and impacts both the inventory assessment and the denominator of the measured emissions. Moving to more coarse gridding solves the stratification problem, but the larger the grid cells, the less regularly sampled the inventory. Both issues were overcome simultaneously by first generating a 10 km^2 resolution footprint, as described in steps 1 - 3 above, and then using kriging interpolation once again to increase the grid resolution to 1 km^2. The same method was applied to the air mass age facet of the footprint, with the exception of simple inverse distance weighted interpolation used in place of kriging interpolation, as this was already highly ordered and decreased computation expense significantly. The resulting footprints for each flight at 90 % contribution are shown in figure 5.11.

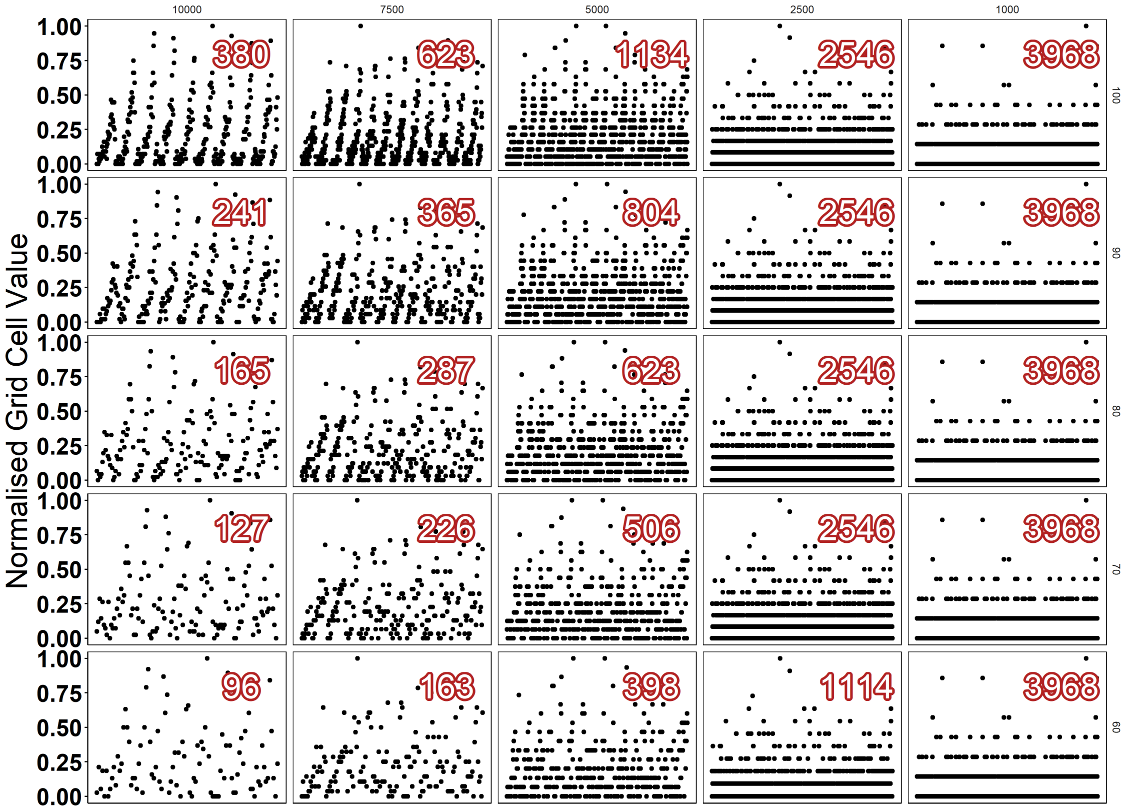

Figure 5.10: Normalised contribution to a footprint grid cell plotted in an arbitrary order. Left to right decreased grid cell size from 10000 m^2 to 1000 m^2. Top to bottom decreases percentage to total footprint contribution from 100 % to 60 %. Red number shows the total number of grid cells in a given combination of resolution and threshold. This figure illustrates the stratification of grid cell values at higher resolution, and subsequent insensitivity to footprint threshold filtering.

5.4.3 NO$_2$ Loss

Unlike the emissions measurements described in chapter 3 the air masses measured during these flights are hours old rather than minutes. NO$_2$ loss to HNO$_3$ is significant on this timescale and must somehow be accounted for. The footprint estimation provides average air mass age by grid cell, however, this cannot be easily translated to the measured emission estimate. This is because each concentration measurement is influenced by an aggregate of several grid cells. Using the modelled footprint a weighted average could be calculated for the

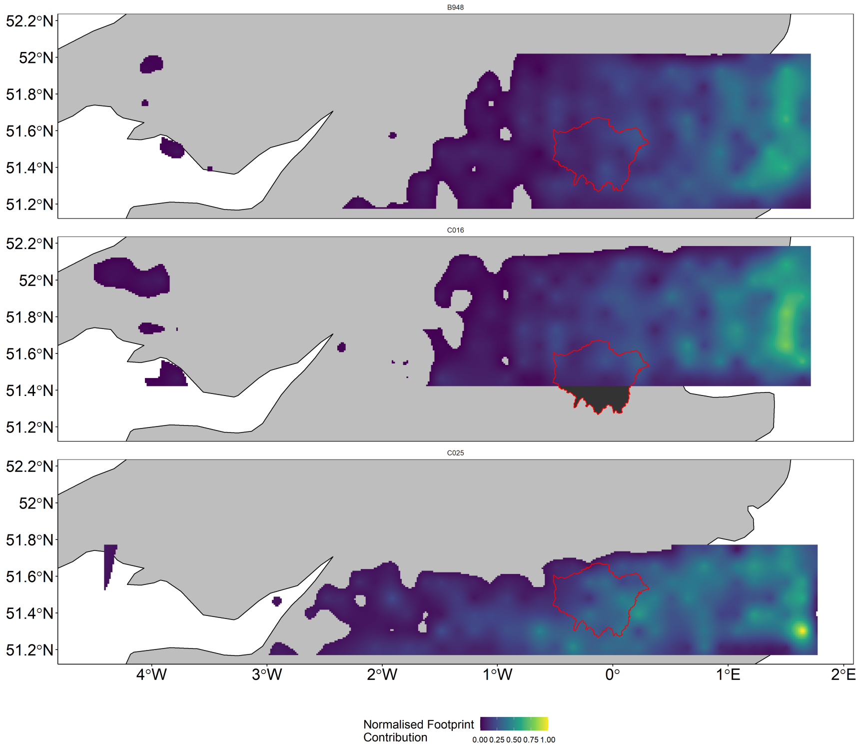

Figure 5.11: Footprints for each flight (top to bottom B948, C016, C025) at 90 % contribution threshold. Colour shows spatial distribution of footprint contribution.

concentration measurements, and the emissions estimate recalculated. Though, as the flights are not directly inter-comparable and must be linked via the inventory already, the more straight forward approach is to apply this correction to the already gridded inventory emission estimate. The resulting measured emission to inventory estimate is then comparable across flights (when fully corrected and scaled).

For this purpose the NO_2:NO_x ratio was calculated along the flight tracks, and carried backwards with the dispersion model and the average calculated per grid cell. Although the emitted NO_x will primarily be as NO, it will reach steady state with NO_2 on shorter timescales than the time taken for transport to the receptor. The loss factor calculated from equation 3.1 (as defined in section 3.1.4) was only applied to a proportion of the inventory emission relative to the average proportion of NO_2 per grid cell.

$$\frac{[NO_2]}{[NO_2]_0} = e^{-k_{[OH]} \cdot (\frac{T}{300})^{-4.5} \cdot [M] \cdot [OH] \cdot t} \tag{3.1}$$

The NO_x loss term for this method will inherently underestimate the proportion of missing NO_x , as only lost to HNO_3 is considered. Over a period of hours, conversion of NO_x to PAN (R 1.13) will be appreciable, as the equilibrium will favour its formation as air temperatures decrease away from the urban area. Additionally, some heterogeneous loss routes for NO_2 (e.g, R 5.24) may be important on these timescales, especially over the ocean where there is likely larger amounts of water vapour present [151]. In future work it may be prudent to consider further NO_x chemistry via an appropriate chemical model, however, whilst other uncertainties are still large, the simple treatment via HNO_3 loss is sufficient.

$$2\,NO_2(g) + H_2O\,(ads) \longrightarrow HONO\,(g) + HNO_3(ads) \tag{R 5.24}$$

5.4.4 Scaling of and Comparison with the NAEI

Corrections thus far have worked to remove variability in the measured emissions due to source area and chemical loss. The measured emissions from the flights cannot be directly compared with one another, but their relation to the NAEI's emission estimates can. Using the footprint model developed in section 5.4.2, NAEI 2017 values for all sectors were extracted at the centre point of each footprint grid cell, and using the average air mass age within each grid cell to the nearest hour scaled to the correct hour of day, relative to the average time whilst measuring the kriging plane. For example B948's kriged plane was measured between 10:58 and 13:34 - averaged to the nearest hour as 12:00, so grid cells have their scaling factor determined as 12:00 minus average air mass age. From the date of the flight day of week and month of year scaling factors were applied. All scaling factors are the same as those used in section 3.3.2. This resulted in each grid cell of the NAEI being scaled for temporal activity by sector, the relative NO_2 proportion by NO_2 loss due to air mass age and the total by footprint contribution based on the dispersion modelling. The sum over all the resulting grid cells provided the total estimated emission in tonnes km^{-2} yr^{-1}. Table 5.4 shows these values compared with the measured emissions in the same units.

Table 5.4: NO$_x$ emissions measured during flights B948, C016 and C025 for each background determination method, compared with the estimated emission from the NAEI, at 90 and 80 % footprint contribution thresholds. Measured/NAEI ratio is calculated from the edge of plume calculation.

			NO$_x$ Emission / tonnes km^{-2} yr^{-1}				
Flight	Threshold / %	Source Area / km^2	Upwind	Above Boundary Layer	Edge of Plume	NAEI	Measured/NAEI
B948	90	5680	0.916	0.482	0.146	3.080	0.047
	80	4070	1.28	0.673	0.204	2.910	0.070
	70	3120	1.67	0.879	0.266	2.400	0.111
	60	2540	2.05	1.080	0.326	1.820	0.179
	50	2010	2.58	1.360	0.412	1.360	0.303
	40	1580	3.28	1.730	0.523	0.870	0.601
	30	1140	4.56	2.400	0.726	0.575	1.260
C016	90	4920	0.900	-	0.736	1.290	0.568
	80	3540	1.250	-	1.020	1.230	0.831
	70	2800	1.580	-	1.290	1.020	1.270
	60	2180	2.030	-	1.660	0.813	2.040
	50	1760	2.510	-	2.050	0.630	3.260
	40	1390	3.180	-	2.600	0.483	5.380
	30	885	5.000	-	4.090	0.370	11.000
C025	90	3500	0.293	0.367	0.237	2.680	0.088
	80	2580	0.397	0.498	0.321	2.560	0.125
	70	1850	0.555	0.695	0.448	2.280	0.197
	60	1200	0.856	1.070	0.692	1.940	0.356
	50	801	1.28	1.600	1.030	1.550	0.667
	40	569	1.8	2.260	1.460	1.170	1.250
	30	394	2.61	3.270	2.110	0.816	2.580

5.5 Discussion and Future Work

The results summarised in table 5.4 show that the methods developed throughout this chapter are not yet enough to provide a conclusive bulk emissions estimate of NO_x from Greater London and surrounding areas. Estimation of the background concentrations has shown to introduce wide uncertainty ranges into the final results, much more than was anticipated at the outset of this analysis. Previous work that has focused on longer lived gases noted the sensitivity to the background, but due its shorter atmospheric lifetime, the calculated enhancement for NO_x was expected to be less responsive to changes in the background, as the in-plume concentration is several orders magnitude greater than the out of plume measurements. However, as the results in table 5.3 show, different methods of determining this background had large impacts on the calculated emission.

Different methods in some cases produced greater than 5 fold changes to the final emissions estimate and counter-intuitively more developed background determination methods increased the disparity between measured and inventory emissions estimates at higher footprint thresholds, e.g flight B948's emission estimate decreases by ~2 times moving from upwind to above boundary layer backgrounds and ~6 from upwind to edge of plume. This was less pronounced in the other two flights with the background methods causing a change on the order of ~1.2 - 1.5 times. This may be due to B948's earlier flight time, making the upwind leg significantly more unrepresentative of the true background as the boundary layer was still developing, though there was still a 3 fold decrease from the above boundary layer to edge of plume cases.

From these results, no certainty can be drawn as to which of the background methods are closest the the *true* background. Conceptually however, a strong argument can be made for the edge of plume method as it is sampled both adjacent to and co-temporally with the plume. Furthermore, its definition bounds the dispersion modelling, directly separating the background concentrations from the enhancement caused by emissions in the footprint area. As such to examine the effect that the footprint model has on the final results, this background method was focused on.

The footprint model fills a precarious space in this analysis, as it intrinsic to both the measured emissions and those generated from the inventory. This is different to the eddy covariance (EC) measurements from the previous chapters, as EC provides emission in terms of unit area so the footprint only directly governs the inventory emissions. Here the measurement gains its per unit area from the footprint, so as this area increases, measured emissions decrease. This also increased the NAEI emissions due to more inland area being sampled, increasing the average per km^{-2} emission for the inventory. This would not be expected in every scenario this footprint is applied to, as it is highly dependant on the surface being sampled. To examine the impact of footprint size the percentage contribution threshold was varied between 90 and 30 %, as shown in the data in table 5.3 and the effect is plotted in figure 5.12. Although the NAEI was found to underestimate the NO_x in central London by a factor of 1.4 in chapter 3, this was expected to be due to local effects and the inventory for the Greater London and surrounding areas has been shown to agree more [90]. Considering this, table 5.5 shows the measured to NAEI ratios closest to 1 using the edge of plume background method selected from the range of footprint thresholds. From this an issue immediately arises; the best agreement for flights B948 and C025 require the footprint to be reduced to 30 and 40 % of its total contribution, but figure 5.12 shows that Greater London does not contribute to the NAEI emission at these thresholds. One reason for this may be that the contribution to the footprint is too heavily weighted near the location of dispersion release. In figure 5.11, the footprint maxima are found at the eastern edge, much of which corresponds to particles touching down within the first hour time-step of the dispersion model. While this may or may not be realistic, the reduction of footprint size by threshold inevitably leaves this area present in the footprint, reducing the inventory's emission until it is in line with the inflating measured emission (due to the diminished footprint area). A second reason follows from this, that the footprint is providing too large an area, and as such the area over which the measurement is being divided results in the emission being overly reduced at larger footprint sizes. Indeed, just averaging NAEI emissions from the Greater London area gives an emission of 23.6 tonnes km^{-2} yr^{-1}. Although this value would be diminished by averaging in the lower emissions area surrounding London, the measured emissions are vastly lower, the highest being 5.0 tonnes km^{-2} yr^{-1} from C016 using upwind background at 30 % footprint threshold. Thirdly, the simplistic treatment of NO_2 loss in this analysis could lead to the NAEI emissions value being too low - the correction was applied relative to the proportion of NO_2 in NO_x at the time of measurement. Most NO_x is emitted as NO and some time is taken to form NO_2 and reach equilibrium, though this would be expected to occur on time scales shorter than the transport from the ground to receptor for much of the measured NO_x. The cycling of NO and NO_2 in the steady state makes a greater portion of the NO_x available to be lost to HNO_3, so increasing the proportion of the NAEI that is corrected for NO_x loss should be considered. From these measurements alone what this proportion should be is hard to determine, and would require the use of chemical-transport models to determine more fully. These could provide concentrations at both the surface and at the receptor site, improving the loss terms used in weighting the inventory.

The footprint model could be improved wholesale using a dispersion model with a higher timer resolution, which can be achieved with HYSPLIT or a different model such as the Numerical Atmospheric dispersion Modelling Environment (NAME) use by Pitt et al. [141]. The HYSPLIT dispersion model data used here is limited, only outputting 1 hour time steps. As the air masses travel between the Greater London area and the receptor on the order of ~4-6 hour, ± 0.5 hour of uncertainty in particle location may translate to quite different weightings of the inventory even after re-gridding and interpolation.

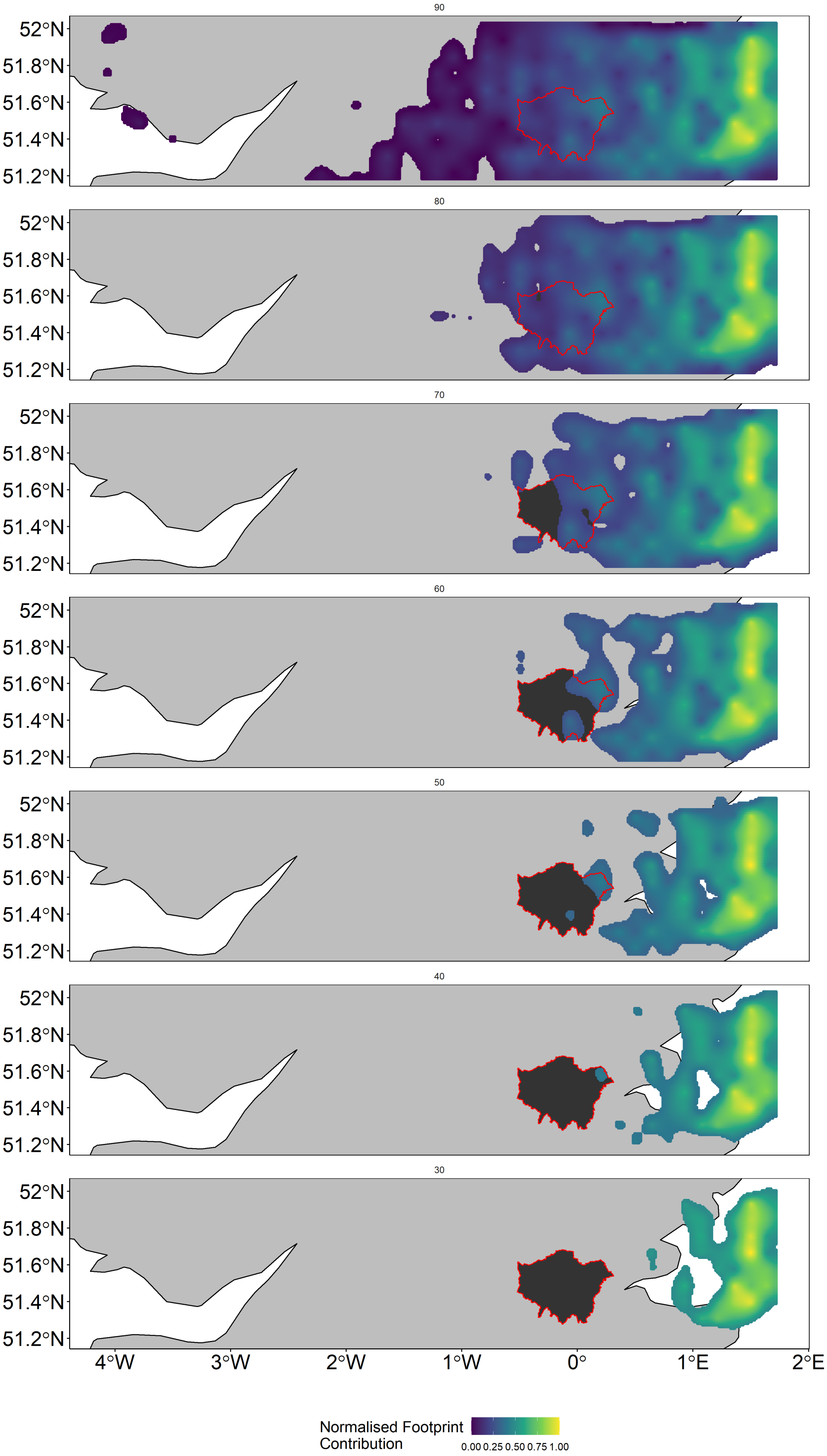

Figure 5.12: B948 footprint at decreasing footprint contribution thresholds from 90 (top) to 30 % bottom. Colour shows spatial distribution of footprint contribution.

Table 5.5: Combination of background determination methods and footprint thresholds that provide a Measured/NAEI ratio closest to 1 for each flight using the edge of plume background determination method.

		NO_x Emission / tonnes km^{-2} yr^{-1}		
Flight	Threshold %	Measured	NAEI	Measured/NAEI
B948	30	0.726	0.575	1.26
C016	70	1.29	1.02	1.27
C025	40	1.46	1.17	1.25

Following on from this, a flaw in the method is the large simplification of using the final point a particle rose above 100 m as a description of the emissions it is representative of. The particle (and the air mass it represents) will have travelled below this height for some time, and while locations closer to the location where it no longer was influenced by the surface will have a greater effect, it is in fact an aggregation over a much larger area than a 1 km^2 inventory grid cell. Through use of a dispersion model with greater temporal resolution a time integrated footprint contribution per particle could be calculated, which would provide more information about surface emissions influencing the air mass than the single points used in this model. This method could be implemented using similar techniques as found in Pitt et al, 2019 where time integrated surface interaction of a dispersion model with the NAEI was used to generate a concentration time series [141]. For this particle releases should be spaced evenly across the kriged concentration space unlike what has been presented both here and by Pitt el al., so the the kriged surface is equally represented by the dispersion model, rather than being linked by the physical aircraft sampling locations. Some development of this time integrated approach to footprint generation may also shift the footprint maxima to the east, as those particles that are rapidly rising from the surface within the first time-step would necessarily spend less time below the 100 m threshold and thus be down-weighted.

If experiments like this are repeated there are some ways that these result suggest flight design could be improved. First and foremost conversion to a multi-aircraft study would allow for co-temporal measurements of the upwind and downwind planes, improving the representativeness of this background method. This of course substantially increases the cost of these measurements and while desirable, may not be feasible, especially if it would reduce the frequency these studies could be conducted. For a complex source like London, who's emissions vary temporally, multiple measurements at differing times of day would also improve emissions estimates. In the absence of a second aircraft, using the edge of plume background method would allow for more of the flight to be focused measuring the downwind plume and if aircraft range allowed, multiple measurements of the same transects could be captured. If this were the case some ~hourly temporal variability may be able to be described using spatio-temporal kriging [152]. This could potentially be further extended into a campaign of flights, where multiple days were targeted to also reduce the need to use day of week scaling factors, possibly utilising the EC measurements from chapter 3 to group similar days (i.e Tuesday-Saturday and Sunday-Monday). It should be noted that if logistical and financial restraints are being omitted, airborne EC can provide highly spatially resolved measurements of emissions [90, 92] and could be extended with multiple flights to give some insight into temporal variability.

As discussed previously the issues posed from a reactive species may benefit from the use of a chemical-transport model. In addition to providing a better treatment of the chemistry, these models are driven by emissions inventories and as such can be used to evaluate their performance against measurement (assuming the chemistry is well described) [153]. This may ultimately prove to be a better alternative to the mass balance method when measuring large spatially complex targets. Pitt et al's dispersion model inversion is somewhat approaching this, as instead of transforming aircraft measurements into emissions estimates blending measurement and model, as has been done here, the inventory emission is transformed into concentrations directly comparable to measurement.

Overall this method is as yet unable to provide a definitive emissions estimate for NO_x emission from Greater London and surrounding areas, but has explored ongoing issues with the mass balance method and proposed improvements may allow for larger targets and reactive species to be more properly quantified.

Chapter 6

Summary and Future Work

The work detailed in this thesis aimed to develop and apply methods to quantify NO_x emission in the urban environment, and link these with local inventories. These measurements were mainly focused in London, UK (chapters 3 and 5) with chapter 4 extending this to include measurements in Dehli, India. Emissions were primarily measured using eddy covariance, and linked to inventories via a footprint model. This proved successful in both of the cities, providing a several month long data set in London, and two essentially contemporaneous time series in Delhi. The airborne measurements in chapter 5 applied a mass balance approach, and whilst it was unable to produce more quantitative results, it developed methods for working with reactive gases and began linking to emissions inventories through the use of particle dispersion modelling.

The use of these measurements to evaluate inventories is important as they inform policy, are used for international reporting of emissions and are an input of chemical-transport models. By necessity, these inventories cannot be constructed from measurements alone as entire countries or regions cannot be encapsulated by them. Instead they are constructed from emissions factors and activity data collected from a wide variety of sources and subsequently emissions measurements can evaluate whether the emissions modelled via this process are representative.

For the National Atmospheric Emissions Inventory in London, the measurements made in chapter 3 found an average underestimation of NO_x emission by the inventory of 1.4 ×, in keeping with previous measurements [91, 108]. Furthermore, these underestimations were found to be the greatest at the weekend, peaking at 3.3 × on Saturday afternoons. The comparison of the inventory by sector with the measured emission and traffic flow data suggests that the scaling factors used place too much emphasis on a decreasing emission on Saturdays compared with the rest of the week, which may well be due to differing activity in central London compared with the country average. Some of the more general underestimation was shown to also have a spatial component, with missing emission to the north-east and west of the tower. These regions align busy roads surrounding the tower, but the area to the north-east also indicates emissions from Euston station may not be fully represented. Measurements at the BT Tower resumed in 2020 with the aim of establishing the NO_x emissions measurements long-term. These data will be able to provide insight into the seasonal variation in NO_x emissions in the city and with more data surface mapping of emissions could be performed with greater temporal resolution i.e daily or hourly maps, averaged over several months, further improving understanding of the sources of discrepancy in the inventory and its scaling factors.

In Delhi, an inventory for the city had been produced by the India Meteorology Department and provided to the DelhiFlux project for evaluation and improvement. The measurements made in chapter 4 gave diurnal profiles at two locations in the city: Indira Gandhi Delhi Technical University for Women (IGDTUW) and the India Meteorology Department (IMD). The former was on the edge of Old Delhi surrounded by very congested roads, and the latter more central in city, but surrounded by larger compounds, wider (less congested) roads and more green space. The NO_x emissions followed what would be expected from these descriptions with 4 - 5 × lower emissions at IMD than IGDTUW. Despite this, similar concentrations were measured at both locations, potentially suggesting that emissions control policies implemented at IGDTUW would have greater impact on the cities overall air quality than at IMD. The inventory was found to greatly overestimate the emissions in its original form, and after some work within the project to correct the transport layer, still overestimated by 2 - 3 ×, however, the inventory did capture the relative differences between the sites lending support to the spatial mapping of emissions, if not their magnitude. The same scaling factors were applied to this inventory as were used in chapter 3, which may account for some of the discrepancy, especially as seasonal factors derived for Europe are unlikely to be representative of India. Local scaling factors would improve this comparison greatly.

Both of these chapters used eddy covariance, performed using the eddy4R software, which formed the basis of an in-house workflow for calculating the fluxes. A key improvement that has been highlighted as a result of this work is the need to output co-spectral correction information. Co-spectra provide flux as a function of eddy size, and can be used to quantify high frequency losses, such as those that are likely present in the London data due to loss of turbulence in the sample line. For these data the tower height works favourably, at nearly 200 m above the surface, high frequency contribution to the measured flux would be expected to be low. In Delhi however, analysis of this loss will be more important due to the lower sampling height. This should be implemented into the eddy4R workflows for future (and potential re-) analysis.

Additionally, Webb, Pearman and Leuning (WPL) corrections for density fluctuations have not been applied, as in the first instance the AQD NO_x analyser is closed path, so fluctuations in density due to sensible heat are already minimised. Those due to latent heat may also be relevant, but are proportional to the concentration-flux ratio. For NO_x this ratio is small and

Squires et al showed the effect on NO_x fluxes measured in a similar fashion in Beijing were less than 1 % [68]. If the system were to be used to measure fluxes where the concentration-flux ratio were larger, these should be considered, and one solution to this would be drying the sample gas. Traditional methods such as using molecular sieve moisture traps may have to be avoided to achieve this, as they would interrupt turbulence in the sample line. The aforementioned acquisition of co-spectral data from the flux calculations would allow the impact of drying methods to be assessed.

Chapter 5 aimed to complement the ground based emissions measurements of central London with a measurement of the bulk emission from Greater London and surrounding areas, using a mass balance approach. The work consisted of developing a routine for extensible calculation of the interpolated scalar planes so that it could be easily applied to multiple flights. This was through interpolation in the R programming language rather than the more commonly used EasyKrig Matlab software, and cross-validation methods were applied to validate the results. This was reasonably successful, allowing for reproducible calculation of the emissions rates for the three flights. These emission rates were then linked to the surface using a footprint model based on HYSPLIT backwards particle dispersion modelling. This has not yet been developed enough to produce viable comparisons with the inventory, with future work to be focused on improving how particle interaction with the surface is defined. Ultimately with future developments building on the analysis presented here, the method may yet be complimentary to the ground based emissions measurements.

In the longer term, applying the advantages seen in chapter 4, where multiple eddy covariance towers were used to assess one inventory, to the more established NAEI would give more detailed interrogation into its underestimations. This would require the London measurements to become continuous which, as mentioned previously, began in 2020 and will allow more site specific details to be interrogated. Additionally, a second (or more) site(s) measuring NO_x fluxes would allow spatial variation in the NAEI to be explored. Arguably the most important decision here would be site selection - if a second site were available in London, but not central London, it would compliment the airborne eddy covariance measurements made by Vaughan et al. 2016 allowing for comparison with inner/outer London [90]. However, the more interesting measurement may be if a site were possible in another major UK city, such as Birmingham or Manchester, as the NAEI is UK wide. The question could then be asked; is the underestimation of the NO_x emission a London specific phenomena, or does it extend to similar areas? Areas of these cities would be expected to be comparable to central London in many regards, and if this is the case, the underestimation of NO_x emission in the UK may be more widespread.

Appendix A

Contribution to Publications

The work carried out as a part of this PhD has additionally contributed to the following publications:

- F. A. Squires et al. "Measurements of traffic-dominated pollutant emissions in a Chinese megacity". *Atmospheric Chemistry and Physics* 20.14 (2020), 8737–8761
- J. D. Lee, W. S. Drysdale, D. P. Finch, S. E. Wilde, and P. I. Palmer. "UK surface NO_2 levels dropped by 42 % during the COVID-19 lockdown: impact on surface O_3". *Atmospheric Chemistry and Physics* 20 (2020), 15743–15759
- W. J. F. Acton et al. "Surface–atmosphere fluxes of volatile organic compounds in Beijing". *Atmospheric Chemistry and Physics Discussions* 2020 (2020), 1–36
- G. Stewart et al. "Sources of non-methane hydrocarbons in surface air in Delhi, India". *Faraday Discuss.* (2021)
- E. Reyes-Villegas et al. "PM_1 composition and source apportionment at two sites in Delhi, India across multiple seasons". *Atmospheric Chemistry and Physics Discussions* (2020), 1–19
- J. M. Cash et al. "Seasonal analysis of submicron aerosol in Old Delhi using high resolution aerosol mass spectrometry: Chemical characterisation, source apportionment and new marker identification". *Atmospheric Chemistry and Physics Discussions* 2020 (2020), 1–42
- Y. Chen et al. "Avoiding high ozone pollution in Delhi, India". *Faraday Discuss.* (2021)

Appendix B

FAAM Aircraft Configuration for EMeRGe

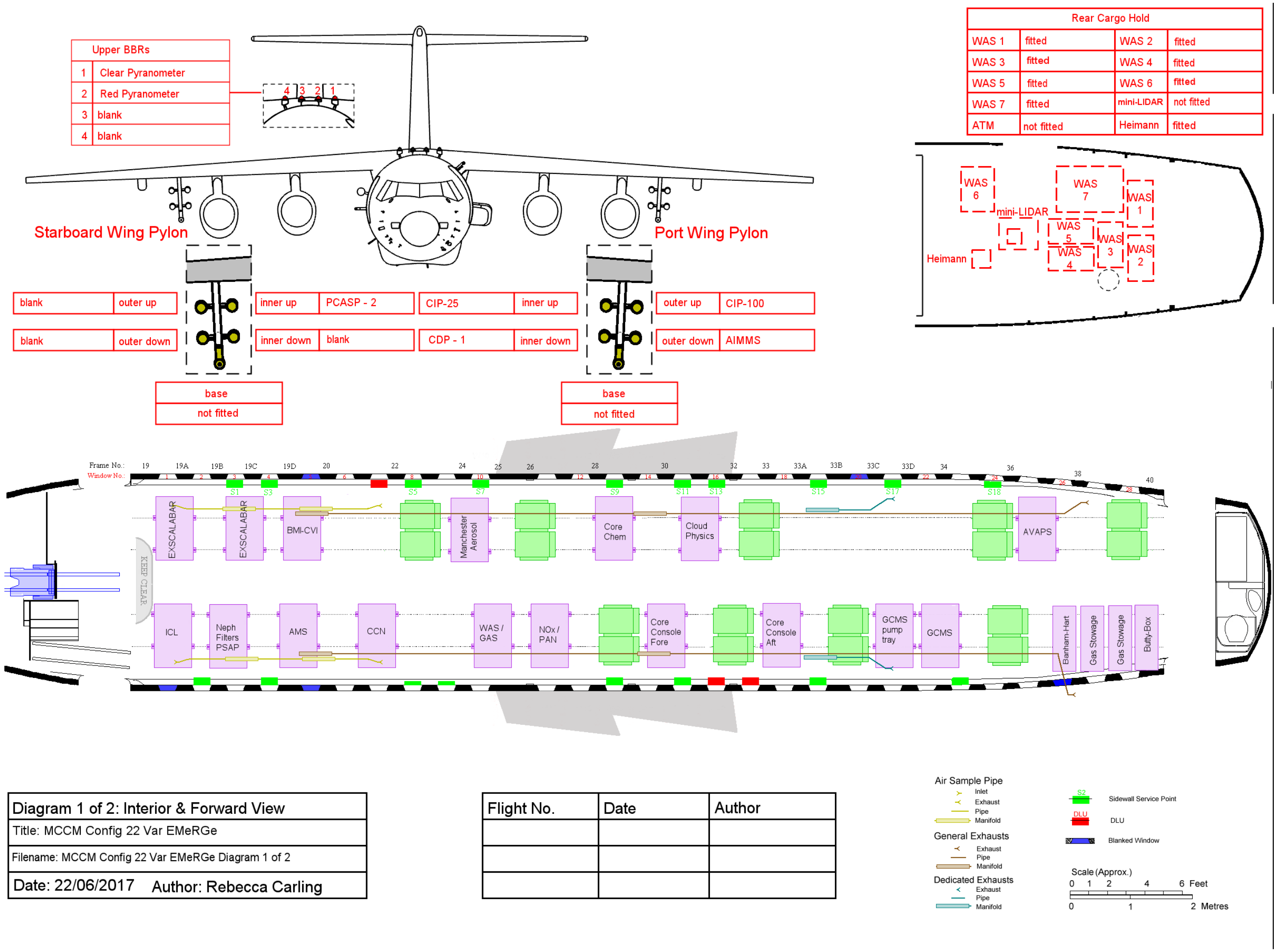

Figure B.1: FAAM instrument configuration for the EMeRGe campaign. 1 of 2

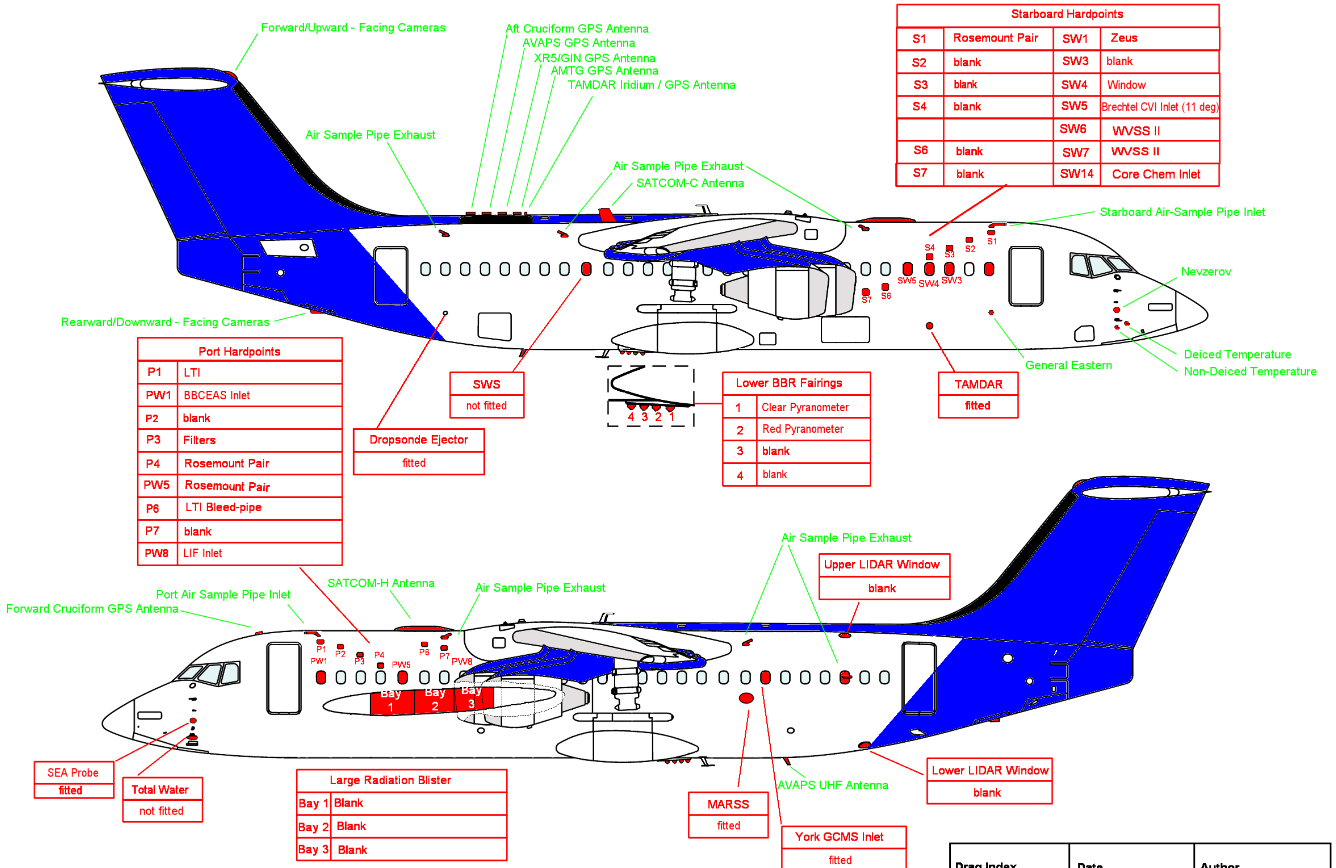

Starboard Hardpoints			
S1	Rosemount Pair	SW1	Zeus
S2	blank	SW3	blank
S3	blank	SW4	Window
S4	blank	SW5	Brechtel CVI Inlet (11 deg)
		SW6	WVSS II
S6	blank	SW7	WVSS II
S7	blank	SW14	Core Chem Inlet

Port Hardpoints	
P1	LTI
PW1	BBCEAS Inlet
P2	blank
P3	Filters
P4	Rosemount Pair
PW5	Rosemount Pair
P6	LTI Bleed-pipe
P7	blank
PW8	LIF Inlet

SWS
not fitted

Dropsonde Ejector
fitted

Lower BBR Fairings	
1	Clear Pyranometer
2	Red Pyranometer
3	blank
4	blank

TAMDAR
fitted

Upper LIDAR Window
blank

SEA Probe
fitted

Total Water
not fitted

Large Radiation Blister	
Bay 1	Blank
Bay 2	Blank
Bay 3	Blank

MARSS
fitted

York GCMS Inlet
fitted

Lower LIDAR Window
blank

Diagram 2 of 2: Aircraft Exterior Views
Title: MCCM Config 22 Var EMeRGe
Filename: MCCM Config 22 Var EMeRGe Diagram 2 of 2
Date: 22/06/2017 Author: Rebecca Carling

Drag Index.	Date	Author
254	22/06/2017	RC

Figure B.2: FAAM instrument configuration for the EMeRGe campaign. 2 of 2

Bibliography

[1] M. Williams. “Air pollution and policy—1952–2002”. *Science of The Total Environment* 334-335 (2004). Highway and Urban Pollution, 15–20.

[2] M. Cames and E. Helmers. “Critical evaluation of the European diesel car boom - global comparison, environmental effects and various national strategies”. *Environmental Sciences Europe* 25.1 (2013).

[3] Council of European Union. *Council regulation (EU) no 715/2007.* eur-lex.europa.eu/legal-content/EN/ALL/?uri=CELEX:32007R0715. 2007.

[4] Council of European Union. *Council regulation (EU) no 459/2012.* eur-lex.europa.eu/legal-content/EN/TXT/?uri=celex:32012R0459. 2012.

[5] Council of European Union. *Council regulation (EU) no 2016/646.* eur-lex.europa.eu/legal-content/EN/TXT/?uri=CELEX:32016R0646. 2016.

[6] A. C. Lewis, D. C. Carslaw, and F. J. Kelly. “Diesel pollution long under-reported”. *Nature* 526.7572 (2015), 195–195.

[7] Q. Schiermeier. *The science behind the Volkswagen emissions scandal.* 2015. URL: nature.com/news/the-science-behind-the-volkswagen-emissions-scandal-1.18426.

[8] D. C. Carslaw et al. “The diminishing importance of nitrogen dioxide emissions from road vehicle exhaust”. *Atmospheric Environment-X* 1 (2019).

[9] World Health Organisation. “Burden of disease from the joint effects of household and ambient Air pollution for 2016 v2” (2018, Accessed September 2020).

[10] J. Lelieveld, J. S. Evans, M. Fnais, D. Giannadaki, and A. Pozzer. “The contribution of outdoor air pollution sources to premature mortality on a global scale”. *Nature* 525.7569 (2015), 367.

[11] D. P. van Vuuren et al. “The representative concentration pathways: an overview”. *Climatic Change* 109 (2011), 5–31.

[12] R. A. Silva et al. “The effect of future ambient air pollution on human premature mortality to 2100 using output from the ACCMIP model ensemble”. *Atmospheric Chemistry and Physics* 16.15 (2016), 9847–9862.

[13] R. Stull. *An Introduction to Boundary Layer Meteorology*. Atmospheric and Oceanographic Sciences Library. Springer Netherlands, 1988.

[14] G. I. Taylor. “The spectrum of turbulence”. *Proceedings of the Royal Society of London Series a-Mathematical and Physical Sciences* 164.A919 (1938), 0476–0490.

[15] T. Foken. “50 years of the Monin-Obukhov similarity theory”. *Boundary-Layer Meteorology* 119.3 (2006), 431–447.

[16] T. R. Oke. “THE ENERGETIC BASIS OF THE URBAN HEAT-ISLAND”. *Quarterly Journal of the Royal Meteorological Society* 108.455 (1982), 1–24.

[17] G. Stewart et al. “Sources of non-methane hydrocarbons in surface air in Delhi, India”. *Faraday Discuss.* (2021).

[18] P. D. Jones, C. Harpham, and K. R. Briffa. “Lamb weather types derived from reanalysis products”. *International Journal of Climatology* 33.5 (2013), 1129–1139.

[19] G. P. O’Hare and R. Wilby. “A REVIEW OF OZONE POLLUTION IN THE UNITED-KINGDOM AND IRELAND WITH AN ANALYSIS USING LAMB WEATHER TYPES”. *Geographical Journal* 161 (1995), 1–20.

[20] R. M. Harrison, D. Laxen, S. Moorcroft, and K. Laxen. “Processes affecting concentrations of fine particulate matter (PM2.5) in the UK atmosphere”. *Atmospheric Environment* 46 (2012), 115–124.

[21] R. J. Pope, N. H. Savage, M. P. Chipperfield, S. R. Arnold, and T. J. Osborn. “The influence of synoptic weather regimes on UK air quality: analysis of satellite column NO2”. *Atmospheric Science Letters* 15.3 (2014), 211–217.

[22] A. M. Graham et al. “Impact of weather types on UK ambient particulate matter concentrations”. *Atmospheric Environment-X* 5 (2020).

[23] R. V. Martin et al. “Global inventory of nitrogen oxide emissions constrained by space-based observations of NO2 columns”. *Journal of Geophysical Research-Atmospheres* 108.D17 (2003).

[24] M. Crippa et al. “Gridded emissions of air pollutants for the period 1970-2012 within EDGAR v4.3.2”. *Earth System Science Data* 10.4 (2018), 1987–2013.

[25] L. T. Murray, D. J. Jacob, J. A. Logan, R. C. Hudman, and W. J. Koshak. "Optimized regional and interannual variability of lightning in a global chemical transport model constrained by LIS/OTD satellite data". *Journal of Geophysical Research-Atmospheres* 117 (2012).

[26] K. Denman et al. "Couplings Between Changes in the Climate System and Biogeochemistry". In: *Climate Change 2007: The Physical Science Basis*. 2007. Chap. 7, 499–587.

[27] United Nations, Department of Economic and Social Affairs, Population Division. *World Urbanization Prospects: The 2018 Revision, Online Edition*. 2018, Accessed September 2020. URL: population.un.org/wup/Download/.

[28] United Nations, Department of Economic and Social Affairs, Population Division. *The World's Cities in 2018 — Data Booklet*. 2018, Accessed September 2020. URL: un.org/en/events/citiesday/assets/pdf/the_worlds_cities_in_2018_data_booklet.pdf.

[29] Defra and BEIS, licenced under the Open Government Licence (OGL), Crown Copyright 2020. *National Atmospheric Emissions Inventory*. 2017, accessed September 2020. URL: naei.beis.gov.uk/data/.

[30] M. A. H. Khan et al. "The global budgets of organic hydroperoxides for present and pre-industrial scenarios". *Atmospheric Environment* 110 (2015), 65–74.

[31] R. E. Dunmore et al. "Diesel-related hydrocarbons can dominate gas phase reactive carbon in megacities". *Atmospheric Chemistry and Physics* 15.17 (2015), 9983–9996.

[32] P. S. Monks. "Tropospheric Photochemistry". In: *Handbook of Atmospheric Science*. John Wiley & Sons, Ltd, 2007. Chap. 6, 156–187.

[33] M. Prather, D. Ehhalt, F. Dentener, R. Derwent, and A. Grubler. "Atmospheric chemistry and greenhouse gases". In: *Climate Change 2001: The Scientific Basis, Third Assessment Report*. IPCC: Working Group I of the Intergovernmental Panel on Climate Change, 2001.

[34] Y. F. Ma, K. D. Lu, C. C. K. Chou, X. Q. Li, and Y. H. Zhang. "Strong deviations from the NO-NO2-O-3 photostationary state in the Pearl River Delta: Indications of active peroxy radical and chlorine radical chemistry". *Atmospheric Environment* 163 (2017), 22–34.

[35] P. A. Leighton. *Photochemistry of Air Pollution*. Elsevier, 1961.

[36] J. Matsumoto et al. “Examination on photostationary state of NOx in the urban atmosphere in Japan”. *Atmospheric Environment* 40.18 (2006), 3230–3239.

[37] R. Atkinson. “Atmospheric chemistry of VOCs and NOx”. *Atmospheric Environment* 34 (1998), 2063–2101.

[38] B. J. Finlayson-Pitts and J. N. Pitts. “ATMOSPHERIC CHEMISTRY OF TROPOSPHERIC OZONE FORMATION - SCIENTIFIC AND REGULATORY IMPLICATIONS”. *Journal of the Air & Waste Management Association* 43.8 (1993), 1091–1100.

[39] A. V. Jackson. “Sources of Air Pollution”. In: *Handbook of Atmospheric Science.* John Wiley & Sons, Ltd, 2007. Chap. 5, 124–155.

[40] J. D. Lee et al. “Detailed budget analysis of HONO in central London reveals a missing daytime source”. *Atmospheric Chemistry and Physics* 16.5 (2016), 2747–2764.

[41] P. S. Monks. “A review of the observations and origins of the spring ozone maximum”. *Atmospheric Environment* 34.21 (2000), 3545–3561.

[42] D. A. Savitz et al. “Ambient Fine Particulate Matter, Nitrogen Dioxide, and Term Birth Weight in New York, New York”. *American Journal of Epidemiology* 179.4 (2014), 457–466.

[43] A. S. V. Shah et al. “Short term exposure to air pollution and stroke: systematic review and meta-analysis”. *Bmj-British Medical Journal* 350 (2015).

[44] F. Forastiere, A. Peters, F. J. Kelly, and S. T. Holgate. “Nitrogen dioxide”. In: *Air quality guidelines global update 2005 : particulate matter, ozone, nitrogen dioxide and sulfur dioxide.* 2005. Chap. 12, 331–394.

[45] P. H. N. Saldiva, N. Kunzli, and N. Lippmann. “Ozone”. In: *Air quality guidelines global update 2005 : particulate matter, ozone, nitrogen dioxide and sulfur dioxide.* 2005. Chap. 11, 307–330.

[46] A. Ponce de Leon, H. R. Anderson, J. M. Bland, D. P. Strachan, and J. Bower. “Effects of air pollution on daily hospital admissions for respiratory disease in London between 1987-88 and 1991-92”. *Journal of Epidemiology and Community Health* 50 (1996), S63–S70.

[47] P. C. Chen et al. “Short-term effect of ozone on the pulmonary function of children in primary school”. *Environmental Health Perspectives* 107.11 (1999), 921–925.

[48] D. Q. Rich et al. "Increased risk of paroxysmal atrial fibrillation episodes associated with acute increases in ambient air pollution". *Environmental Health Perspectives* 114.1 (2006), 120–123.

[49] M. W. Frampton et al. "Multicenter Ozone Study in oldEr Subjects (MOSES): Part 1. Effects of Exposure to Low Concentrations of Ozone on Respiratory and Cardiovascular Outcomes". *Res Rep Health Eff Inst* 192, Pt 1 (2017), 1–107.

[50] R. McConnell et al. "Asthma in exercising children exposed to ozone: a cohort study". *Lancet* 359.9304 (2002), 386–391.

[51] S. V. Krupa, M. Nosal, and A. H. Legge. "A numerical analysis of the combined open-top chamber data from the USA and Europe on ambient ozone and negative crop responses". *Environmental Pollution* 101.1 (1998), 157–160.

[52] R. Van Dingenen et al. "The global impact of ozone on agricultural crop yields under current and future air quality legislation". *Atmospheric Environment* 43.3 (2009), 604–618.

[53] HEI Review Panel on Ultrafine Particles. "Understanding the Health Effects of Ambient Ultrafine Particles. HEI Perspectives 3" (2013, Accessed September 2020).

[54] S. Ohlwein, R. Kappeler, M. K. Joss, N. Kunzli, and B. Hoffmann. "Health effects of ultrafine particles: a systematic literature review update of epidemiological evidence". *International Journal of Public Health* 64.4 (2019), 547–559.

[55] M. R. Heal, P. Kumar, and R. M. Harrison. "Particles, air quality, policy and health". *Chemical Society Reviews* 41.19 (2012), 6606–6630.

[56] J. M. Samet, M. Brauer, and R. Schlesinger. "Particulate matter". In: *Air quality guidelines global update 2005 : particulate matter, ozone, nitrogen dioxide and sulfur dioxide*. 2005. Chap. 10, 217–306.

[57] Council of European Union. *Council regulation (EU) no 50/2008*. eur-lex.europa.eu/legal-content/EN/TXT/?uri=CELEX:02008L0050-20150918. 2008.

[58] Department for Environment, Food and Rural Affairs. *2010 to 2015 government policy: environmental quality - Appendix 5*. 2015, Accessed September 2020. URL: www.defra.gov.uk/environment/quality/air/air-quality/approach/.

[59] Department for Environment, Food and Rural Affairs. *Automatic Urban and Rural Network*. Accessed September 2020. URL: uk-air.defra.gov.uk/networks/network-info?view=aurn.

[60] European Environment Agency. *Air Pollution.* Accessed September 2020. URL: www.eea.europa.eu/themes/air.

[61] Central Pollution Control Board. *Central Control Room for Air Quality Management.* Accessed September 2020. URL: cpcbccr.com.

[62] Environmental Protection Agency. *Air Data: Air Quality Data Collected at Outdoor Monitors Across the US.* Accessed September 2020. URL: epa.gov/outdoor-air-quality-data.

[63] Imperial College London. *London Air.* Accessed September 2020. URL: londonair.org.uk.

[64] J. D. Lee, W. S. Drysdale, D. P. Finch, S. E. Wilde, and P. I. Palmer. "UK surface NO_2 levels dropped by 42 % during the COVID-19 lockdown: impact on surface O_3". *Atmospheric Chemistry and Physics* 20 (2020), 15743–15759.

[65] T. Karl et al. "Urban eddy covariance measurements reveal significant missing NOx emissions in Central Europe". *Scientific Reports* 7 (2017), 2536.

[66] T. Karl, M. Striednig, M. Graus, A. Hammerle, and G. Wohlfahrt. "Urban flux measurements reveal a large pool of oxygenated volatile organic compound emissions". *Proceedings of the National Academy of Sciences of the United States of America* 115.6 (2018), 1186–1191.

[67] W. J. F. Acton et al. "Surface–atmosphere fluxes of volatile organic compounds in Beijing". *Atmospheric Chemistry and Physics Discussions* 2020 (2020), 1–36.

[68] F. A. Squires et al. "Measurements of traffic-dominated pollutant emissions in a Chinese megacity". *Atmospheric Chemistry and Physics* 20.14 (2020), 8737–8761.

[69] C. Helfter et al. "Spatial and temporal variability of urban fluxes of methane, carbon monoxide and carbon dioxide above London, UK". *Atmospheric Chemistry and Physics* 16.16 (2016), 10543–10557.

[70] P. L. Kebabian, S. C. Herndon, and A. Freedman. "Detection of Nitrogen Dioxide by Cavity Attenuated Phase Shift Spectroscopy". *Analytical Chemistry* 77.2 (2005), 724–728.

[71] U. Javed et al. "Laser-induced fluorescence-based detection of atmospheric nitrogen dioxide and comparison of different techniques during the PARADE 2011 field campaign". *Atmospheric Measurement Techniques* 12.3 (2019), 1461–1481.

[72] D. Grosjean and J. Harrison. "RESPONSE OF CHEMI-LUMINESCENCE NOX ANALYZERS AND ULTRAVIOLET OZONE ANALYZERS TO ORGANIC AIR-POLLUTANTS". *Environmental Science & Technology* 19.9 (1985), 862–865.

[73] C. Reed, M. J. Evans, P. Di Carlo, J. D. Lee, and L. J. Carpenter. "Interferences in photolytic NO2 measurements: explanation for an apparent missing oxidant?" *Atmospheric Chemistry and Physics* 16.7 (2016), 4707–4724.

[74] J. Drummond, V. A., and E. D. H. "An optimized chemiluminescence detector for tropospheric NO measurements". *Journal of Atmospheric Chemistry* 2 (1985), 287–306.

[75] J. D. Lee et al. "Year-round measurements of nitrogen oxides and ozone in the tropical North Atlantic marine boundary layer". *Journal of Geophysical Research-Atmospheres* 114 (2009).

[76] G. Burba. *Eddy Covariance Method for Scientific, Industrial, Agricultural, and Regulatory Applications: A Field Book on Measuring Ecosystem Gas Exchange and Areal Emission Rates*. LI-COR Biosciences, Lincoln, NE, USA, 2013.

[77] M. Aubinet, T. Vesala, and D. Papale, eds. *Eddy Covariance: A Practical Guide to Measurement and Data Analysis*. Vol. 12. 2012.

[78] X. Lee, W. Massman, and B. Law, eds. *Handbook of Micrometeorology*. Springer Netherlands, 2004.

[79] D. Vickers and L. Mahrt. "Quality control and flux sampling problems for tower and aircraft data". *Journal of Atmospheric and Oceanic Technology* 14.3 (1997), 512–526.

[80] D. Vickers and L. Mahrt. "The cospectral gap and turbulent flux calculations". *Journal of Atmospheric and Oceanic Technology* 20.5 (2003), 660–672.

[81] F. V. Brock. "A Nonlinear Filter to Remove Impulse Noise from Meteorological Data". *Journal of Atmospheric and Oceanic Technology* 3.1 (1986), 51–58.

[82] D. Starkenburg et al. "Assessment of Despiking Methods for Turbulence Data in Micrometeorology". *Journal of Atmospheric and Oceanic Technology* 33.9 (2016), 2001–2013.

[83] A. A. Turnipseed, D. E. Anderson, P. D. Blanken, W. M. Baugh, and R. K. Monson. "Airflows and turbulent flux measurements in mountainous terrain Part 1. Canopy and local effects". *Agricultural and Forest Meteorology* 119.1-2 (2003), 1–21.

[84] J. M. Wilczak, S. P. Oncley, and S. A. Stage. “Sonic anemometer tilt correction algorithms”. *Boundary-Layer Meteorology* 99.1 (2001), 127–150.

[85] S. Metzger et al. *Algorithm Theoretical Basis Document (ATBD): Eddy-Covariance Data Products Bundle.* data.neonscience.org/documents/10179/2403599/NEON.DOC.004571vA/18a9fbe9-a84b-4441-8283-dc498829b073. 2018, Accessed September 2020.

[86] T. Foken and B. Wichura. “Tools for quality assessment of surface-based flux measurements”. *Agricultural and Forest Meteorology* 78.1-2 (1996), 83–105.

[87] D. Vickers, C. Thomas, and B. E. Law. “Random and systematic CO2 flux sampling errors for tower measurements over forests in the convective boundary layer”. *Agricultural and Forest Meteorology* 149.1 (2009), 73–83.

[88] S. T. Salesky, M. Chamecki, and N. L. Dias. “Estimating the Random Error in Eddy-Covariance Based Fluxes and Other Turbulence Statistics: The Filtering Method”. *Boundary-Layer Meteorology* 144.1 (2012), 113–135.

[89] J. Mann and D. H. Lenschow. “ERRORS IN AIRBORNE FLUX MEASUREMENTS”. *Journal of Geophysical Research-Atmospheres* 99.D7 (1994), 14519–14526.

[90] A. R. Vaughan et al. “Spatially resolved flux measurements of NOx from London suggest significantly higher emissions than predicted by inventories”. *Faraday Discussions* 189 (2016), 455–472.

[91] J. D. Lee et al. “Measurement of NOx Fluxes from a Tall Tower in Central London, UK and Comparison with Emissions Inventories”. *Environmental Science & Technology* 49.2 (2015), 1025–1034.

[92] A. R. Vaughan et al. “VOC emission rates over London and South East England obtained by airborne eddy covariance”. *Faraday Discussions* 200 (2017), 599–620.

[93] T. Vesala et al. “Flux and concentration footprint modelling: State of the art”. *Environmental Pollution* 152.3 (2008), 653–666.

[94] H. P. Schmid. “Footprint modeling for vegetation atmosphere exchange studies: a review and perspective”. *Agricultural and Forest Meteorology* 113.1-4 (2002), 159–183.

[95] N. Kljun, P. Calanca, M. W. Rotach, and H. P. Schmid. “A simple parameterisation for flux footprint predictions”. *Boundary-Layer Meteorology* 112.3 (2004), 503–523.

[96] N. Kljun, P. Calanca, M. W. Rotach, and H. P. Schmid. "A simple two-dimensional parameterisation for Flux Footprint Prediction (FFP)". *Geoscientific Model Development* 8.11 (2015), 3695–3713.

[97] S. Metzger et al. "Eddy-covariance flux measurements with a weight-shift microlight aircraft". *Atmospheric Measurement Techniques* 5.7 (2012), 1699–1717.

[98] S. Metzger et al. "eddy4R 0.2.0: a DevOps model for community-extensible processing and analysis of eddy-covariance data based on R, Git, Docker, and HDF5". *Geoscientific Model Development* 10.9 (2017), 3189–3206.

[99] Acton, W. J. "Measurements of VOC fluxes in New Delhi - working title" (in prep).

[100] Acton, W. J. "PTR-MS eddy covariance flux calculation intercomparison - working title" (in prep).

[101] LI-COR Lincoln, NE. *EddyPro Software (Version 7.0)*. Infrastructure for Measurements of the European Carbon Cycle consortium. 2019.

[102] D. Smith and S. Metzger. *Algorithm Theoretical Basis Document: Quality Flags and Quality Metrics for TIS Data Products.* data.neonscience.org/api/v0/documents/NEON.DOC.001113vA. 2013, Accessed September 2020.

[103] J. E. Tillman. "The Indirect Determination of Stability, Heat and Momentum Fluxes in the Atmospheric Boundary Layer from Simple Scalar Variables During Dry Unstable Conditions". *Journal of Applied Meteorology* 11 (1972), 783–792.

[104] T. Foken et al. "Post-field data quality control". In: *Handbook of Micrometeorology*. Ed. by X. Lee, W. Massman, and B. Law. Springer Netherlands, 2004.

[105] C. Thomas, T. Foken, and Ams. "Re-evaluation of integral turbulence characteristics and their parameterisations". *15th Symposium on Boundary Layers and Turbulence* (2002), 129–132.

[106] S. K. Grange and D. C. Carslaw. "Using meteorological normalisation to detect interventions in air quality time series". *Science of the Total Environment* 653 (2019), 578–588.

[107] Transport for London. *Congestion Charging - Impacts Monitoring Fourth Annual Report*. 2016.

[108] A. R. Vaughan. "Measurement and Understanding of Emissions over London and Southern England by Airborne Eddy-Covariance". 2017.

[109] Environment Agency. *LIDAR Composite DSM*. 2015. URL: data.gov.uk.

[110] J. W. Deardorff and G. E. Willis. "FURTHER RESULTS FROM A LABORATORY MODEL OF THE CONVECTIVE PLANETARY BOUNDARY-LAYER". *Boundary-Layer Meteorology* 32.3 (1985), 205–236.

[111] R. Atkinson et al. "IUPAC Task Group on Atmospheric Chemical Kinetic Data Evaluation". *Atmospheric Chemistry and Physics* 4 (2004), 1461–1738.

[112] D. Stone, L. K. Whalley, and D. E. Heard. "Tropospheric OH and HO2 radicals: field measurements and model comparisons". *Chem. Soc. Rev.* 41 (19 2012), 6348–6404.

[113] Copernicus Climate Change Service Climate Data Store (CDS). *Copernicus Climate Change Service (C3S): ERA5: Fifth generation of ECMWF atmospheric reanalyses of the global climate*. 2017, accessed Feb 2020. URL: cds.climate.copernicus.eu/cdsapp#!/home.

[114] D. H. Lenschow, J. Mann, and L. Kristensen. "HOW LONG IS LONG ENOUGH WHEN MEASURING FLUXES AND OTHER TURBULENCE STATISTICS". *Journal of Atmospheric and Oceanic Technology* 11.3 (1994), 661–673.

[115] R. Leuning and K. M. King. "COMPARISON OF EDDY-COVARIANCE MEASUREMENTS OF CO2 FLUXES BY OPEN-PATH AND CLOSED-PATH CO2 ANALYZERS". *Boundary-Layer Meteorology* 59.3 (1992), 297–311.

[116] W. Sutherland. "The viscosity of gases and molecular force". *Philosophical Magazine* 5 (1893), 507–531.

[117] D. R. Drew, J. F. Barlow, and S. E. Lane. "Observations of wind speed profiles over Greater London, UK, using a Doppler lidar". *Journal of Wind Engineering and Industrial Aerodynamics* 121 (2013), 98–105.

[118] Transport for London. *Bus Fleet Audit*. 2017, accessed Feb 2020. URL: content.tfl.gov.uk/fleet-audit-30-june-2017-final.pdf.

[119] Council of European Union. *Council regulation (EU) no 2016/2284*. eur-lex.europa.eu/legal-content/EN/TXT/?uri=uriserv:OJ.L_.2016.344.01.0001.01.ENG. 2016.

[120] European Environment Agency. *EMEP/EEA air pollutant emission inventory guidebook 2016*. Publications Office of the European Union, 2016.

[121] I. Tsagatakis et al. *UK Emission Mapping Methodology – 2016 Emissions*. 2018.

[122] D. M. Brookes et al. *Technical report on UK supplementary assessment under the Air Quality Directive (2008/50/EC), the Air Quality Framework Directive (96/62/EC) and Fourth Daughter Directive (2004/107/EC) for 2012*. 2013.

[123] P. Coleman et al. *Assessment of benzo[a]pyrene atmospheric concentrations in the UK to support the establishment of a national PAH objective*. 2001.

[124] H. D. van der Gon, C. Hendriks, J. Kuenen, A. Segers, and A. Visschedijk. *Description of current temporal emission patterns and sensitivity of predicted AQ for temporal emission patterns*. 2011.

[125] *original source data provided by Operational Analysis department, Transport for London.*

[126] W. H. Organisation. *WHO Global Ambient Air Quality Database (Update 2018)*. 2018, Accessed Sept 2020. URL: who.int/airpollution/data/cities.

[127] European Commission, Joint Research Centre (EC-JRC)/Netherlands Environmental Assessment Agency (PBL). "Emissions Database for Global Atmospheric Research (EDGAR), release EDGAR v4.3.2 (1970 - 2012)" (2017, Accessed April 2019).

[128] J. A. Geddes, R. V. Martin, B. L. Boys, and A. van Donkelaar. "Long-Term Trends Worldwide in Ambient NO2 Concentrations Inferred from Satellite Observations". *Environmental Health Perspectives* 124.3 (2016), 281–289.

[129] J. Li. "Pollution Trends in China from 2000 to 2017: A Multi-Sensor View from Space". *Remote Sensing* 12.2 (2020).

[130] J. Kurokawa and T. Ohara. "Long-term historical trends in air pollutant emissions in Asia: Regional Emission inventory in ASia (REAS) version 3.1". *Atmospheric Chemistry and Physics Discussions* 2019 (2019), 1–51.

[131] S. K. Singh. "Urban Transport in India: Issues, Challenges, and the Way Forward". *European Transport* (52 2012).

[132] C. W. Spicer, D. W. Joseph, and W. M. Ollison. "A Re-Examination of Ambient Air Ozone Monitor Interferences". *JOURNAL OF THE AIR & WASTE MANAGEMENT ASSOCIATION* 60.11 (2010), 1353–1364.

[133] V. Shrangi. "Badarpur power plant shut, action plan to tackle air pollution in Delhi-NCR comes into force". *Hindustan Times* (2018). accessed September 2020.

[134] D. Fowler and J. Duyzer. "Micrometeorological techniques for the measurement of trace gas exchange". In: *In Exchange of Trace Gases between Terrestrial Ecosystems and the Atmosphere*. Ed. by M. O. Andreae and D. S. Schimel. John Wiley & Sons Ltd., 1989, 189–207.

[135] E. Nemitz, K. J. Hargreaves, A. G. McDonald, J. R. Dorsey, and D. Fowler. "Meteorological measurements of the urban heat budget and CO2 emissions on a city scale". *Environmental Science & Technology* 36.14 (2002), 3139–3146.

[136] J. Stocker. "PROMOTE: Process analysis, observations and modelling – Integrated solutions for cleaner air for Delhi. Delhi road emissions analyses". *personal comms.* (2020). Cambridge Environmental Research Consultants.

[137] J. Stocker. "PROMOTE: Process analysis, observations and modelling – Integrated solutions for cleaner air for Delhi. Investigating emission rates on the explicit road network". *personal comms.* (2020). Cambridge Environmental Research Consultants.

[138] N. R. P. Harris et al. "COORDINATED AIRBORNE STUDIES IN THE TROPICS (CAST)". *Bulletin of the American Meteorological Society* 98.1 (2017), 145.

[139] K. L. Mays et al. "Aircraft-Based Measurements of the Carbon Footprint of Indianapolis". *Environmental Science & Technology* 43.20 (2009), 7816–7823.

[140] S. J. O'Shea et al. "Area fluxes of carbon dioxide, methane, and carbon monoxide derived from airborne measurements around Greater London: A case study during summer 2012". *Journal of Geophysical Research-Atmospheres* 119.8 (2014), 4940–4952.

[141] J. R. Pitt et al. "Assessing London CO2, CH4 and CO emissions using aircraft measurements and dispersion modelling". *Atmospheric Chemistry and Physics* 19.13 (2019), 8931–8945.

[142] K. Ashworth et al. "Megacity and local contributions to regional air pollution: an aircraft case study over London". *Atmospheric Chemistry and Physics* 20.12 (2020), 7193–7216.

[143] T. Klausner et al. “Urban greenhouse gas emissions from the Berlin area: A case study using airborne CO2 and CH4 in situ observations in summer 2018”. *Elementa-Science of the Anthropocene* 8 (2020).

[144] V. Brocchi et al. “Local air pollution from oil rig emissions observed during the airborne DACCIWA campaign”. *Atmospheric Chemistry and Physics* 19.17 (2019), 11401–11411.

[145] P. K. Kitanidis. *Introduction to Geostatistics: Applications in Hydrogeology.* Cambridge University Press, 1997.

[146] D. Chu. *The GLOBEC Kriging software package—EasyKrig3.0; The Woods Hole Oceanographic Institution.* 2014.

[147] E. J. Pebesma. “Multivariable geostatistics in S: the gstat package”. *Computers & Geosciences* 30 (2004), 683–691.

[148] B. Gräler, E. Pebesma, and G. Heuvelink. “Spatio-Temporal Interpolation using gstat”. *The R Journal* 8 (1 2016), 204–218.

[149] J. C. Turnbull et al. “Synthesis of Urban CO2 Emission Estimates from Multiple Methods from the Indianapolis Flux Project (INFLUX)”. *Environmental Science & Technology* 53.1 (2019), 287–295.

[150] A. F. Stein et al. “NOAA’S HYSPLIT ATMOSPHERIC TRANSPORT AND DISPERSION MODELING SYSTEM”. *Bulletin of the American Meteorological Society* 96.12 (2015), 2059–2077.

[151] U. Baltensperger, S. Nyeki, and M. Kalberer. “Atmospheric Particulate Matter”. In: *Handbook of Atmospheric Science.* John Wiley & Sons, Ltd, 2007. Chap. 5, 124–155.

[152] B. Graler, E. Pebesma, and G. Heuvelink. *Spatio-Temporal Interpolation using gstat.* 2016. URL: cran.r-project.org/web/packages/gstat/vignettes/spatio-temporal-kriging.pdf.

[153] E. R. Morris. “Simulations of air quality in West Africa: An evaluation of the emissions, sources, seasonality and impacts of pollutants”. 2019.

[154] E. Reyes-Villegas et al. “PM_1 composition and source apportionment at two sites in Delhi, India across multiple seasons”. *Atmospheric Chemistry and Physics Discussions* (2020), 1–19.

[155] J. M. Cash et al. “Seasonal analysis of submicron aerosol in Old Delhi using high resolution aerosol mass spectrometry: Chemical characterisation, source apportionment and new marker identification”. *Atmospheric Chemistry and Physics Discussions* 2020 (2020), 1–42.

[156] Y. Chen et al. “Avoiding high ozone pollution in Delhi, India”. *Faraday Discuss.* (2021).